Spectroscopy of spin-valley excitons in two-dimensional semiconductors and heterostructures

Victor Funk

München 2024

Spectroscopy of spin-valley excitons in two-dimensional semiconductors and heterostructures

Victor Funk

Dissertation
an der Fakultät für Physik
der Ludwig-Maximilians-Universität
München

vorgelegt von
Victor Funk
aus Schwäbisch Gmünd, Deutschland

München, den 8. Oktober 2024

Erstgutachter: Prof. Dr. Alexander Högele
Zweitgutachter: Prof Dr. Alexey Chernikov

Tag der mündlichen Prüfung: 13.November 2024

Zusammenfassung

Übergangsmetall-Dichalkogenide wie Wolframdiselenid (WSe_2) und Molybdändiselenid ($MoSe_2$) sind zweidimensionale Halbleiter, die einzigartige optische und elektronische Eigenschaften aufweisen. Im Grenzfall der Monolage weisen sie eine direkte Bandlücke auf, mit optischen Übergängen im sichtbaren bis nahinfraroten Bereich. An den Energieminima der inäquivalenten K- und K' Valleys koppelt Licht-Materie-Wechselwirkung Elektronen des Leitungsbandes mit Löchern im Valenzband. Die reduzierte elektrostatische Abschirmung aufgrund der zweidimensionalen Kristallstruktur führt zur Bildung von fest gebundenen Exzitonen. Diese sind energetisch entartet und zeigen vom Valley-Index abhängige optische Auswahlregeln, ideal für optoelektronische Bauelemente der nächsten Generation. Diese Arbeit konzentriert sich auf die Licht-Materie-Wechselwirkungen in WSe_2-Mono- und Bilagen sowie $MoSe_2$-WSe_2-Heterobilagen bei kryogenen Temperaturen, um das Verständnis ihrer Exzitonenübergänge, Phononenwechselwirkungen und Polarisationseigenschaften zu vertiefen.

Der erste Teil dieser Studie untersucht die temperaturabhängige Photolumineszenz von WSe_2 Mono- und Bilagen unter kontrollierter elektrostatischer Dotierung. Es wurde eine ausgeprägte Asymmetrie in der phononenunterstützten Lumineszenz von impulsindirekten Exzitonenreservoiren beobachtet. Im Kontrast dazu, zeigen Exzitonen mit direktem optischen Übergang thermisch verbreiterte, symmetrische Spektralprofile. Die Photonen-Dispersionsrelation reduziert durch Energie- und Impulserhaltung die Anzahl an erlaubten radiativen Zuständen. Diese Einschränkung wird durch Phononen aufgehoben. Die Ergebnisse dieser Arbeit tragen zum Verständnis der phononenunterstützten Rekombination von Impuls-dunklen Exzitonen bei und ermöglichen den Zugang zur thermischen Verteilung von Exzitonen mit endlichen Impulsen in atomar dünnen Halbleitern mit indirekten Bandlücken.

Der zweite Teil der Arbeit untersucht die Spindynamik von Interlagen-Exzitonen in antiparallelen $MoSe_2$-WSe_2 Heterobilagen in Spin-Triplett Konfiguration. Kryogene, spektrale und zeitaufgelöste Messungen der Photolumineszenz im Magnetfeld wurden unter kontrollierter Polarisation durchgeführt. Der gemessene Polarisationsgrad wurde in magnetische und optische Beiträge zerlegt und innerhalb eines Ratengleichungsmodell beschrieben. Das Modell bezieht die Thermalisierung zwischen Zeeman-gespaltenen Reservoiren sowie die Dephasierung durch langreichweitige Coulomb-Wechselwirkungen mit ein. Im Rahmen dieser minimalen Annahmen wurden Impuls-indirekte Interlagen-Exzitonen als polarisationserhaltendes Reservoir vorgeschlagen. Diese Arbeit untersucht die Valley-polarisation von Interlagen-Exzitonen als Funktion des Magnetfelds im Gleichgewichtszustand, sowie zeitaufgelöst und bietet ein analytisches Gerüst, welches sich auf die ganze Klasse von Heterobilagen und deren Interlagen-Exzitonen übertragen lässt.

Abstract

Transition metal dichalcogenides such as tungsten diselenide (WSe_2) and molybdenum diselenide ($MoSe_2$) are two-dimensional semiconductors that exhibit unique optical and electronic properties. In the monolayer limit, they exhibit a direct band gap with optical transitions in the visible to near-infrared spectrum. At the energy minima of the inequivalent K and K' valleys, light-matter interactions couple electrons of the conduction band with empty valence band states. The reduced electrostatic screening due to the two-dimensional nature of the crystal structure leads to the formation of tightly bound excitons. These are energetically degenerate and exhibit valley-index dependent optical selection rules, making them ideal for next generation optoelectronic devices. This thesis focuses on the light-matter interactions in WSe_2 mono- and bilayers as well as $MoSe_2$-WSe_2 heterobilayers at cryogenic temperatures to add to the understanding of their exciton transitions, phonon interactions and valley polarisation.

The first part of this study investigates the temperature-dependent photoluminescence of WSe_2 mono- and bilayer under controlled electrical doping. A pronounced asymmetry in the spectral profile of phonon-assisted luminescence from momentum-indirect exciton reservoirs were observed. In contrast, excitons with direct radiative decay pathways display thermally broadened, symmetric spectral profiles. The photon dispersion relation reduces the number of allowed radiative states due to energy and momentum conservation. This restriction is removed by phonons. The results of this work add to the understanding of phonon-assisted recombination of momentum-dark excitons and, more generally, establish means to access the thermal distribution of finite-momentum excitons in atomically thin semiconductors with indirect bandgaps.

The second part of the thesis explores the spin dynamics of interlayer excitons in $MoSe_2$-WSe_2 heterobilayers in spin-triplet configuration. Cryogenic, spectral and time-resolved measurements of the photoluminescence in magnetic field were performed under controlled polarisation. The measured degree of polarisation was decomposed into magnetic and optical contributions and described within a rate equation model. The model includes thermalisation between Zeeman-split reservoirs and dephasing due to long-range Coulomb interactions. Within these minimal assumptions, momentum-indirect interlayer excitons were found as a polarisation-maintaining reservoir. The resulting valley polarisation of interlayer excitons as a function of magnetic field was described for both the steady-state and time-resolved regimes. This work provides an analytical framework applicable to the whole class of interlayer-excitons in heterobilayer systems.

Contents

1 Introduction

"One shouldn't work on semiconductors, that is a filthy mess; who knows whether any semiconductors exist"

— Wolfgang Pauli, *Letters to Peierls, 1931*

Michael Faraday not only discovered fundamental interactions of electricity and magnetism, but also documented the first observation of a semiconductor effect in 1833, where he noticed that the resistance in silver sulfide decreases with temperature. It took another century, until Rudolf Peierls in 1930 presented for the first time a concept of forbidden gaps that was applied to realistic solids by Brillouin [1]. Fortunately, Pauli's scepticism towards this theory was unjustified as nearly another century later, semiconducting silicon defines most electronic circuits we use in our daily life. Ongoing miniaturisation of these circuits composed of transistors is commonly described by Moore's law [2] and Dennard scaling [3]. Their prediction on exponentially growing performance over time requires not only higher resolution of fabrication techniques, but as we reach the fundamental limits of the transistor size due to the tunnel barrier, research towards novel semiconductor materials receives utmost importance and is critical to continue the development of next-generation electronic devices.

With the isolation of graphene in 2004 by Geim and Novoselov [4], the new research field of two-dimensional (2D) materials was established. By studying the physics of elementary particles confined in two dimensions in graphene-based structures, massless Dirac fermions [5], quantum Hall states [6] as well as high electron mobility was discovered. This success led to investigations of other 2D materials with similar lattice structure: covalent bonds forming a few-atoms thin layer in plane, with weak van der Waals (vdW) forces out-of plane. In particular, the family of semiconducting transition metal dichalcogenides (TMDs) emerged with intriguing optical and electronic properties. Similar to graphene, TMDs form a hexagonal lattice structure and possess high electron mobility [7]. Contrary to graphene, which exhibits Dirac cones at the edge of the first Brillouin zone and shows no sizeable

bandgap for multilayer graphene [8, 9], TMDs exhibit a crossover from an indirect to direct bandgap in the visible to infrared energy spectrum when scaled down to the monolayer (ML) limit [10]. Light-matter interaction in TMDs is dominated by excitons [11], electron-hole pairs tightly bound by the attractive Coulomb interaction. The band extrema on opposite sites of the first Brillouin zone (K and K') are referred to as 'valleys' and exhibit opposite spin due to the broken inversion symmetry. In combination with strong spin-orbit coupling, TMDs allow contrasting circular dichroism in different k-space regions [12, 13]. This enables the use of the momentum state of excitons in information processing, introducing a new paradigm called valleytronics [14].

Applications require long-lived, polarised, coherent and addressable states. Many efforts were made to improve the spectral quality of TMDs, where encapsulation in hexagonal boron nitride narrowed down the photoluminescence (PL) linewidth close to the lifetime limit [15–17] and advances in doping control enabled the differentiation between charged and neutral excitonic features [18, 19]. In the particular material WSe_2, these advances revealed novel underlying signatures, where localised excitons, trions as well as phonon sidebands were discussed as origins [20, P1]. In addition, adjacent local band extrema further complicate the peak assignment [21].

This thesis investigates the spectral signatures of momentum-indirect excitons in monolayer and bilayer WSe_2 [P2], where electrons and holes reside in different local minima of the reciprocal space and require the assistance of a phonon for radiative recombination due to momentum-conservation [22]. This phonon sideband luminescence enriches the spectral signatures substantially [P1, 23, 24, P3]. To date, momentum-indirect excitons have been considered predominantly in the context of PL yield and dynamics [25–27], rather than in terms of spectral line-shape analysis. This work, in contrast, relates the pronounced spectral asymmetry to the thermal distribution of excitons beyond the restrictive limit of the radiative cone.

In addition, TMD monolayers may be considered as individual 'Lego' blocks, where numerous material combinations in vertical arrangement may lead to novel physics [28]. As demonstrated for graphene, even two layers with precise angle-controlled stacking reveal new effects like superconductivity [29] or Wigner-crystal formation [30, 31]. TMD heterostructures as a result of vdW-engineering potentially form moiré patterns, a periodic modulation of the real space lattice induced by lattice mismatch and angular displacement [32]. However, due to the interplay of adhesion and strain, defined atomic registries form on a mesoscopic scale [33]. In particular, the material combinations of $MoSe_2$ and WSe_2 exhibits a type-II band alignment which leads to interlayer exciton formation, where the electron and hole reside in their energetically most favourable layer. The spatial separation induces a dipole moment, reduces the wavefunction overlap and thereby gives access to longer radiative lifetimes as well as longer spin coherence times up to microseconds [34].

The second part of this thesis investigates the decoherence mechanism in TMDs, namely

electron-hole exchange interaction [35, 36] described by a Hanle-like spin-dephasing. A minimal rate equation model captures the magnetic field dependent change of the degree of circular polarisation of time-resolved PL stemming from interlayer excitons of a reconstructed uniform atomic registry formed inside a $MoSe_2$-WSe_2 heterobilayer. The distinction between thermal population distribution among Zeeman-split sub bands and injected optical polarisation gives access to the intrinsic spin-coherence times. In combination with optical selection rules and exciton g-factors from theory [33], we identify momentum-indirect interlayer excitons as an intermediate reservoir in the relaxation process.

Overall, this thesis focuses on the light-matter interactions in WSe_2 mono - and bilayers as well as $MoSe_2$-WSe_2 heterobilayer at cryogenic temperatures and aims to add to the understanding of their exciton transitions, phonon interactions and spin-valley polarisation.

Overview

A brief introduction into exciton physics of TMDs is given in Chapter 2. After the description of the crystal structure, electronic properties are discussed with focus on reconstruction effects, exciton g-factors and optical selection rules.

Chapter 3 gives an overview of the experimental methods. We begin by presenting the cryogenic confocal microscope used for our studies, followed by a detailed description of the sample fabrication techniques in inert atmosphere. Exfoliation, identification of layernumbers as well as transfer and assembly into gate-tunable vdW-heterostructures are shown.

Chapter 4 then discusses phonon-sideband luminescence. The charging behaviour of a gate-tunable device consisting of mono- and bilayer WSe_2 was first characterised, before temperature-induced effects such as linewidth broadening and bandgap renormalisation are discussed. The main feature hereby is the temperature dependent asymmetry in the line shape of phonon-mediated transitions. This approach introduces a simple method for the distinction between momentum-indirect and momentum-direct optical transitions in TMDs. The Boltzmann distribution used within our model links the exciton temperature to the spectral asymmetry, where deviations from the crystal temperature were shown and assigned to 'hot' excitons. Such direct experimental access to the temperature of excitons with finite center-of-mass momenta provides additional insight into the fundamental electron-hole recombination processes in atomically thin semiconductors.

In Chapter 5 we first discuss the spectral features of interlayer exciton emission stemming from a $MoSe_2$-WSe_2 heterostructure, with focus on a reconstructed spot where the centers of the hexagon of the crystal structure align in anti-parallel configuration (H_h^h-registry). Polarisation-resolved time-dependent PL provides access to the spin dynamics of the system. The degree of circular polarisation was decomposed into the optically induced spin polarisation and the thermally driven population distribution induced by magnetic field.

This identifies the long-range exchange interactions responsible for spin-dephasing, described by a rate equation model. From minimal assumptions, we extract spin-dephasing times and reproduce the time-dependent degree of circular polarisation. Our approach suggests that momentum-indirect interlayer excitons represent an intermediate reservoir in the relaxation process. The simplicity of our model, together with a good agreement with experimental data, motivates further studies on spin-dynamics of interlayer exctions.

Finally, Chapter 6 provides a summary of the main findings of this work and gives an outlook on future experiments for the understanding of momentum-indirect excitons in WSe_2 and spin-dynamics in TMD based heterostructures.

2 Fundamental aspects of transition metal dichalcogenides

This chapter will give a brief introduction in the relevant physical properties of transition metal dichalcolgenides (TMDs) studied in this work. After introducing the real-space and reciprocal crystal properties for monolayer (ML) TMDs, exciton physics and fundamental aspects of its light-matter interaction will be discussed and expanded to hetero-bilayer TMD systems consisting of $MoSe_2$ and WSe_2.

2.1 Review on monolayer physics

2.1.1 Crystal structure and lattice vibrations

TMDs are a group of about 60 materials of the form MX_2, where M is a transition metal element and X are chalcogen atoms. Most of them have a layered structure in their bulk form with weak interlayer van-der-Waals (vdW) interactions, similar to graphene [4, 37]. In general, these individual layers exist in three different phases, namely 1H, 1T and $1T_0$ [38–41]. This work focuses on group VIB semiconducting TMDs in the most studied 1H phase, consisting of Tungsten (W) and Molybdenium (Mo) as transition metals and Sulfite (S) and Selenide (Se) as chalcogenide atoms. Here, the trigonal prismatic structure with the side view shown in Fig. 2.1 (a), is built by three hexagonal packed planes of covalent bonded atoms in the formation X-M-X, where one X-M-X structure is referred to as a monolayer (ML). This arrangement results in a overall hexagonal lattice structure shown in Fig. 2.1 (b). with an out-of-plane mirror symmetry. The in-plane inversion symmetry although is broken due to the two-atom basis of the unit cell and the symmetry group reduces from D^4_{6h} for bulk TMDs to D^1_{3h} [40]. The weak interlayer vdW bonds between the ML allow for mechanical exfoliation [42] as a top-down approach, however different bottom-up approaches including chemical vapor deposition (CVD) [43, 44], or molecular beam epitaxy (MBE) [45] also create reproducible and high-quality ML crystals.

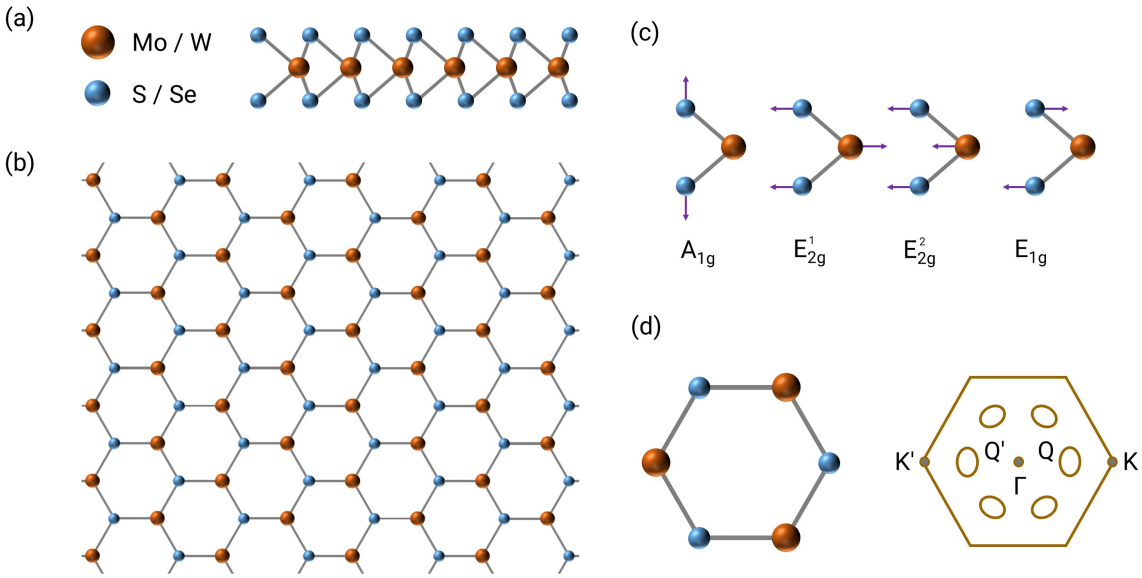

Figure 2.1: (a),(b) Sketch of the real space crystal structure of a monolayer transition metal dichalcogenide (TMD) in side (a) and top (b) view, where the metal atoms are shown in orange and the chalcogen atoms in blue. (c) Four optical Raman active phonon modes most common in TMDs. (d) Illustration of the hexagonal two-dimensional crystal structure with a two-atom basis of the unit cell and it's reciprocal hexagonal representation, where high symmetry points at the corner of the first Brillouin zone (1.BZ) are labelled K/K' and intermediate local minima as Q/Q', with the center Γ.

Lattice vibrations

Small atom displacements in a crystalline structure with three atoms per unit cell occur in 6 possible optical and three acoustical vibrational modes and are described by quasi-particles called phonons. With the distinction between in-plane and out-of-plane modes and additional symmetry analysis [46], one finds that the modes relevant for electron-phonon scattering are the in-plane and in-phase acoustic modes (TA/LA), the optical polar E' (LO/TO) modes, with all three atoms moving out of phase in the plane as well as the energetic highest, out-of-plane optical mode A_1 [47]. The four optical Raman active modes are shown in Fig 2.1 (c), where the indices convention is chosen for bulk MX_2 stuctures. The E_{1g} is forbidden in the typical backscattering Raman configuration [48]. The E^2_{2g} shear mode corresponds the vibration of two rigid layers against each other and is therefore absent in the ML. This effect and other multi-layer corrections are used to identify the exact layer number, as further described in Chap. 3.2.2. Band edge chiral phonons also play a crucial role in the light-matter interaction of TMDs [49, 50] and are further discussed in Chapter 4 in the context of phonon sidebands in WSe_2.

2.1.2 Optoelectronic properties

Independent of the thickness, the hexagonal real-space crystal symmetry in TMDs results in a hexagonal reciprocal lattice, schematically depicted in Fig. 2.1 (d) where the labeled high symmetry points correspond to local extrema in the band structure, referred to as valleys. Interestingly, the MX_2 structures investigated in this work all undergo a direct-to-indirect band-gap transition when thinned down to the ML limit due to quantum confinement in the out-of-plane direction [13, 45, 51]. Bulk TMDs are momentum-indirect semiconductors with the valence band (VB) maximum in Γ and conduction band (CB) minimum in Q [52], where in the ML the resulting band-edge states K and K' at the corner of the first Brillouin zone form a direct band-gap ranging from visible to near-infrared.

The by time-reversal symmetry connected K and K' points are inequivalent due to the two-atom basis of the ML real space unit cell. This breaks inversion symmetry and in combination with strong spin-orbit coupling (SOC), leads to spin-polarised valleys [12, 40, 53]. The main contribution to the VB states stem from the d_{xy} and $d_{x^2-y^2}$ orbitals of the metal atoms. Due to their large angular momentum (l =2, m = $\pm$2), strong SOC splits the VB into two spin-polarised bands separated by hundreds of meV [54]. The CB on the other hand is dominated by the d_{z^2} orbital with m = 0 and therefore no spin splitting is expected in a first order approximation. A schematic of the first Brillouin zone with hyperbolic band dispersion at the K and K' points is shown in Fig. 2.2 (a). However, minor contributions from the p-orbitals of the chalcogen atoms and their interplay with d-orbitals introduce a finite spin splitting of few to tens of meV. The types of atoms, metal and chalcogen, contribute

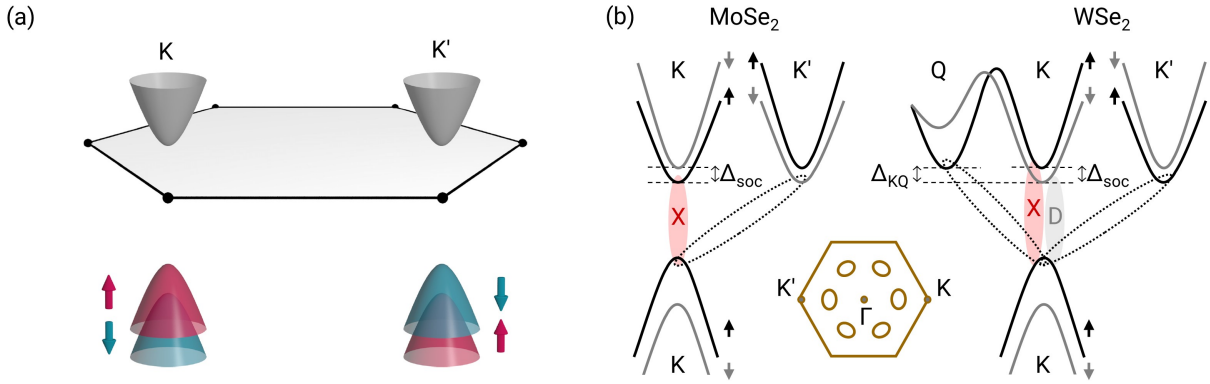

Figure 2.2: (a) Sketch of the first Brillouin zone with band dispersions at the K and K' high-symmetry points commonly referred to as valleys. The strong spin-orbit splitting of the valence band give rise to coupled spin and valley physics in TMDs. (b) Detailed depiction of the bandstructure for $MoSe_2$ and WSe_2. The reversed sign of the conduction band spin-orbit splitting changes the spin ordering and give rise to parallel exciton-spin configurations, spin-bright (X) and anti-parallel, spin-dark (D) excitons, color-coded and labeled accordingly. The dashed ellipses between K/K' and K/Q are symbolising momentum-indirect exciton configurations, where due to momentum mismatch absorption or emission of a phonon is needed for radiative recombination. The spin orderings and population distribution are described by the respective valley-splittings Δ_{KQ} and Δ_{SOC}. Figures adapted from Ref. [61].

to the CB spin splitting with opposite signs [55] and the resulting conduction sub-band ordering is reversed between Molybdenum and Tungsten dichalcogenides [55–60]. As shown in Fig. 2.1(d), the ML shows additional local CB minima at the Q (in literature also called Λ) points, which are pairwise connected by time reversal symmetry. The depth of these valleys is material dependent and varies between $\Delta_{KQ} \simeq 160$ meV for $MoSe_2$ to $0-80$ meV for tungsten-based TMDs [21, 47, 59]. Light-matter interaction in TMDs is dominated by exciton physics. Excitons are quasiparticles formed by the attractive Coulomb interaction between an excited electron and a residual vacancy (hole) in the crystal lattice. The two-dimensional nature of TMD ML causes a reduction of the dielectric screening as other charge carrier are absent in the out-of plane axis. Therefore, Coulomb interactions lead to exciton binding energies E_B^X in the order of ≈500 meV, a dramatic increase compared to bulk TMD or other 3D semiconductors such as silicon and germanium, where typical exciton binding energies are in the order of tens of meV [62]. Excitons behave as hydrogen-like complexes [11] and in TMD ML have a Bohr radius in the nm range, which compared to the lattice constant of ≈ 0.3 nm expands over several lattice unit cells and therefore are classified as Wannier-Mott type excitons. In photoluminescence experiments most relevant for this work, these correlated electron-hole pairs are formed after photon absorption and by recombining, emit light with the energy $E = E_g - E_B^X$, where E_g denotes the energy of the quasiparticle gap between the lowest CB and highest VB.

In first order considering only the momentum direct transitions at K and K', an exciton consists of a hole in the VB and an electron in the CB with spin-parallel (↑↑ or ↓↓) configuration - a so-called bright exciton (X). The optical selection rules are deduced from symmetry analysis and show valley dependent spin orientation . The valley-degenerate excitons couple to $\sigma+$ or $\sigma-$ polarised light respectively, giving rise to the so-called valley-polarisation, defining the optical response [13, 63]. A schematic depiction of the single particle band structure of the 1.BZ of $MoSe_2$ and WSe_2 is shown in Fig. 2.2 (b), where possible exciton configurations are drawn. For $MoSe_2$, due to the sign of the SOC the energetically lowest exciton configuration at K/K' is spin-bright, whereas for WSe_2 the conduction sub-band ordering changes and the spin-dark (D), anti-parallel excitonic state is energetically favoured [64, 65]. In addition, the splitting Δ_{KQ} reduces for WSe_2 and momentum-indirect Q-K excitons contribute to the optical signature via simultaneous phonon emission or absorption following momentum-conservation, and will be discussed in detail in Chapter 4.

2.2 Properties of $MoSe_2$-WSe_2 heterostructures

Part of this section is based on the Publications [33, 66, 67].

2.2.1 Stacking type of commensurate lattices

The TMD crystal properties of individual layers discussed in Chapter 2.1 are now expanded to a Bilayer (BL) system. In general, six atomic registries between two layers form, with additional parameters being the lattice mismatch as well as the rotational alignment. While for now neglecting the former, the latter is most simply classified in R and H-type stacking configurations, where for R-type stacking the in-plane crystalline axes are orientated in the same direction with 0° twist angle and for H-type stacking the direction is inverted due to a 180° twist-angle [65, 68]. With this assignment, Fig. 2.3 follows the nomenclature of Zhao et.al. [33] and displays all atomic registries realisable by lateral displacement, where the labeling refers to the stacking type (R- or H-type, parallel or anti-parallel crystal configuration respectively) and indices are: h = hollow center of hexagon, X = chalcogen site and M = metal site. Here, the different layers are distinguishable by color, where the dashed vertical lines show the exact atomic overlay and the translation from side-view to top-view, displayed below. The natural stacking in bulk TMD is the energetically most favourable H_h^h registry [69], often referred to as 2H symmetry due to its hexagonal nature and two X-M-X layers per repeat unit [46]. Here, the two center of the hexagonal lattices overlap and form an overall pure hexagonal structure with the chalcogenide atoms of the first layer residing on top of the metal atoms of the second layer and vice versa. Other possible high-symmetry

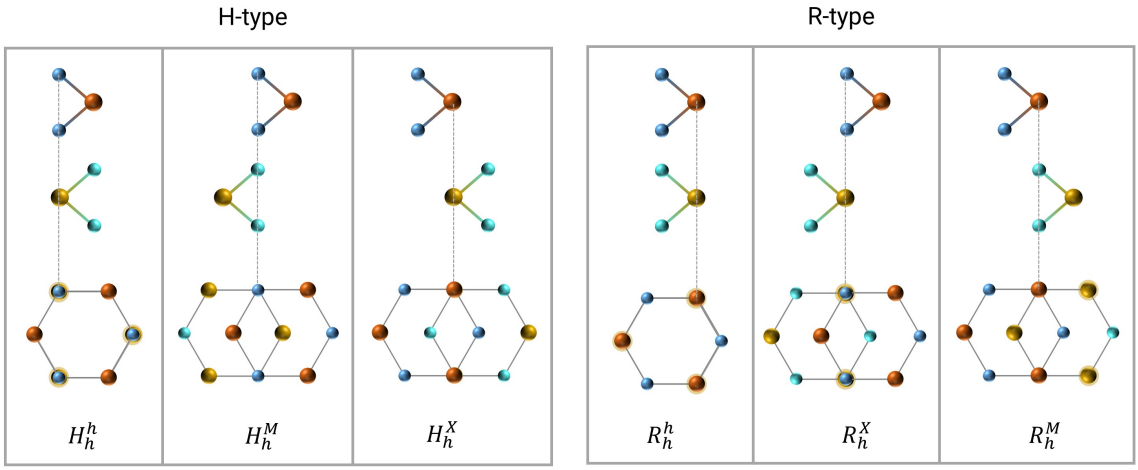

Figure 2.3: Atomic registries realisable by lateral displacement. The labeling refers to the stacking type (R- or H-type) and indices are: h = hollow center of hexagon, X = chalcogen site and M = metal site. Here, the different layers are distinguishable by color, where the dashed vertical lines show the exact atomic overlay and the translation from side-view to top-view, displayed below.

registries of H-type nature are H_h^M and H_h^X, where due to displacement, the center of the hexagons is filled with the metal or chalcogenide atoms of both layers respectively. The R_h^h registry displays the exact overlay of metal and chalcogenide atoms with orientated crystal axis. Remarkably, the R_h^M and R_h^X registries are indistinguishable in the case of homobilayer systems, where both layers consist of the same material. This configuration is also referred to as 3R stacking, where the R-type geometry is expressed by three X-M-X layers per repeat unit to form bulk [46]. With recent advances in CVD synthesis, perfectly aligned high-quality 3R-homobilayer became accessible and in comparison with the natural 2H-stacking, yield new optoelectronic properties [70]. In heterobilayers (HBL) e.g. $MoSe_2$-WSe_2 structures discussed in this work, the vertical ordering and nomenclature is defining the type of metal atom residing in the hexagonal center. The lattice constants between $MoSe_2$ and WSe_2 however, differ by 0.1% [69] and therefore, the assumption of a commensurate lattice is only valid in CVD-grown HBL crystals, since atomic vacancies formed during the growth process counteract the lattice mismatch [71, 72].

2.2.2 Moiré and reconstruction effects in bilayer systems

With the inclusion of rotational alignment between two individual TMD ML, a moiré superlattice is formed as schematically displayed in Fig. 2.4. It consists of a periodic modulation of the atomic registries depicted in Fig. 2.3. The size of the lattice mismatch between the individual layers defines upper boundaries for the size of the moiré lattice and leads to

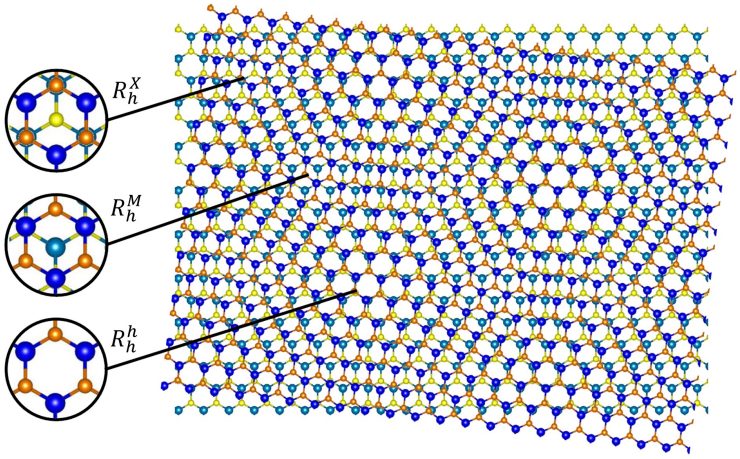

Figure 2.4: Ideal moiré pattern in a $MoSe_2$-WSe_2 HBL with R-type stacking under 4° twist angle. The resulting superlattice consists of a periodic modulation of the atomic registries defined in Fig. 2.3. The lateral dimension of the moiré lattice is dependent of the lattice mismatch and the twist angle. Figure adapted from Ref. [73].

the distinction between commensurate and incommensurate lattices. For commensurate homobilayer with identical lattice constants and zero twist angle, the moiré lattice is absent. In general, the length L_M of the moiré supercell is defined via [74]:

$$L_M(\Theta) = \frac{a_1}{\sqrt{1+(\frac{a_1}{a_2})^2 - \frac{2a_1}{a_2}\cos(\Theta)}}, \Theta \in [-30^\circ, 30^\circ], \tag{2.1}$$

where a_1 and a_2 are the individual lattice constants and Θ is the rotational twist-angle between the two layers with a 60° rotation symmetry. In the case of near-commensurate $MoSe_2$-WSe_2 HBL , this results in an upper limit of $L_M \approx 180$ nm. HBLs with different chalcogen atoms are incommensurate as they show a much higher lattice mismatch. This reduces the upper limit of L_M to $\approx$ 8nm. However, the typical optical spot-size of ~ 1 μm of a diffraction limited confocal microscope used in this work spans over multiple moiré unit cells. Therefore, in the absense of strain and interlayer-adhesion induced relaxation and reconstruction, the optical excitonic response of these systems is probed as a collective overlay of all atomic registries with an additional moiré potential. As the atomic registries alternate spatially, so does the local effective bandstructure and thereby the energy of the interlayer excitons (IX), coulomb-bound, layer-separated electron-hole pairs. This periodic potential modulation leads to localised IX, where correlated physical phenomena like Mott-insulating states were shown in in homo- and heterobilayer systems [30, 32, 75].

The above mentioned description of twist-angle dependent heterobilayer stacking is due to its strong simplifications often called 'powerpoint moiré'. It only occurs if the energetic minima from the interplay of the intralayer strain and interlayer adhesion energy lies above

the moiré induced total lattice energy. Displayed in Fig. 2.5 are numerical results taken from Ref. [33] for incommensurate $MoSe_2$-WSe_2 HBLs. The moiré lattice is shown in a point-like representation, where each atomic registry (H_h^M,H_h^h,H_h^X and R_h^M,R_h^h,R_h^X) is associated with a certain color (see Fig. 2.5 (a), left). These stacking possibilities reduce drastically if one includes the mechanical relaxation patterns of incommensurate BL systems. The sum of intralayer (strain) and interlayer (adhesion) energy is given by the integral over the HBL area S via [76]:

$$\mathcal{E} = \int_S [U(\mathbf{r}) + W_s(\mathbf{r})]\, \mathrm{d}\mathbf{r}, \tag{2.2}$$

where $U(\mathbf{r})$ and $W_s(\mathbf{r})$ are intralayer and interlayer strain energy densities respectively, depending on the in-plane displacements in $MoSe_2$ and WSe_2 layers as well as their elastic properties. On the nanoscale, twisted bilayers relax into periodic domains by rearranging lattice atoms according to a 2D displacement vector field [33, 77], resulting in a periodic reconstructed landscape shown in Fig. 2.5 (a), right. The energetic most favourable domains in case of periodic reconstruction are the hexagonal H_h^h domains for H-type stacking, as well as the energetically degenerate triangular R_h^X and R_h^M domains for R-type stacking.

However, with the introduction of a spatially confined region (numerically through boundary conditions) the periodic reconstructed domains evolve to a mesoscopic domain pattern, with 2D, 1D and 0D regions, shown in Fig. 2.5 (b) for zero twist deformations around the points associated with the dimensionless parameter α numerically defined by the initial conditions, with a total twist-angle $\theta = 0.4°$. The resulting total areal energy given by Eq. 2.1 is evaluated for different twist angles and rotational points α, shown for R- and H-type stacking in Fig. 2.5 (c-d) and (e-f), respectively. These results have drastic consequences for the interpretation of the HBL systems studied in this work, as their size is finite, their twist-angle is small and especially close to edges, mesoscopic reconstruction dominates as it lies energetically below periodic domain formations as well as pure moiré-lattice formation.

2.2.3 Electronic band structure of bilayer systems

After the treatment of the real space properties of bilayer systems above, we now discuss their electronic properties. In general, the direct bandgap in ML TMDs is not longer present for BL systems. The bands at K/K' valleys feature a stronger in-plane orbital character, where in contrast the Γ/Q valleys feature an out-of plane character and are therefore more sensitive to interlayer interactions and orbital hybridisation [78]. For natural homo-bilayers this results in the CB minimum to be found at the reciprocal high-symmetry point Q, where the location of the VB maximum is material dependent. In case of natural 2H stacked WSe_2 homobilayer, the VB minimum is located at K ,only 40±30 meV higher than the Γ-point and thereby exhibits a Q-K indirect band gap [70, P4].

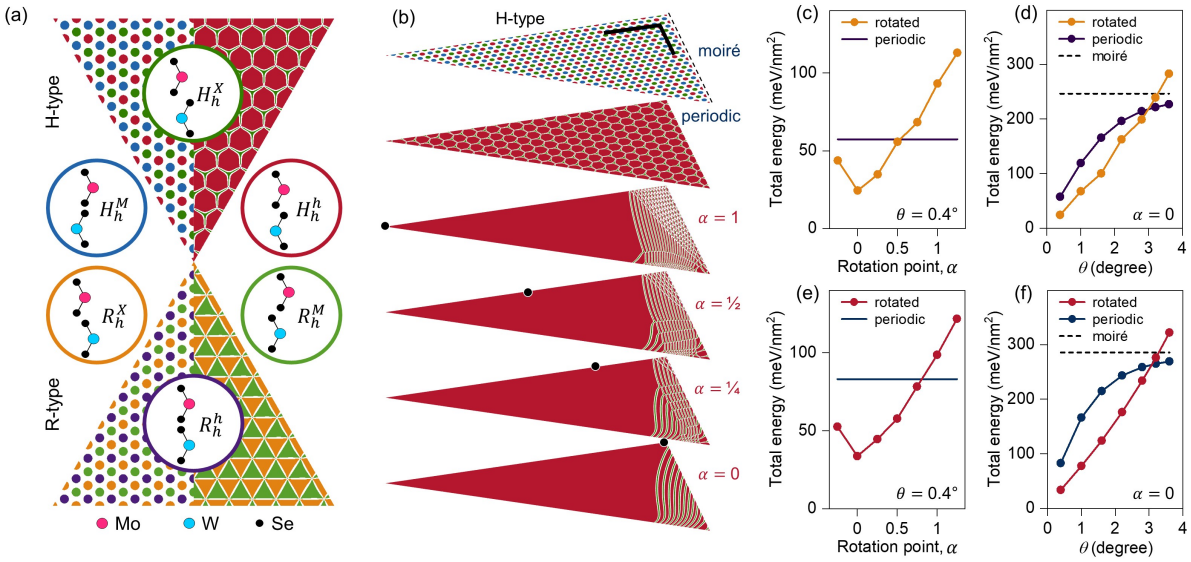

Figure 2.5: (a) Schematic representation of R and H-type registries with ideal moiré (left) and periodically reconstructed (right) patterns, where the coloured regions show high-symmetry atomic registries. (b) Finite size simulation of a triangular shaped HBL for H-type configurations with $\theta = 0.4°$ twist angle and scale bars of 200 nm. Shown in the top panel are moiré patterns. Below, periodic reconstruction with hexagonal domain formation is shown as a result of the interplay of intralayer strain and interlayer adhesion energy. Mesoscopically reconstructed domain patterns are obtained for different zero-twist deformations, where the black dots mark the relaxation initial position, associated with the dimensionless parameter α. (c,e), Total areal energy for R and H-type stacking respectively for different α under a small twist of 0.4°. (d,f) Total areal energy for R and H-type stacking respectively with a variation of θ for $\alpha = 0$. Figure adapted from Ref. [33].

Heterobilayer however have more degrees of freedom due to the choice of material and relative alignment and thereby enable access to band engineering and correlated physical phenomena, e.g. $MoSe_2$-WS_2 HBLs have shown hybridisation of their CBs [79] and in WSe_2-multilayer MoS_2, a restoration of the direct bandgap was demonstrated [80].

The band-alignment in $MoSe_2$-WSe_2 HBLs in contrary, is of type-II, as sketched in Fig. 2.6 (a) and generally understood by the Anderson rule. Here, horizontal grey lines indicate the energetic position of the K and K' valley of $MoSe_2$ and WSe_2 respectively. Intralayer-excitons (X), momentum-direct transitions in the K/K' valley, are formed in $MoSe_2$ and WSe_2 and are sketched by vertical arrows, where the CB energy of the former resides in the bandgap of the latter. This band-alignment leads to a ultra-fast, phonon-mediated and spin-conserving charge transfer processes between the layers, depicted as dashed arrows. The energetically most favourable electron and hole states accumulates the majority of the free charge carriers within tens of femtoseconds [81–83]. As the layer distance is comparable to the exciton Bohr radius ($\sim 1-3$ nm), coulomb interaction, similar to the case of intralayer excitons, leads to the formation of spatially separated but bound electron-hole pairs, which initially are energetic excited and therefore referred to as 'hot' interlayer (IX) excitons. The energetic relaxation and IX formation takes place in $\sim$1 μs and the binding energy is in the order of hundreds of meV. This two-step process is depicted by the diagonal arrow in Fig. 2.6 (a). The resulting real space scheme of an $MoSe_2$-WSe_2 IX is shown in Fig. 2.6 (b), where black arrows display the resulting electric field. From the spatial separation of $\sim$0.5-0.8 nm, the field orientation has a favoured direction and therefore IX exhibit a permanent electric dipole moment in the out-of plane direction, in contrary to intralayer excitons. The next consequence of the layer separation is a reduced wave-function overlap which provides exciton lifetimes up to hundreds of nanoseconds [84], orders of magnitude longer than in momentum-direct spin-parallel intralayer excitons (e.g. ML WSe_2 X-excitons are in the order of$\sim$ ps [25]).

The comparison of the individual bandstructure of $MoSe_2$ and WSe_2 respectively also shows a much higher spin-splitting in the VB of WSe_2 than the contributing CB in $MoSe_2$, leading to a spin-split IX formation in the order of $\sim$ 25 meV, inherited from the ML [55].

However this analysis neglects the interlayer coupling as well as orbital hybridisation and is insufficient to fully describe the electronic properties of HBL. Ab initio calculations using density functional theory (DFT) give additional insights to the bandstructure of HBL, including the above mentioned effects. Based on the DFT results, the Wannier exciton model in the effective mass approximation [85] is used to calculate the exciton energies for different spin-valley configurations, where details of the numerical parameters and following analytical calculations are shown in the supplementary material of Ref. [67]. A stacking specific result is displayed in Fig. 2.6 (c), where the first Brillouin zone is shown exemplary for the R_h^h configuration. The energetic spacing Δ_{KQ} in the CB defines the nature of the excitonic transition - momentum-direct KK (K'K') or indirect KQ (K'Q , KQ', K'Q'),

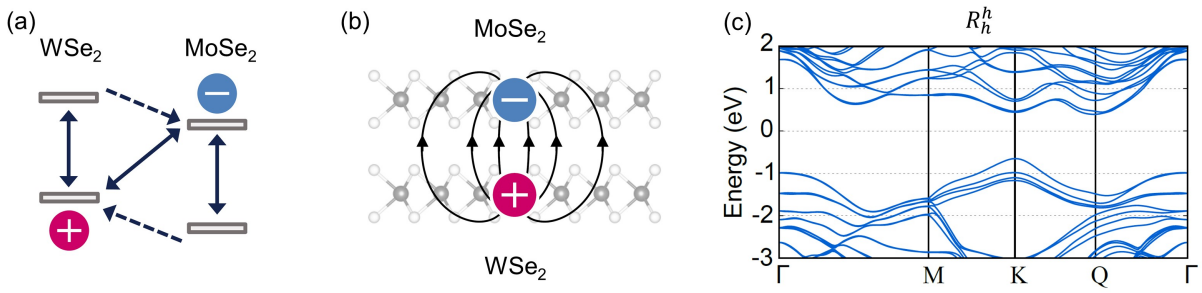

Figure 2.6: (a) Schematic depiction of the type-II alignment of a $MoSe_2$-WSe_2 heterostructure. The vertical arrows indicate the momentum direct intralayer exciton (X) formation, where the dashed arrows symbolise the charge transfer process to the CB minimum and VB maximum for electron and holes respectively, where interlayer excitons (IX) are formed. (b) Real space side-view of a interlayer exciton with resulting electrical field, illustrating the permanent electric dipole induced due to spatial separation. (c) $MoSe_2$-WSe_2 bandstructure from DFT calculation [67] for a respective stacking, namely R_h^h. Figures adapted from Ref. [67, 73].

where stacking dependent theoretical results vary strongly [86, 87]. The inclusion of the above discussed mesoscopic reconstruction in combination with additional insights from the exciton g-factor analysis give access to experimental verification of the valley origin of excitonic transitions, as shown in Chapter 5.

2.2.4 Exciton g-factors

This section is based on the publication [P3].

Each energy band in a crystal, similar to orbitals in atoms, exhibits a magnetic moment that leads to an energy shift proportional to an applied magnetic field. The connected spin-valley physics in TMDs due to inversion symmetry breaking and strong SOC, lifts the energetic degeneracy of the valleys inside a magnetic field. Depending on the spin orientation, the sign of the energy shift changes, causing an energetic splitting, the valley Zeeman effect. The energy splitting Δ_Z is defined by:

$$\Delta_Z = g\mu_B B, \tag{2.3}$$

where B is the perpendicular applied magnet field and g the valley-dependent exciton g-factor. The Bohr magneton $\mu_B = |e|\hbar/(2m_o c)$ is defined through the electron charge e and mass m_0, the reduced Planck constant $\hbar$ and the speed of light c.

We start from a crystal electron in a Bloch state $\psi_{nk} = S^{-1/2} exp(ikr) u_{nk}(r)$ with energy E_{nk}, n indicating the band number and k being the wave vector. $u_{nk}(r)$ represents the periodic Bloch amplitude and S the normalisation area. The first order correction to the

electron energy induced by a static magnetic field B is given by [88]:

$$V_n(k) = \mu_B B[g_0 \mathbf{s} + L_n(k)], \tag{2.4}$$

where the expression in square brackets is often called effective magnetic moment and consist of a spin and orbital contribution. The first term , where $g_0 \simeq 2$ describes the free Landé g-factor, and $\mathbf{s} = \sigma/2$ the spin-angular momentum, with σ denoting the Pauli matrix.

The second term describes the orbital angular momentum $L_n(k) = \langle \psi_{nk} | \mathbf{L} | \psi_{nk} \rangle$, with $\mathbf{L} = \hbar^{-1}[r \times p]$ as the corresponding operator. Its matrix elements are obtained by reducing the calculation to the interband matrix elements, numerically solved within the DFT calculations further described in Ref. [P3, 33].

With the restriction of the magnetic field to the z-axis, we define the electron Zeeman splitting as the energetic difference between the electron state with wave vector +**k** and spin projection +s and the state -**k**, -s as:

$$\Delta_n(k) = V_n(+\mathbf{k}) - V_n(-\mathbf{k}) = 2\mu_B B[g_0 s + L_n(\mathbf{k})]. \tag{2.5}$$

Therefore, the electron g-factor of the n-th band is:

$$g_n(\mathbf{k}) = \frac{\Delta_n(\mathbf{k})}{\mu_B B} = \pm g_0 + 2L_n(\mathbf{k}), \tag{2.6}$$

where the sign depends on the spin z-projection $s = \pm 1/2$ ($\uparrow$ or $\downarrow$). Neglecting electron-hole Coulomb interactions, the exciton Zeeman splitting simplifies to the sum of the Zeeman splitting of the electron and the hole. Therefore, the exciton g-factor is obtained as:

$$g^{(cv)}(\mathbf{k}_c, \mathbf{k}_v) = g_c(\mathbf{k}_c) - g_v(\mathbf{k}_v), \tag{2.7}$$

where time-reversal symmetry relates spin and wave vector of an empty electron state to the hole via $s_h = -s_v$ and $\mathbf{k}_h = -\mathbf{k}_v$. From the numerical values of the z-projection of $L_n(k)$, together with the spin orientation of each valley, g-factors of spin-like and unlike as well as momentum-direct and indirect excitons are calculated [P3].

2.2.5 Optical selection rules in $MoSe_2$-WSe_2 heterobilayers

To obtain the spin-orientation of each valley as well as the resulting polarisation of light, optical selection rules deduced from symmetry analysis of atomic registries are used. A detailed description and derivation is found in the Appendix of Ref. [73] and in the supplementary information of Ref. [66]. In brief, the electron Bloch functions at high-symmetry points are defined by the stacking of the real space lattice and translated into irreducible representations in Koster notation $\Gamma_n (n = 1, ..., 6)$ [89]. Taking into account the spin part,

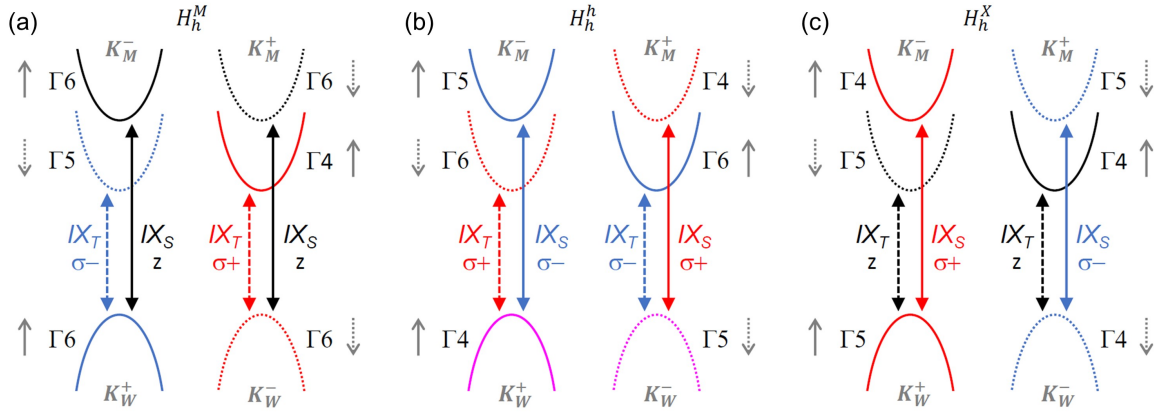

Figure 2.7: Optical selection rules for a $MoSe_2$-WSe_2 H-type HBL in the single-particle band diagram at K and K' points for the (a) H_h^M, (b) H_h^h and (c) H_h^X atomic registry. Momentum-direct IX are formed between the K/K' -point in the VB of WSe_2 and the two CB in $MoSe_2$, denoted as $K_{W/M}^{+/-}$ respectively. Spin alignment is indicated by arrows, with resulting dipolar transitions IX_T and IX_S, shown in color-coded polarisation (black: z, red: σ^+, blue: σ^-, magenta: σ^+ and σ^- -polarization supported). Figure adapted from Ref. [66].

the Bloch amplitudes are recast as spinor representations of the VB in WSe_2 and the CB of $MoSe_2$ respectively, where the optical transitions are then derived by $\Gamma_c \times \Gamma_v^*$ and result in three possible transitions: σ^+, σ^- and z-polarisation [36]. Here, * denotes the time-reversed representation used to relate electron-states to holes, with $\Gamma_c(\Gamma_v)$ being the irreducible representation of the CB (VB) respectively.

The spin orientation and resulting polarisation for transitions at the K /K' points is shown in Fig. 2.7 for three atomic registries (see Fig. 2.3) in H-type stacking. The R-type stacking mainly differs in the alignment of the K-K and K-K' valley stemming from the $MoSe_2$ CBM and WSe_2 VBM, originated by the π-rotation in real space. Momentum-direct IX are formed between the K/K'-point in the VB of WSe_2 and the two CB in $MoSe_2$, denoted as $K_{W/M}^{+/-}$ respectively. The spin alignment for parallel ($\uparrow\uparrow$ or $\downarrow\downarrow$) and anti-parallel ($\uparrow\downarrow$ or $\downarrow\uparrow$) configuration is classified in triplet and singlet-interlayer excitons, denoted as IX_T and IX_S respectively, and linked to the polarisation of the dipolar transition.

2.2.6 Summary

Finally, this section briefly summarises the results from DFT calculation as well as optical selection rules. An overview of the relevant stacking dependent theoretical IX properties of $MoSe_2$-WSe_2 HBL is summarised in Table 2.1 [33]. The transition energies are experimentally verified by photo-luminescence(PL) experiments. The oscillator strength defines the probability of absorption or emission between energy levels and is proportional to $\sim |\mu|^2$, where $|\mu|$ is the electric dipole moment in Deybe from DFT. The polarisation of the exciton

	Singlet				Triplet			
Stacking	Energy	$\|\boldsymbol{\mu}\|$	Pol.	g-factor	Energy	$\|\boldsymbol{\mu}\|$	Pol.	g-factor
R_h^X (optimal)	1.33	1.47	σ_-	+5.8	1.35	0.70	σ_+	-10.5
R_h^h	1.38	2.06	σ_+	-6.4	1.40	0.19	z	11.0
R_h^M (optimal)	1.48	1.09	z	6.3	1.50	0.02	σ_-	+10.9
H_h^M	1.39	0.40	z	13.1	1.37	0.10	σ_-	+17.6
H_h^X	1.41	0.69	σ_+	-13.2	1.39	0.40	z	17.7
H_h^h (optimal)	1.42	2.14	σ_-	+12.9	1.40	0.42	σ_+	-17.6

Table 2.1: Theoretical results from DFT calculations and symmetry analysis for different atomic registries in $MoSe_2$-WSe_2 HBLs for singlet and triplet interlayer excitons. The energetic optimal stackings are marked accordingly. Transition energy is given in eV, where values are taken from Ref. [90]. The electric dipole moment $|\mu|$ is a measure of the oscillator strength, obtained by DFT calculations and given in Deybe. The dipole transition polarisation (Pol.) is deduced from the optical selection rules. The dimensionless g-factors are obtained from DFT (see Sec. 2.2.4). Results are reproduced from Ref. [33].

transition is calculated from the optical selection rules, shown exemplary in Fig. 2.7. The g-factors are calculated for the respective bands from the orbital angular momentum $L_n(\mathbf{k})$ obtained by DFT, via Eq. 2.6 and 2.7. With polarisation resolved magneto-luminescence experiments as shown in Chap. 5, these values are probed - an ideal example where the interplay of theory and experiment leads to additional insights into optical transitions.

3 Experimental methods

The following chapter will first discuss the experimental optical setup used for the cryogenic photoluminescence studies in this dissertation. Then, fabrication techniques for van der Waals heterostructure assembly from TMD and hBN bulk crystals to a gate-tunable device are presented in detail.

3.1 Cryogenic confocal microscopy

To investigate the optical properties of TMD heterostructures at cryogenic environments, a home-build fibre based confocal microscope was used in back-scattering geometry, as shown in Fig. 3.1. Optical excitation is provided with different light sources, particularly continuous wave lasers (MSquared SolsTiS or laser diodes) and pulsed laser (NKT Super K Extreme), for spectrally resolved and time-correlated PL measurements respectively. The laser light is coupled to an optical single-mode fibre and connected to the setup. The confocal microscope is built with collimators matching the numerical aperture (NA) of the singe-mode fibre (NA ~0.13) on the fibre side and a low temperature apochromatic objective (attocube systems, LT-APO/LWD/NIR/0.63 and Cryo-glass VIS) with a confocal spot-size of ~1 μm on the sample side. A set of linear polarisers as well as $\lambda/2$ and $\lambda/4$-waveplates allow full control of the light polarisation for excitation and detection. A short-pass filter in the excitation path blocks additional Raman signal stemming from the fibre and a long-pass filter blocks the reflected laser light, such that only the emission from the sample is collected inside the detection fibre. Beamsplitter (10:1) guide the light towards the sample and allow additional photodiodes and cameras for alignment purposes. For PL measurements, the emitted light was dispersed by a monochromator (Princeton Instruments Acton SP 2500) and recorded with a nitrogen cooled charge-coupling device (CCD, Princeton Instruments PyLoN). For time-resolved measurements, avalanche photodiodes (APD, PicoQuant τSPAD) with a temporal resolution of 0.6 ns were used. The sample was mounted on a titanium

holder on top of a piezo nanopositioner with three spatial degrees of freedom (attocube systems ANPxy101 and ANPz102), forming a so called 'piezo-stack'. This stack was mounted below the objective, where the z-position was matching its working distance as well as the maximum of the magnetic field (up to 9 T) stemming from the superconductive coils inside the dry closed-cycle cryostat at 3.2 K (attocube system, attodry1000). Below the sample, an additional photo-diode may be installed for transmission measurements. Also, next to the sample on the titanium holder, additional resistances provide an effective way for temperature control and measurement (Allen-Bradley, 1 kΩ). The sample, together with the nanopositioner and objective were placed inside a dewar with inert helium atmosphere with a pressure of 20 mbar to ensure thermalisation with the surrounding bath temperature. Also, all possible electrical connections with the sample are guided in twisted pairs of copper-cables through the dewar and thereby enable motion, temperature and doping control.

3.2 Fabrication of van der Waals heterostructures

First experiments of two-dimensional materials were based on mechanical exfoliation. Even though the Nobel laureates Andre Geim and Konstantin Novoselov did receive the price for the astonishing physical properties of graphene [4, 5] and not its isolation and fabrication, the simplicity of it is beautiful. A simple scotch-tape put on a pencil and repeatedly torn apart eventually results in a single-atom thick 2D-crystal. Monolayer may be considered as individual 'Lego' blocks, where numerous material combinations in vertical arrangement may lead to novel underlying physics [28].

Van der Waals heterostructures consistent of multiple monolayers of TMDs, dielelectric passiviation layers and graphene gain immense attention in the last years [4, 92, 93]. The mechanical exfoliation is by default inherently limited in its scalability for industrial applications. We briefly give an overview of alternative promising methods to solve this issue, before describing all fabrication processes used in this work in more detail.

TMD synthesis like chemical vapor deposition (CVD) result in increasing quality and size of monolayers reaching wafer scale [94, 95] and enable direct heterostructure growth [71]. Efforts towards patterned CVD-growth on surface-modified substrates has shown promising results [96], where other works with gold-assisted mechanical exfoliation also achieved mm-sized, patterned ML fabrication and transfer [24, 97]. Graphene, with some years of head start compared to TMDs, made the transition into industry with applications raging from electrical devices(e.g. OLEDs and screens [98]) to coatings of sport products for increased durability [99].

TMDs on the other hand are on the verge of industrialisation, where semiconductor foundries (Graphene Flagship, 2D-EPL) are starting multi-project wafer runs for proto-

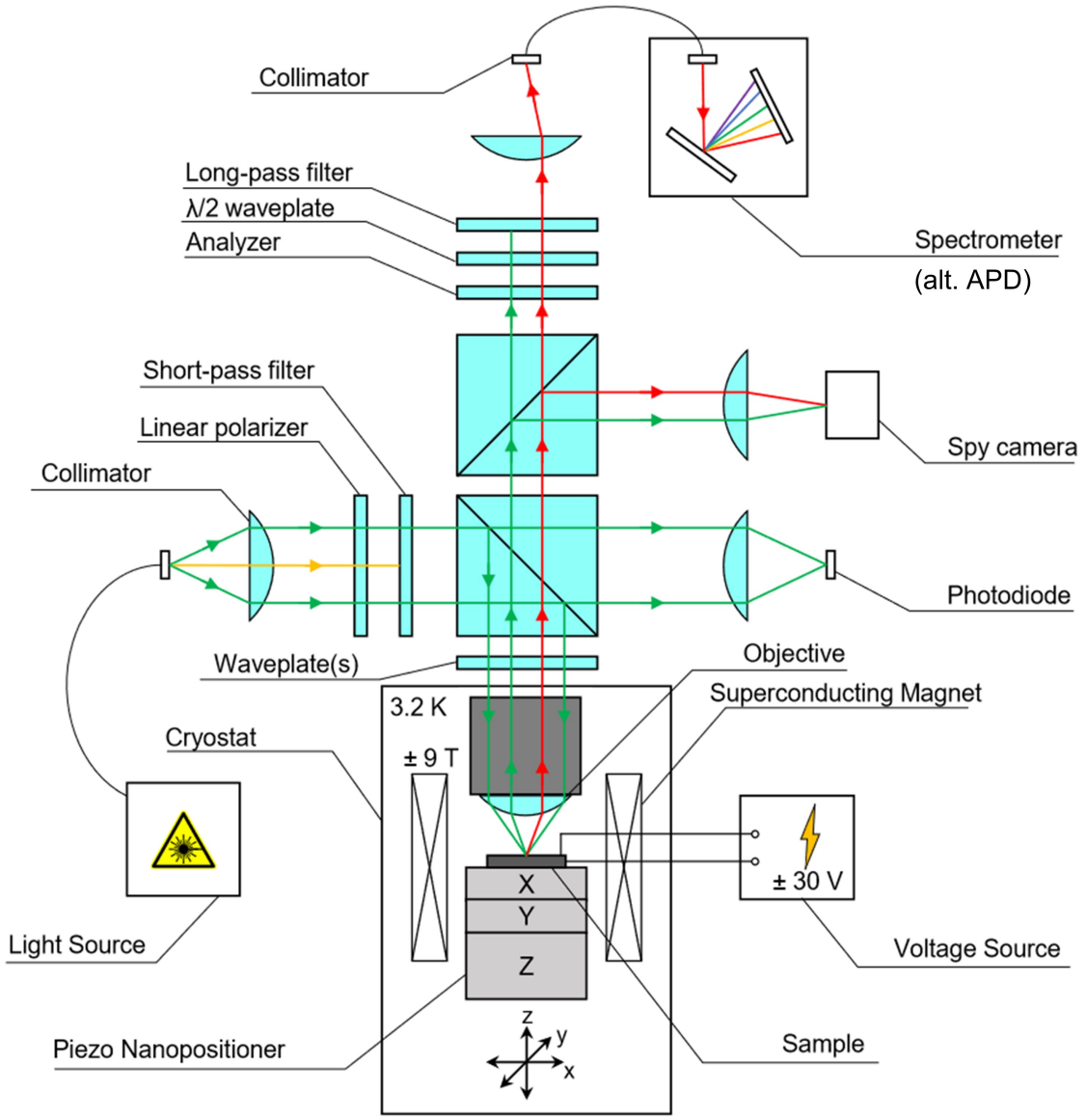

Figure 3.1: Optical setup consisting of a fibre-based confocal microscope used for PL spectroscopy and a closed-cycle cryostat with a base temperature of 3.2 K. The sample was mounted on top of piezo nanopositioners on a titanium-holder and placed inside the cryostat at the center of the magnetic field up to ±9 T, induced by the superconducting coils in Faraday geometry. Green lines are the excitation light directed at and reflected from the sample, whereas red lines show the emitted light by the sample. Raman signal from the fibre is blocked by the short-pass filter, whereas reflected light is blocked by a long-pass filter before detection. Additional motorised $\lambda/4$-plates are mounted below the beam-splitter and in the detection arm to access polarisation-resolved PL. For spectroscopy, a monochromator in combination with a CCD was used, whereas for time-resolved measurements, the detection fibre was coupled to an APD. Figure adapted from Ref. [91]

type chip integration. From research side, current trends for example go towards electrical computing with MoS_2-based field-effect transistors [100] as well as photonic applications, where TMDs show promising results as active phase-shifter [101]. Also, in the exploration of endless combination of 2D semiconductors, there is an urgent need for fully automatised fabrication, including not only ML production, but transfer and assembly as well as post-treatment [102–104].

For studies of light-matter interaction in this thesis, this section will focus on the manual, mechanical exfoliation and assembly of mono- and few-layer TMDs with hexagonal boron nitride (hBN) into gate-tunable vdW-hetereostructures.

3.2.1 Fabrication setup in inert gas atmosphere

Nobel laureate Herbert Kroemer coined the famous phrase “the interface is the device" and was referring to the advances in thin-film semiconductor fabrication and application [105]. In all processes towards a vdW-heterostructure consisting of multiple, often below 1 nm thick 2D-surfaces, this is absolutely true. Therefore to ensure the maximum sample quality by preventing oxidation effects [106], water deposition [107] and eliminate dust or other contaminants which may accumulate on the crystal surface, an inert atmosphere is of essence.

Therefore, we designed a dedicated setup based on a Glovebox for high-quality fabrication of functional devices based on two-dimensional materials. The Glovebox Setup was provided by MBraun (Unilab PLus) as shown in Fig. 3.2 and operated with argon-gas in overpressure conditions. The automated gas-cycle system consisting of reactor, heat-exchanger, activated carbon as solvent filter and Hepa-dust filter reduced the total gas-exhaust, where the atmosphere purity was continuously monitored by H_2O and O_2 sensors and kept below 1 ppm respectively. Motorisation is a crucial factor, as the handling of samples with tweezers or mechanical fine-adjustment of motion stages with gloves is limited. Therefore, as shown in Fig. 3.2 (b), a microscope (Olymus) was customised with a motorised focal axis, two optical camera ports, and installed above two piezo-nanopositioner stacks (attocube systems, ECS series) to function as a transfer setup, described in more detail in Section 3.2.4. All electrical and optical interconnect cables have to be mounted inside a flange to hermetically seal the system. The working area shown on the right hand side consists of a hot plate, cutting mat and an adhesive substrate region and was used for exfoliation of bulk crystal into thin films, discussed in the next section.

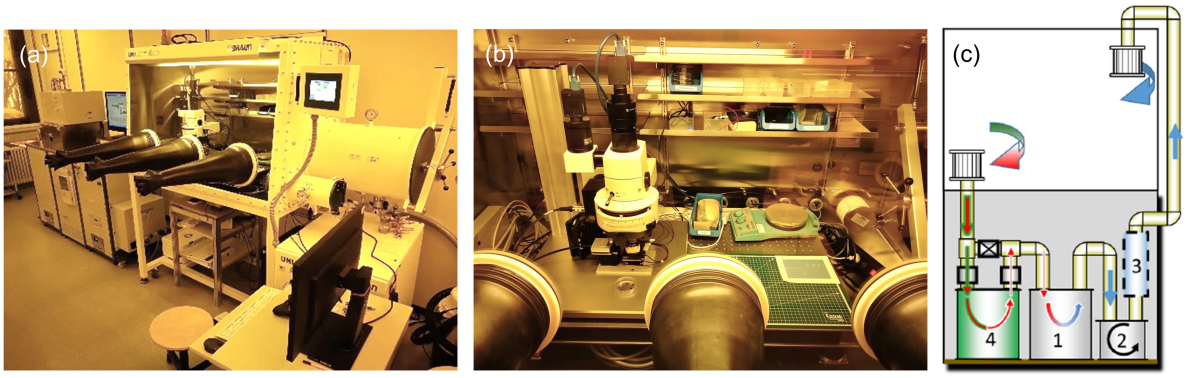

Figure 3.2: Exfoliation and Transfer-Setup in inert atmosphere. (a) Glovebox Setup by MBraun in Ar over-pressure operation, with motorisation control from the Desktop PC, two air locks and a automatised regeneration cycle through a gas-purifier reactor. The system includes O_2- and H_2O sensors as well as Hepa dust filter. (b) Left: μm-transfer setup including full motorised nano-positioner and a motorised optical microscope. Right: Exfoliation setup including a hot plate, dedicated region for tape-exfoliation and a adhesive substrate region to facilitate the tape removal under the reduced fine motor skills with gloves. (c) Schematic of automatised gas-recycle system, with in and output of the inert gas (Ar) though Hepa-dust filters. The cycle consist of i) Gas regeneration by the reactor, ii) Blower, iii) Heat-exchanger for temperature stabilisation and iv) an additional solvent filter consistent of activated carbon.

3.2.2 Mechanical exfoliation and identification of few-layer transition metal dichalcogenides

Micro-mechanical exfoliation, often referred to as "Scotch-Tape method", was established as an intuitive and simple top-down approach to isolate mono- and few-layer TMDs from bulk crystal. The name refers to the tape first used for graphene exfoliation [4] twenty years ago, where an adhesive tape was brought into contact with bulk graphite, pulled off and then with a second tape, repeatedly brought into contact and peeled off, such that a visible large area on the tape was covered with crystal residues. Fig. 3.3 (a) and (b) visualises the similar procedure, where Nitto Tape BT-150P-LC was brought into contact with bulk material provided by HQ Graphene ($MoSe_2$, MoS_2, WSe_2 or WS_2) and removed such that a small piece of bulk adheres to the tape. A second tape is then matched and pressure is applied to ensure contact and reduce air blisters to maximise the adhesive forces between the tapes. After the tapes were pulled apart, this procedure is repeated three to four times until a sizeable area is covered with crystal regions of varying thickness and size, the so called "flakes".

The tape is finally brought into contact with a target structure, in our case SiO_2/Si chips, where we used 80-85 nm oxide layer for optimised optical contrast of TMD ML as well as graphene [108, 109]. Slow and steady removal of the tape transfers stochastic distributed flakes onto the SiO_2 surface, as shown on the bright-field microscope image in Fig. 3.3 (d). The yield of transferred flakes is increased by heating the chip in contact with the tape at ~100 °C on a hot plate for 2 min and subsequent cool-down [42], at the cost of increasing tape-residues. Also, plasma-treatment of the SiO_2/Si chip shortly before tape contact increases the adhesive forces but also introduce trapped charges in oxidised silicon. This modified doping level of the substrate later on strongly affect the samples behaviour in cryogenic PL measurements and therefore was omitted [110]. It is elusive if few-layer TMDs found on the SiO_2/Si surface stem directly from the tape or were cleaved from larger flakes on the tape to the substrate, were the latter would result in cleaner interfaces and therefore, quality control of all flakes used for subsequent fabrication techniques is of essence.

As monolayer TMDs investigated in this work all show strong photoluminescence (PL) at room temperature, their identification and distinction e.g. between mono- and bilayer as well as their optical uniformity, PL-imaging was implemented into the Olympus-microscope installed inside the glovebox, similar to Ref. [111, 112]. A combination of short and long-pass filter (Thorlabs, FESH0550 and FELH0600) were installed inside a filter module of the microscope (see Fig. 3.4 a), such that the LED light source used for bright-field microscopy was converted into a broadband excitation source, while blocking wavelengths in the range of PL response (Fig. 3.4 c). This facilitated the identification and characterisation immensely, as after a manual search for ML candidates, simply the filter-wheel and the CCD camera was switched to a monochromatic CCD with higher quantum efficiency (Point grey, GS3-U3-14S5M) for confirmation. Figure 3.4 (d-g) show exemplary bright-field and PL images from

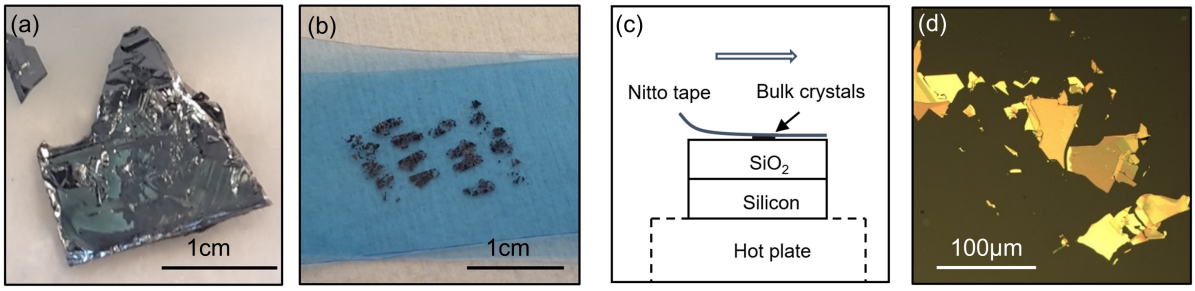

Figure 3.3: (a) Bulk crystal of MoS_2. (b) Nitto tape after exfoliation from bulk and repetitively exfoliation to a sizeable area covered with crystal layers. (c) Schematic illustration of the final exfoliation step. Contact of the SiO_2/Si substrate with the prepared tape and subsequent remove is leading to direct exfoliation of layered crystals onto the substrate. Indicated hot plate is optionally used for 2 minutes at 100°C to increase the adhesive forces between the two interfaces, leading to a higher yield of exfoliated and transferred flakes but induces also tape residues. (d) Optical bright-field microscope image of MoS_2 crystals on top of SiO_2/Si.

the same spatial location of an exfoliated WSe_2 ML and CVD grown $MoSe_2$, both confirming ML thickness as well as revealing cracks, bubbles and residues for the latter.

With an optical contrast up to 10% for ML TMDs [109] depending on the SiO_2 thickness, they are clearly distinguishable from the substrate. The differentiation between bi- or tri-layer although is not straightforward. Atomic force microscopy (AFM) has a limited utility to determine the number of layers, as the theoretical lattice constant of ≈ 0.3 nm result in measured heights up to multiple nanometers for ML due to their elevated height from tape residues, water molecules or measurement error [107]. Raman spectroscopy hereby resolves this issue and provides a powerful tool in determining the exact number of layers of the exfoliated TMDs [46, 113, 114]. Four active Raman modes, three in-plane modes E_{1g}, E^1_{2g} and E^2_{2g} as well as one out of plane mode A_{1g} show strong shift in frequency or intensity variation as a function of layer-number. Figure 3.5 gives an overview of all studied TMDs, where optical contrast from bright-field images is directly compared with PL images and Raman-measurements carried out in a room-temperature home-build microscope similar to Fig. 3.1. Especially the distance between the E^1_{2g} and A_{1g} mode determines the layer number for $MoSe_2$, MoS_2 and WS_2 [114, 115]. WSe_2 shows no separation between the E^1_{2g} and A_{1g} mode but a peak located at around 308 cm^{-1}, possibly a combination of a shear mode with the E^1_{2g} mode, and absent in ML crystals [114, 116]. PL-images confirm the layer-number and identify monolayer as well as bilayer TMDs, where the intensity reduction from the bilayer in the order of ~5-20 is in agreement with literature [13, 42, 116]. The inset reveals a trilayer of WSe_2, where integration time was adjusted for the ~100 times lower PL intensity compared to the ML.

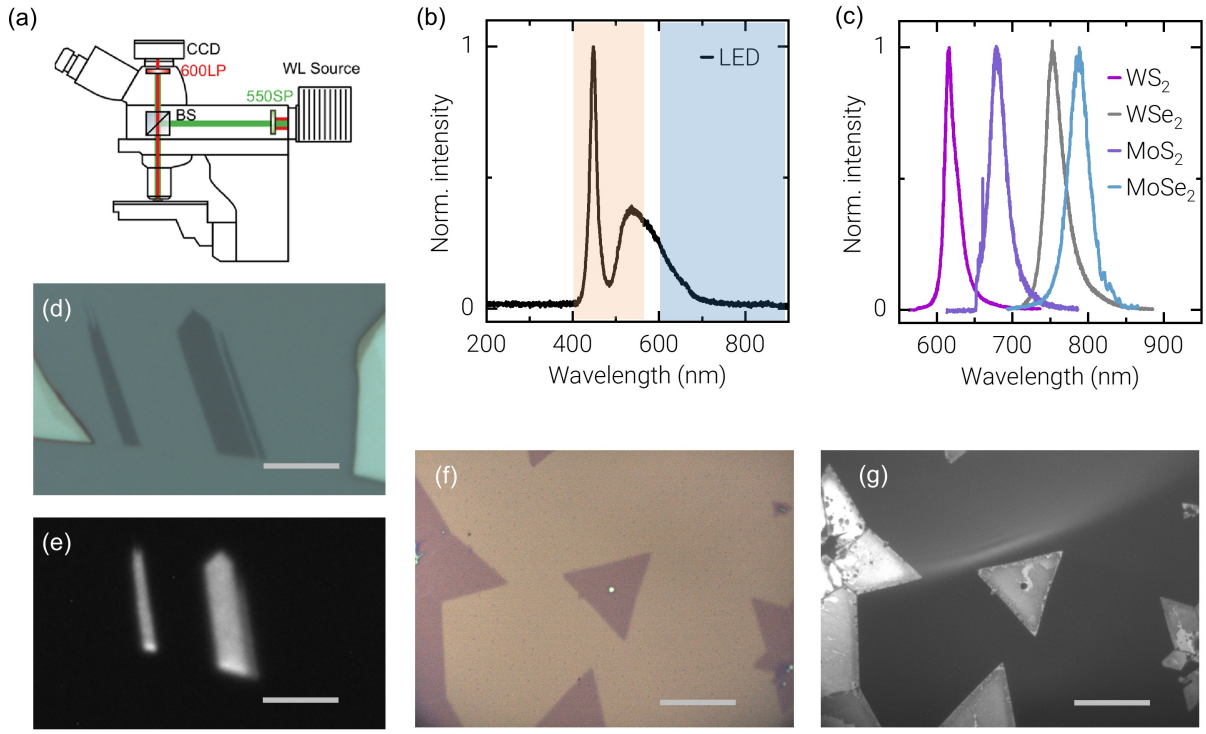

Figure 3.4: PL imaging setup and monolayer characterisation. (a) Schematic representation of the PL imaging setup consisting of a bright-field optical microscope modified with a combination of long- and short-pass filter for photo-excitation and luminescence detection via a CCD camera. Figure adapted from Ref. [112]. (b) Spectral distribution of the LED white-light source, where short- and long-pass transmission regions are indicated by color (orange and blue respectively). (c) PL spectra of four different ML of the TMD family on a SiO_2/Si substrate at room-temperature under 530 nm excitation in a confocal microscope. (d-e) Bright field image of a WSe_2 ML on SiO_2/Si in direct comparison to the PL image under 1s integration with gain settings to maximum, where in (f-g) the PL imaging setup was used to characterise the quality, homogeneity and chemical composition of CVD grown $MoSe_2$ ML on SiO_2/Si under 6s integration. Scattered light stemming from the leakage through the optical filters is partially covering the image on the top left corner. Scale bar is 30 μm.

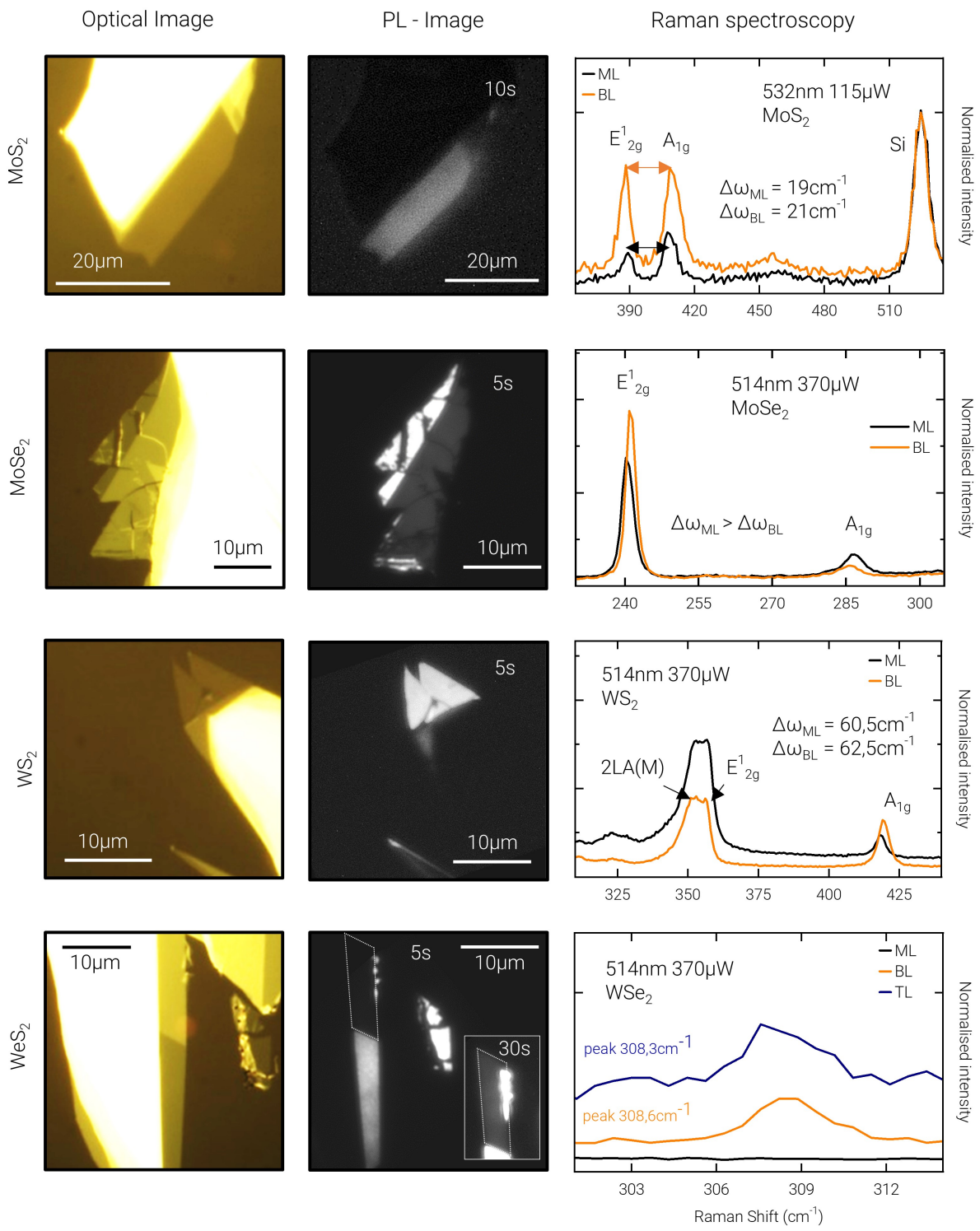

Figure 3.5: Comparison of optical bright-field images of flakes on PDMS with PL-images and Raman spectroscopy measurements to identify and differentiate between mono- bi- and trilayer TMDs. Figure adapted from Ref. [117].

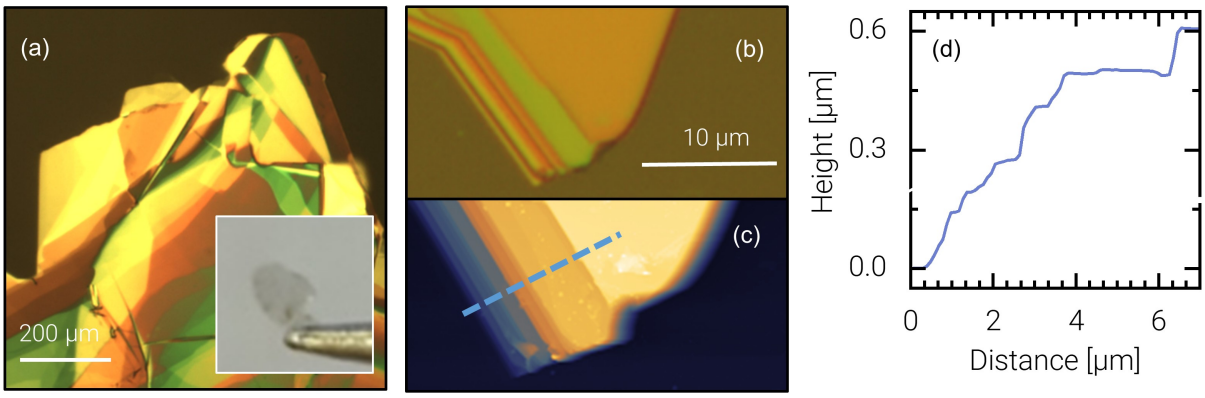

Figure 3.6: (a) Optical microscope image of exfoliated hBN on a SiO2/Si substrate. The inset shows a typical bulk crystal approximately 1 mm in diameter. (b) Extended picture of a typical edge on a large hBN flake, where AFM data (c-d) relates color to thickness. The blue line in (c) marks the spatial position of the height-profile shown in (d). Figure adapted from Ref. [117].

3.2.3 Hexagonal boron nitride

On the search for the ideal dielectric environment for 2D materials, insulating hexagonal boron nitride (hBN) with a indirect bandgap of 5.95 eV [118], low dielectric constant [119] and atomically flat and passive interface, drastically increased the quality of graphene [120] and TMD based devices. Encapsulation of TMDs with hBN led to a linewidth reduction at cryogenic temperatures close to the intrinsic life-time limit [15, 121] and enabled the study of multiple PL sub-peaks especially for tungsten based TMDs [P2, 122, 123].

The real space lattice of hBN, in analogy to TMDs and contrary to cubic boron nitride, consists of boron and nitrogen atoms strongly bond with covalent forces in-plane, forming a hexagonal single-atom wide lattice structure with vdW forces in-between layers [124]. Mechanical exfoliation from bulk crystal is done in analogy to TMDs as shown in Sec. 3.2.2 although the optical contrast induced per layer is significantly smaller [125]. Also for larger flakes, the key challenge is to identify the correct thickness of hBN needed e.g. either for cavity experiments as spacer directly, or to optimise for the exciton lifetime in TMDs [126]. Figure 3.6 shows the underlying problem on two exemplary hBN flakes; the resulting color in bright-field images is repetitive as multiple thicknesses lead to similar contrast values [127]. Atomic force microscopy gives the simplest solution by measuring the height directly (Fig 3.6 b-d). With careful observation of the flake edges and in the absence of color repetition, one is able to match contrast to height for flakes below 100 nm thickness.

3.2.4 Heterostructure assembly

Minimising disorder on and inside all 2D layers involved in the fabrication of vdW heterostructures is crucial and already starts with the choice of bulk crystal synthesis [128]. After exfoliation, identification and characterisation of all individual building blocks, the assembly involves multiple transfer steps. The key challenges are not only the detachment of these materials from their substrate, but also the deterministic positioning onto the target substrate while maintaining ultra-clean interfaces. Techniques ranging from wet-transfer involving etching or electro-chemical treatments to dry-viscoelastic stamping with various polymers as adhesive layers were hereby exploited by the community, where the biggest challenge remains the scalability for industrial application [129].

For heterostructure assembly in this work, we focus on dry viscoelastic stamping as it is most applicable to mechanical exfoliated flakes and with careful flake selection and parameter tuning, it results in the cleanest interfaces as no additional wet chemistry is involved. Early works demonstrated deterministic dry transfer of 2D materials by using a transparent glass-slide covered with a polydimethylsiloxane (PDMS) block, where with careful mechanical control, the adhesive forces of the PDMS were used to peel off flakes from their substrate and transfer them onto a target position and substrate of choice [130]. However, PDMS residues were still limiting the device performances and bubbles, trapped air and water molecules between the interfaces induced additional inhomogenities.

Methods exploring PDMS-treatment e.g. with UV-ozone [131] or the coverage of PDMS with various polymers were investigated. The latter, especially in combination with temperature control of the stack resulted in fast, clean transfer as the adhesive forces between different polymers and the crystal interface is a function of temperature, especially close to the melting point of the polymer [110, 132–134]. Also, instead of using square blocks of PDMS as the underlying elastomer acting as buffer-material, droplets of PDMS showed not only additional control of the contact interfaces, but also function as a lens [127, 135].

Stamp preparation

Figure 3.7 shows a step-by-step guide for stamp preparation used for the dry transfer. First, PDMS with curing agent (SYLGARD$_T$ M184) was mixed in a mass ratio of 10:1 and placed in vacuum for 15 min to remove air bubbles inside the mixture. Next, a glass slide was covered with a drop of the liquid with a diameter of ~1 cm and a height of ~4 mm. Then, the PDMS was dried upside down over a hot-plate at 140 °C for 20 min, followed by room-temperature storage over night (Fig. 3.7.1). A polycarbonate (PC) solution (6% in chloroform) was then dropped onto a glass slide and flattened by a second glass slice, pressed and parallel pulled away, leaving a thin-film PC-polymer on both slides [133] (Fig. 3.7.2). A squared region matching the size of the PDMS droplet was then cut out from a tape and then used to peel off the PC-film from the glass slide. An additional, similarly prepared double-sided tape was

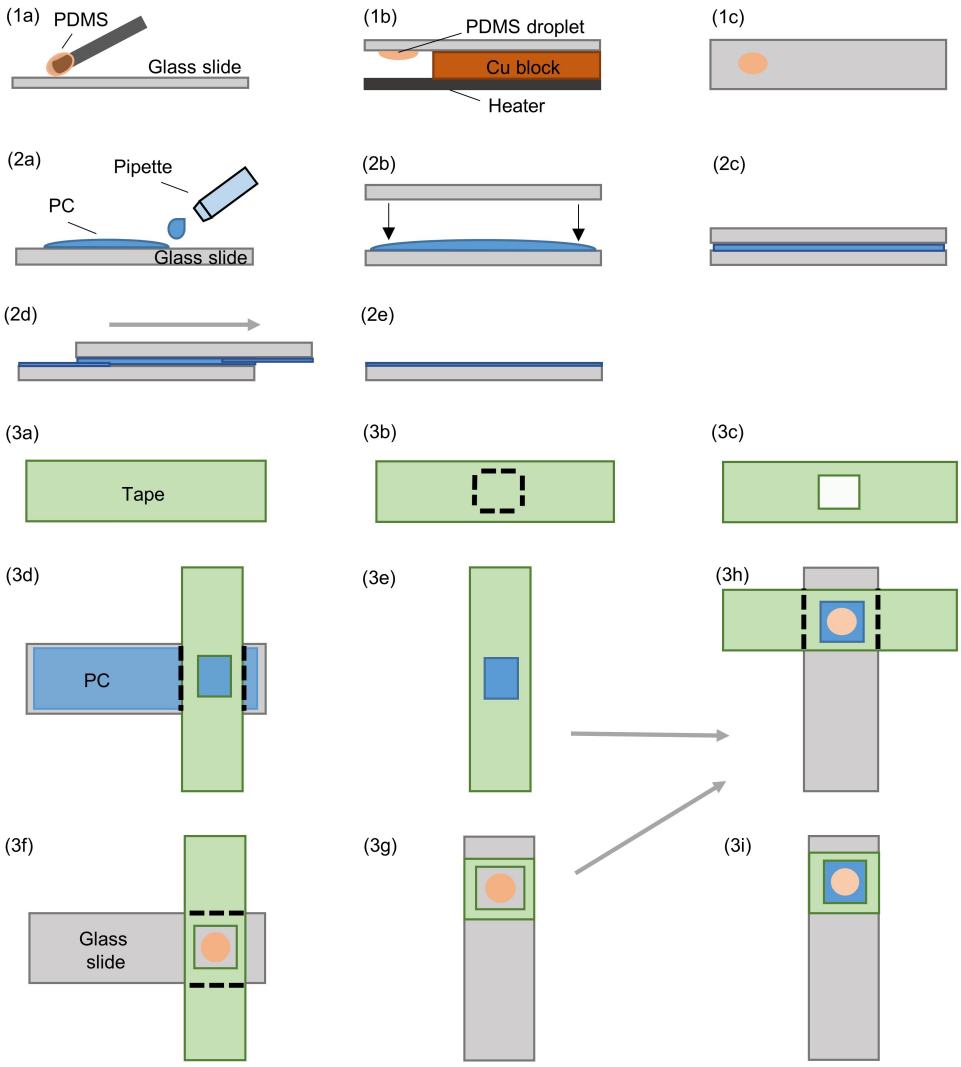

Figure 3.7: Stamp preparation for temperature-controlled viscoelastic stamping. (1) A glass slide is covered with liquid PDMS and dried upside-down over a hotplate to form domed shaped PDMS droplets. (2) PC film fabrication by flattening the polymer solution between two glass slides, where subsequent parallel removal leads to thin PC film covering both slides. (3) Stamp assembly. A tape with an aperture matching the droplet dimensions is used to peel off the PC film from the glass slide and then placed on top of the dome, previously prepared with double-sided tape around the PDMS to ensure adhesion. Figure adapted from Ref. [136]

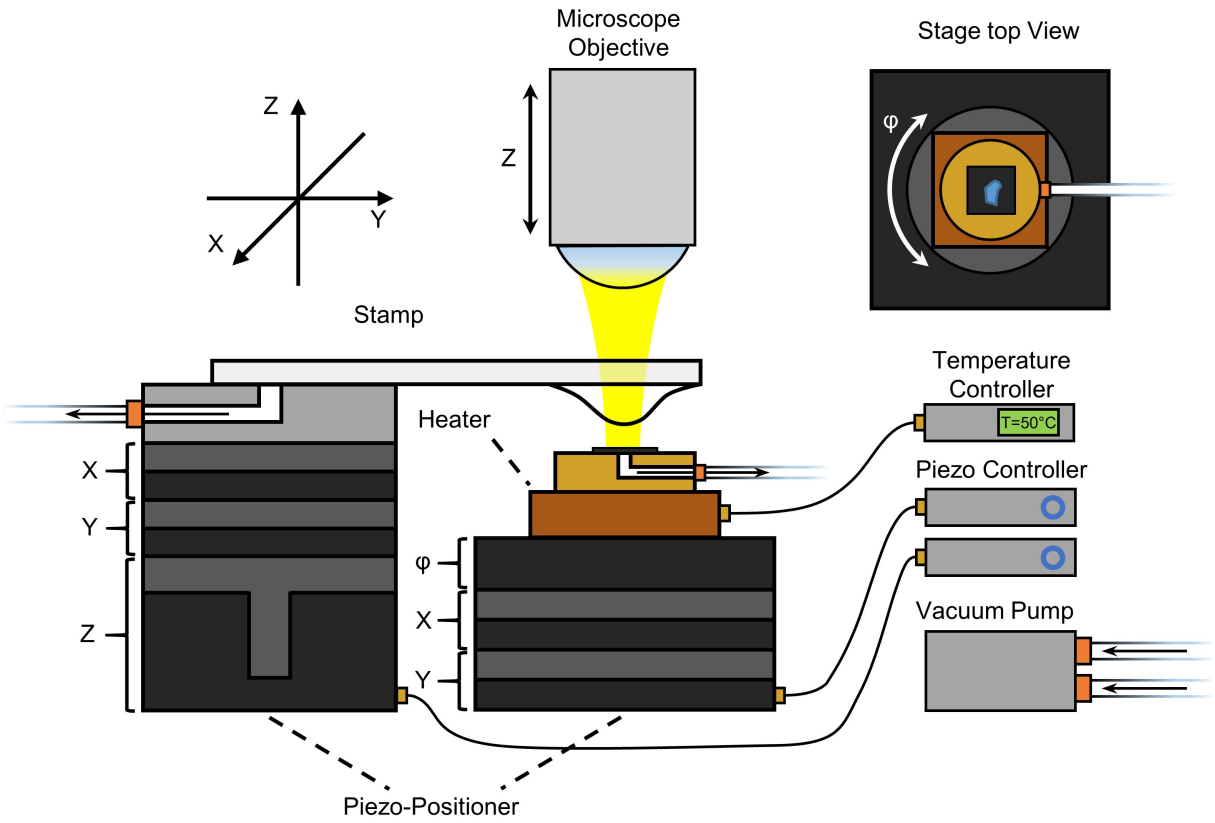

Figure 3.8: The Glovebox stamping-setup. Two piezo-stacks with lateral degrees of freedom in XY were placed underneath the z-motorised microscope equipped with long-working objectives ranging from 5x to 50x. Sample and stamp are fixed via vacuum suctions. In addition, the stamp has additional z-motorisation to allow precise control of the contact-interface. Rotational alignment is provided on the sample piezo-stack. A heater mounted underneath the copper sample-holder provides temperature control. Figure adapted from Ref. [137].

placed around the droplet to ensure adhesion of the PC-tape. Finally, the tapes are placed on top of each other, covering the PDMS with a thin PC film. Left over tape was removed afterwards (Fig 3.7.3)

Dry transfer

Before transfer and stacking of multiple materials on top of each other, the prepared stamp as described above was mounted inside the transfer setup as shown in Fig. 3.8 for careful optical examination. Care was taken to choose the best stamp without wrinkles, folds and possible contaminants, where roughly only 30% of the produced stamps showed a clean interface in a radius of ~500 μm. To test its elasticity, prior to the flake pick-up, the stamp was

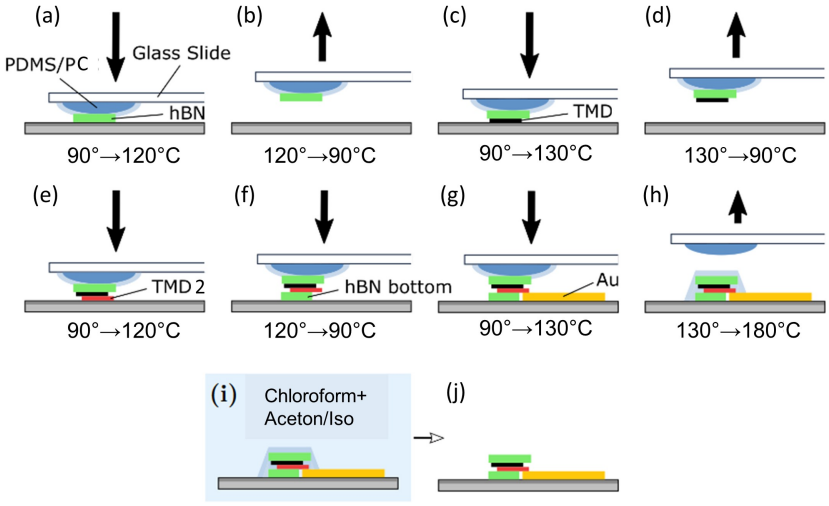

Figure 3.9: Schematic of the hot-pick-up technique with all stamping steps for vdW heterostructure assembly. (a) A glass slide covered with PDMS/PC is brought into contact with the top hBN at 90°C and picked up (b) from a SiO_2/Si substrate at 110-120°C. For TMD pick-up this processes is repeated at elevated temperatures of up to 130°C (c-f). The stack is then placed on the target substrate, schematically shown with a pre-patterned gold-structure, where the PC film was detached from the PDMS droplet and melt on the substrate at 160-180°C (g-h). Afterwards a chloroform bath over night and subsequent rinsing in acetone and isopropanol removes the PC residues from the stack (i-j). Figure adapted from Ref. [138].

brought into contact with a blank region on the SiO_2/Si substrate, heated up to 100°C and then subsequently lowered and lifted while monitoring the PC film. This test ensured that during the next stacking steps, each involving one repetition of extension and contraction, the PC film does not produce folds or breaks.

The full assembly of a heterostructure e.g. consisting of two TMD monolayer encapsulated in hBN and deposited on a predefined gold structure is shown in Fig. 3.9. In general, the tip of the dome is placed ~200-300 μm away from the desired flake and due to the transparency of the glass slide, PDMS and PC film, the surface of the target substrate is visible at all times. This allows precise lateral positioning as well as contact-control of the PC film with the SiO_2 substrate by varying the z-position of the stamp with up to ~nm step-size. It is crucial to slowly modify the contact-interface close and over the region of target flakes as strain and wrinkles have to be avoided. For that not only motion control, but also heat expansion is used, where typically interference stripes appear at the contact-interface which expand (contract) slowly with temperature increase (decrease). After full coverage of the desired flake with the stamp, waiting ~10 min for thermalisation increases the success rate. First a hBN flake is picked up with the PC-film, before acting itself as the adhesion interface for the subsequent 2D materials (TMD, few-layer graphite, hBN). After repetition of this process

until all desired TMDs are encapsulated in hBN, the stack is released from the stamp onto the target location by increasing the temperature above 160°C, such that the PC film starts to melt. Carefully lifting the stamp while maintaining high temperature dissolves the PDMS from the PC film and by careful lateral movements, the polymer film with the stack of 2D materials breaks off. Note, that the exact temperatures described above are just guides and vary strongly with the PC-solution concentration, thickness as well as stamping setup as the temperature sensors often do not reflect the real temperature at the sample. At last, the remaining PC film covering the desired structure is removed in a chloroform bath followed by rinsing in acetone and isopropanol. The stack was then slowly (1°C/min starting from 90°C) heated to 200°C for up to 12 h in an annealing oven at high vacuum of $\sim 10^{-9}$ hPa to extract enclosed atmosphere between the layers as well as evaporate water molecules, increasing the overall sample quality and homogeneity [131, 139], with the downside of possible stress-induced breaks.

3.2.5 Electrical contacts

In many electronic applications of TMDs, e.g. in field-effect transistors (FET) [140], it is crucial to control the doping inside the ML. But also for fundamental scientific questions, Fermi-level control enables the study of light-matter interaction for the negative, positive and neutral regime as most TMDs show intrinsic doping. In the most intuitive case, for that one needs to build a capacitor. Few-layer graphite hereby is compatible with the stacking recipe and enables the fabrication of dual-gate devices. In general, the need for low ohmic contact resistance [141] is crucial.

The samples investigated in this work however are based on the field effect device, where one contact is made with gold by directly placing the TMD stack on top and the other is the highly doped silicon of the substrate, acting as a global back-gate. To reduce the risk of device failure and damage, all fabrication steps described below were carried out prior to stack-deposition.

Standard lithography (Fig. 3.10 a) with a positive photo-resist (AZ 701 MIR), spin-coated at 3000 rpm for 40 s, was used for patterned gold-deposition on a blank SiO_2/Si layer. After pre-bake at 110°C for 90 s, the substrate was placed under a photo-mask in the Karl Suss MJB3 mask aligner. Exposure with a mercury lamp for 35 s was followed by submerging the substrate in developer (AZ 726 MIF) for 35 seconds and rinsing in water. Ultra-high vacuum electron beam evaporation was used to deposit Ti(5 nm)/Au(70 nm) and last, lift-off in an acetone bath removed the remaining photo-resist, leaving the defined gold-structure on the surface.

For the global backgate, the challenge is to avoid Schottky-barriers at low temperatures by creating an ohmic contact between the metal/semiconductor interface. Therefore, high-voltage boron-doped gold wires were electrically discharged through the doped silicon

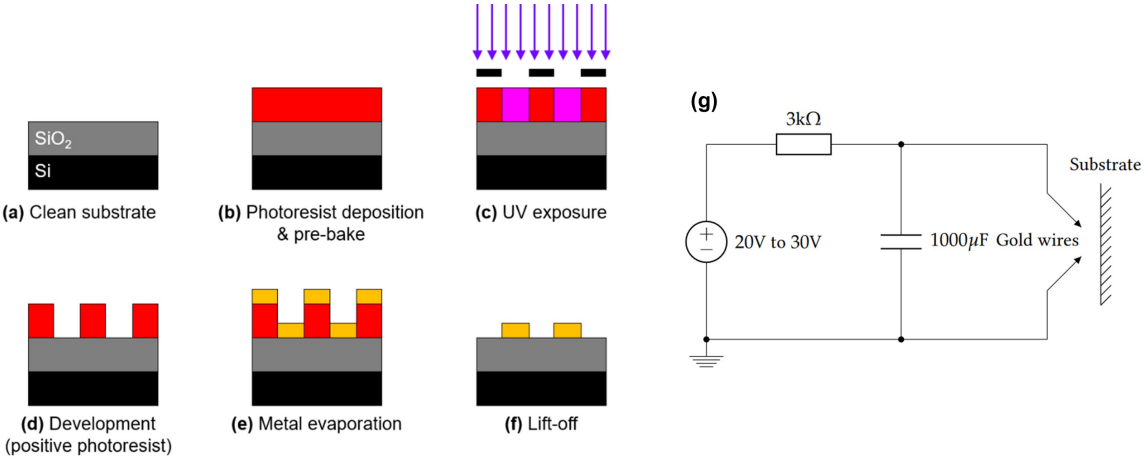

Figure 3.10: Schematic illustration of standard lithography (a-f): A clean substrate is spin-coated with positive photo-resist and pre-baked, before UV light exposure under a photo-mask and subsequent development removes the resist at exposed areas. Metal evaporation with a high vacuum electron beam then deposits Ti/Au on the surface before an acetone bath lifts off remaining photo-resist. (g) Circuit diagram for back-gate fabrication: A voltage source proving up to 30 V charges a capacitor, connected to two boron-doped gold wires. The distance between the wires and the silicon substrate is decreased until an electric arc discharges the capacitor thought the substrate, evaporating the tip of the wires and locally doping the silicon with a gradient semiconductor/metal-interface. Figures adapted from Ref. [91, 142].

substrate as its conductivity is higher than ambient air. A schematic is shown in Fig. 3.10 (b). As this process evaporates the tips of the wires, it creates a gradient metal-semiconductor and thereby avoids a Schottky barrier, leaving a gold droplet on the surface.

After successful stamping on the edge of the gold-structure, the capacity needed for electrostatic doping control is formed by the gold and silicon, separated by the bottom hBN and SiO_2 (50nm) layer. The gold-pattern as well as the gold-droplet on the substrate edge is now contacted with thin wires using conducting silver paste, giving a macroscopic access to voltage application. To assess the breakdown voltage and thereby determine the contact quality, a CV-measurement at cryogenic environments was conducted. As shown in Fig. 3.11, a lock-in amplifier monitors the real and imaginary part of the current created by an applied DC-voltage (±30 V) with a AC-modulation ($U_0 = 10$ mV, $f = 77$ Hz) between the contact and back-gate, giving access to the resistive and capacitive parts. By first performing the experiment with a gauge capacitance, the capacity of the sample is measured with high precision. To characterise the dielectric properties and device quality, the resistive part was monitored while increasing the DC voltage up to the point, where an exponential increase in the leakage-current was measured. Thereby, the voltage boundaries for safe device operations were determined.

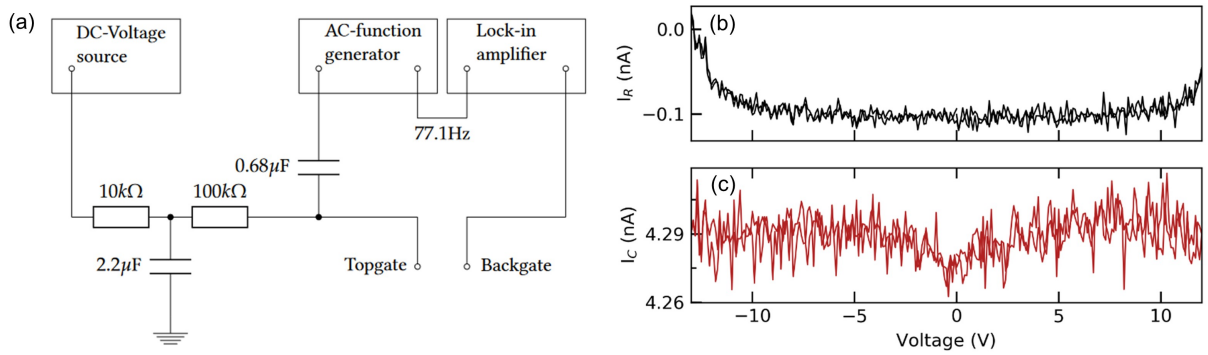

Figure 3.11: (a) CV-measurement setup. A lock-in amplifier measures resistive and capacitive currents between the sample top-gate and back-gate. Therefore, a constant AC-signal is added on a varying DC-voltage to measure small leaking currents. As the resistive part will rise close to the breakthrough voltage, the safe DC operation range for later studies is determined. (b-c) Exemplary measurement illustrating recorded resistive and capacitive currents as a function of DC voltage. An onset of the exponential rise in resistive current is visible above/below ±10V indicating the break down of the device. Figures adapted from Ref. [91, 138].

4 Spectral asymmetry of phonon sidebands in the photoluminescence of mono- and bilayer WSe_2

THIS CHAPTER IS BASED ON THE PUBLICATION [P2]
Funk, V., Wagner, K., Wietek, E., et al. Spectral asymmetry of phonon sideband luminescence in monolayer and bilayer WSe_2 Phys. Rev, Res. 3, L042019 (2021).

The following Chapter discusses an experimental study of temperature-dependent spectral line shapes of phonon sideband emission stemming from dark excitons in monolayer and bilayer WSe_2. Using photoluminescence spectroscopy in the range from 4 to 100 K, we observe a pronounced asymmetry in the phonon-assisted luminescence from momentum-indirect exciton reservoirs. We demonstrate that the corresponding spectral profiles are distinct from those of bright excitons with direct radiative decay pathways. The line-shape asymmetry reflects thermal distribution of exciton states with finite center-of-mass momenta, characteristic for phonon sideband emission. The extracted temperature of the exciton reservoirs is found to generally follow that of the crystal lattice, with deviations reflecting overheated populations. The latter are most pronounced in the bilayer case and at lowest temperatures. Our results add to the understanding of phonon-assisted recombination of momentum-dark excitons and, more generally, establish means to access the thermal distribution of finite-momentum excitons in atomically thin semiconductors with indirect band gaps.

4.1 Introduction

The nature of radiative electron-hole transition in semiconductor physics has a rich history. Germaniun (Ge) and silicon (Si) are two examples, where it became apparent that the fundamental optical response in absorption [143, 144] and emission [145–148] is determined by simultaneous energy and momentum conservation. Spectroscopy in general provides convenient methods such as PL, differential reflection (DR), transmission as well as time-resolved spectroscopy to discriminate between momentum-direct and momentum-indirect transitions. Ge/SiGe multiple quantum wells for example were studied extensively to identify interface transitions and phonon-assisted recombinations [149, 150] and enabled bandgap engineering for future device application.

As mentioned in Chapter 2, these learnings were successfully transferred to 2D semiconductors in general and TMDs in particular, where the prominent indirect-to-direct crossover from the bulk to the ML TMD was shown [10, 151]. Following recent advances in sample preparation and doping control [15, 16, 18, 19, 121], TMDs exhibit a rich spectrum of exciton PL associated with electron-hole pairs from different high-symmetry points of the first Brillouin zone.

In our studies, we employ temperature-dependent PL spectroscopy to analyse the spectral line shapes stemming from dark excitons in ML and BL WSe_2. The PL of charge-neutral mono and bilayer TMDs are generally grouped into features of excitons with zero center-of-mass momentum [10, 151–153] and phonon sidebands of dark excitons with finite momenta [P1, 22, 23, P4]. The former decay radiatively with in- or out-of-plane polarisation, where the characteristic spectral profiles in PL are symmetric and follow a Lorentzian or Gaussian distribution function. Contrary to that, the latter originate from higher-order processes that require the assistance of phonons to conserve momentum upon photon emission. In the specific case of WSe_2, phonon sidebands enrich the ML emission spectra by adding peaks energetically below the bright exciton [P1, 23, 24, P3, 122, 152–156].

In the following, the investigated charge-tunable WSe_2 ML and BL device will be characterised in PL as a function of doping. Afterwards, the study of temperature-dependent measurements on two devices results in a qualitative and quantitative line shape analysis for the charge-neutral regime, which gives access to the temperature-dependent peak energy, phonon-broadened linewidth and exciton temperature. Especially the resulting exciton temperature gives additional insight into exciton physics and together with the graphical approach of this work, offers a intuitive distinction between phonon-sidebands and direct transitions.

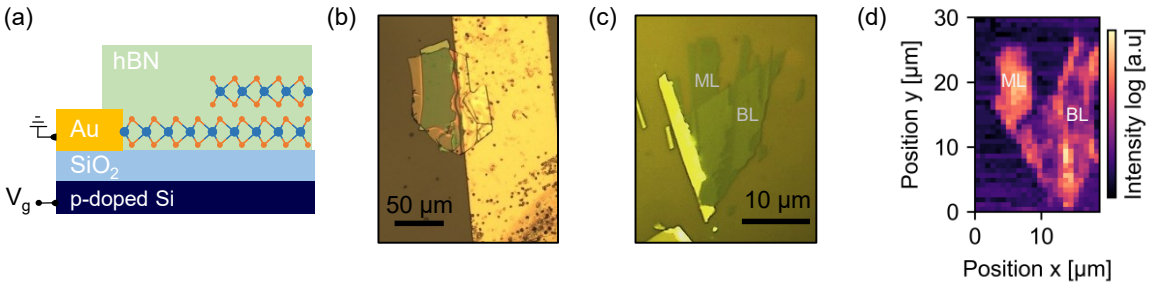

Figure 4.1: Characterisation of sample B: (a) Schematic of the studied hBN/WSe_2/hBN field-effect device. Figure taken from [P3].(b),(c) Optical microscope images of the heterostructure, where in (b) the full device including the gold-pattern created by standard lithography is shown. (c) Few-layer WSe_2 shown prior to stacking. (d) Low-temperature hyperspectral two-dimensional PL map, where investigated ML and BL regions are indicated.

4.2 Sample characterisation

The investigated samples A and B are based on exfoliated vdW heterostructures consisting of ML (samples A and B) and BL (sample B, see Fig. 4.1) WSe_2 provided by HQ Graphene, encapsulated between hexagonal boron nitride (hBN) layers and deposited on a SiO_2/Si substrate by viscoelastic stamping and subsequently annealed to enhance interlayer contact, as described in Chapter 3. Sample A was fabricated and measured with similar techniques by the Group of Prof. Alexey Chernikov, as noted in the affiliations of Ref. [P2]. In more detail, sample A was mounted in a continuous-flow cryostat in a confocal microscope and excited by a cw laser at 2.33 eV with a power of 500 nW into an optical spot of 1 μm diameter. The PL was dispersed with a spectrometer and detected by a charge-coupled-device camera.

In addition to the fabrication steps both samples have in common, sample B was transferred onto a gold electrode in contact with the TMD crystal (Fig. 4.1(b)) and in combination with a global back-gate, is functioning as a field-effect device which enables charge-density control of the WSe_2 ML and BL [P3], where the resulting device structure is displayed in Fig 4.1(a). Sample B was studied with a confocal microscope (see Chapter 3) in a closed-cycle magneto-cryostat with a base temperature of 3.2 K and excited with a cw diode laser at 1.95 eV close to the 2-s resonance of WSe_2 [157], with a low pump density in the linear regime. A hyper-spectral two-dimensional PL map of sample B under these experimental conditions is shown in Fig. 4.1 (d). Here, the integrated PL intensity is displayed in a logarithmic false-color plot, where bright regions are characteristic for ML PL and dark regions indicate the presence of a BL, where the labels specify the position of the further investigated confocal spots of ~ 1 μm. This assignment is confirmed by the image of a bright-field microscope of the few-layer WSe_2 crystal used in the device fabrication, displayed in Fig. 4.1 (c).

Fig. 4.2 shows the cryogenic PL for the accessible charge-doping control of sample B,

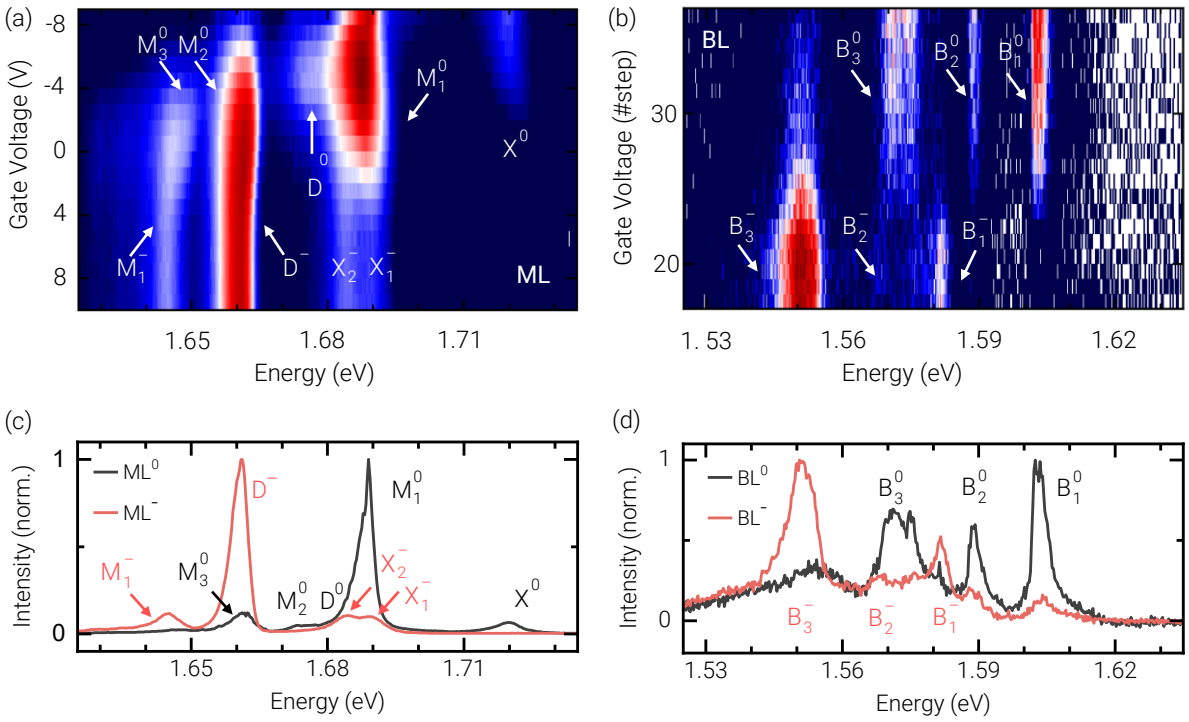

Figure 4.2: (a),(b) Logarithmic false-color plots of the photoluminescence as a function of the gate voltage, recorded at representative positions of monolayer and bilayer WSe2, respectively. The monolayer features characteristic photoluminescence of neutral bright (X^0) and dark (D^0) excitons, as well as the negatively charged bright trion doublet (X_1^- and X_2^-) and dark trion (D^-). All other peaks of monolayer (M) and bilayer (B) photoluminescence are labeled according to their charge state in the superscript and an increasing subscript number. (c),(d) Normalised PL spectra extracted from (a),(b) at the neutral (-8V) and charged regime (+8V) respectively, with same labels for clarification. For bilayer WSe_2 displayed in (d), marginal residual charges contribute to each spectrum.

where the voltage limit was tested with CV-measurements as described in Chap. 3. Logarithmic false color plots of the PL as a function of gate voltage are shown in Fig. 4.2 (a) and (b) for ML and BL WSe_2 respectively. In more detail, the spectra are recorded from a continuous dynamic modulation of the voltage between the determined limits in a zig-zag pattern. Therefore the y-axis differs between absolute voltage values for the ML and a selected range of the applied ramp with a relative scale for the BL spectra, where each step corresponds to − 1V. In the ML case shown in Fig. 4.2 (a) and (c), the charge-neutral regime (ML^0, peaks labeled according the superscript) is defined by the presence of X^0, the neutral exciton at 1.72 eV at -8 V, consistent with residual n-doping of the exfoliated crystal [18, 122]. The most prominent feature is the M_1 peak at 30 meV redshift from X^0. This peak has a rich history of controversial assignments, including defect-activated recombination of KK'

momentum-dark intervalley excitons [23, 24], phonon-assisted emission PL from virtual trions [158], and phonon sideband of momentum-dark KQ excitons [P1, P3].

The spin-dark KK exciton (D) in sample B is very weakly pronounced. With its 42 meV redshift from X^0 [64, 65, 152, 159], it lies on the red shoulder of M_1 and due to the chosen objective with an NA of 0.82, the in-plane collection of the PL is weak. A series of red-shifted peaks below are labeled by an increasing subscript number with decreasing peak energy as M_2 through M_4 and represent phonon sideband luminescence from long-lived dark excitons. In charge-neutral samples, recent work has ascribed the peaks M_2 and M_3 at 51 and 59 meV red-shifts from X^0 to phonon sidebands of momentum-dark KK' excitons [23, 24]. However, it has been also shown that excitons from KQ should exhibit phonon-assisted emission around M_2 [22, 27].

At positive gate voltages, the ML is charged with electrons and therefore shows the characteristic signatures of a bright trion doublet (X_1^- and X_2^-) with ~6 meV splitting caused by the exchange energy and an overall 29 and 36 meV redshift respectively from the neutral exciton X^0, caused by the additional binding energy of the trion [122]. The dark trion (D^-) at 28 meV redshift from X_1^- is the most prominent feature in the charged spectrum, followed by a series of low-energy peaks dominated by M_1^- at 44 meV redshift [23, 156].

Complementary to the ML results discussed above, Fig. 4.2(b) and (d) shows charge-tunable PL from encapsulated BL WSe_2. The neutral regime (indicated by superscript) features a multi-peak structure, labeled by an increasing subscript number with decreasing peak energy as B_1^0 through B_3^0. These peaks, located about 110 to 150 meV below the ML peak X, correspond to phonon sidebands of momentum-indirect KQ excitons [P3, P4, 160]. In the negative doping regime, a simultaneous redshift of 22 meV occurs for all peaks, leading to the assumption of a common origin of B_1^- through B_3^-, identified as bilayer KQ trions [P4] with the excess electrons accommodated at the conduction band edge by the Q-valleys. The imperfect charge-control leads to small features in Fig. 4.2 (d), where residual trion peaks are visible in the neutral regime, as well as vice versa, the lowest-energy peak B_3^- is weakly present in the neutral regime.

4.3 Temperature-dependent photoluminescence

Next, Sample A and B were investigated in temperature-dependent PL, where derivations from the cryogenic base temperature was achieved by applying a controlled voltage to resistances close to the sample (see Chapter 3). In Fig. 4.3, the resulting charge-neutral PL of both devices in the temperature range of 4 K to 120 K is shown. The fundamental PL response of Sample A hereby exhibits an overall sample-specific blue-shift of 8 meV, compared to the above discussed sample B. Due to the missing charge-tunability, a weak signature of the trion doublet is present in the recorded data presented in Fig. 4.3 (a). The overall reduced line-

width of all spectral features in sample A point to an additional phonon-sideband labeled as M_4. With its 65 meV red-shift from X, M_4 corresponds to the chiral-phonon replica of long lived spin-dark D excitons [23, 24, 156, 161], where D is specifically pronounced due to measurements with an high-NA objective.

All peaks show a characteristic temperature-dependent red-shift with increasing temperature, as previously shown for TMDs [154]. In general, early studies from Varshni [162] suggest, that the temperature-dependency of the semiconductor band-gap is described semi-empirically by $E_g = E_0 - \alpha T^2/(T+\beta)$, where E_g is the energy gap which may be direct or indirect, E_0 is its value at $0K$ and α and β are material specific constants. What is commonly referred to as bandgap renormalisation is a superposition of the temperature-dependent lattice dilatation and electron-lattice interaction. Later, a more advanced empirical formula was postulated by O'Donnell in Ref. [163], where the linear and quadratic behaviour of experimental data was captured and the problematic association of β with the Deybe-Temperature θ lifted. Here, the bandgap renormalisation is described by thermally activated phonons, with average phonon energy $\hbar\bar{\Omega}$. The dimensionless coupling constant S empirically describes the coupling to the lattice via:

$$E_0(T) = E_0^0 - S\hbar\bar{\Omega}\left[\coth\left(\frac{\hbar\bar{\Omega}}{2k_BT}\right) - 1\right], \tag{4.1}$$

where $E_0(T)$ is the temperature-dependent bandgap defined experimentally by the peak position, and E_0^0 the zero temperature limit of the peak energy. Modelling of the data with Eq. 4.1 is shown in Section 4.5.

In addition, the PL intensity of the bright exciton X increased with temperature at the expense of all lower-lying peaks. This is consistent with a temperature-dependent population redistribution from lower dark to energetically higher bright exciton states, in agreement with previous experimental studies [64, 159], where e.g. in Ref. [64] a simple two-level system with thermal Boltzmann distribution given as:

$$N_X(T) = \frac{exp(-\Delta/k_bT)}{exp(-\Delta/k_bT)+1} const \tag{4.2}$$

was used to identify a reservoir with an energy splitting of $\Delta = 30 \pm 5$ meV below X . $N_X(T)$ denotes the temperature dependent population X, T the temperature and k_B the Boltzmann constant. In the case of WSe_2, the spin-dark state D with its 42 meV red-shift appeared to be the best candidate in the mentioned reference. However, due to the uncertainty of this simplified model and the ambiguous energetic position of the Q-valley in WSe_2[P1], this simplification does not hold. A more recent theoretical study found in Ref. [22] investigates the lower lying phonon-sidebands in ML WSe_2 and attributes it to KK' excitons, mediated by acoustical and optical phonons, where M_1^0 was left out of discussion due to the above

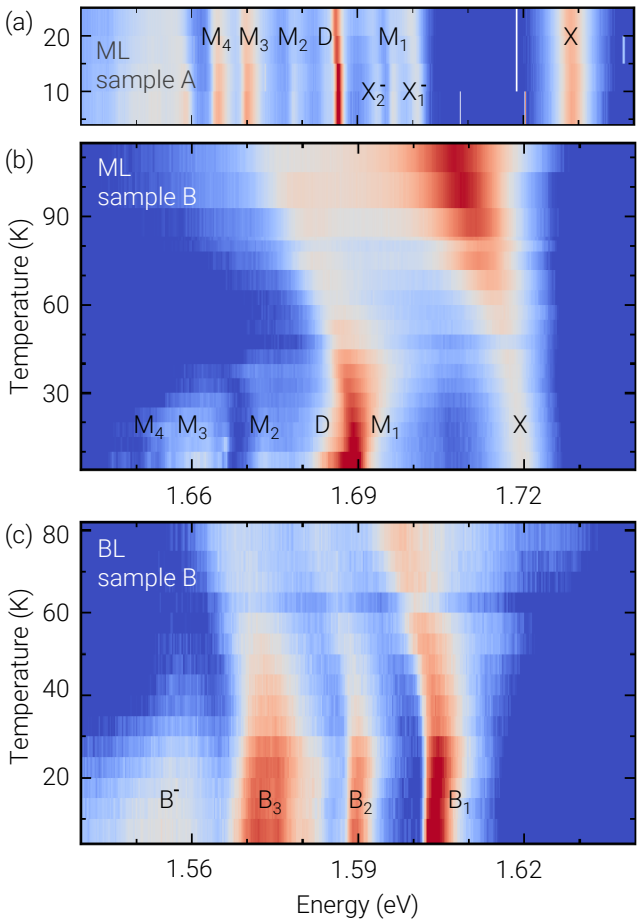

Figure 4.3: (a), (b) Logarithmic false-color plots of the PL from samples A and B of ML WSe_2 encapsulated in hBN. The former exhibits features of residual doping and the latter is tuned to charge neutrality and therefore, no superscript was used for the neutral regime. (c) PL of BL WSe_2 from sample B tuned close to charge neutrality with a marginal contribution of the negative bilayer trion B^-. The spin-bright and spin-dark KK exciton peaks are denoted as X and D, and the trion doublet as X_1^- and X_2^-. The remaining ML and BL peaks are labeled by an increasing subscript number n as M_n and B_n, respectively.

mentioned ambiguity. The fundamental intensity increase of X though, was fully captured in the description.

For the BL case, the temperature-induced energy shifts in PL are similar to the ML. The evolution of the PL intensity with increasing temperature although differs significantly. The indirect bandgap of the BL is substantially smaller than the energy of the direct KK transition and therefore, the thermal energy on the order of 10 meV accessed in our experiments is far from sufficient to provide substantial thermal excitation of the population from the momentum-dark KQ reservoir into bright KK states with efficient radiative decay pathways. Consequently, the relative intensities of all peaks remain largely the same with a moderate decrease of the total emission signal. Only B^- quenches strongly, as expected for a weakly bound trion state.

4.4 Line-shape analysis of the photoluminescence of mono and bilayer WSe_2

Following the description of the relevant transitions with its temperature dependent bandgap renormalisation and population distribution, we now focus on their characteristic spectral lineshapes. The left panels of Fig. 4.4 (a) and (b) shows the recorded normalised spectra at different temperatures, shifted to the energy of X and B_1 for ML and BL, respectively. The temperature range hereby is 4 to 120 K (a) and 4 to 80 K (b), encoded in the color from purple to red. The direct comparison between ML and BL highlights the main difference in their temperature dependent spectral profiles. Whereas the ML bright exciton peak X is well described by a symmetric peak function such as a Lorentzian which broadens symmetrically with temperature, the BL peaks even at low temperatures are asymmetric with a pronounced high-energy shoulder which becomes increasingly prominent at higher temperature. The symmetric spectral broadening shown for X is well described by phonon mediated dephasing. The temperature-dependent exciton linewidth $\Gamma(T)$ is hereby the full-width at half-maximum (FWHM) Lorentzian linewidth in units of energy. It follows the quantitative assessment which relates the spectral broadening to the phonon occupation weighted by their interaction strength with electron-hole pairs given by [164]:

$$\Gamma(T) = \Gamma_0 - a\,T + b\left[\exp\left(\frac{\hbar\Omega}{kT}\right) - 1\right]^{-1}. \tag{4.3}$$

Here Γ_0 represents the zero temperature limit (excluding inhomogeneity), and a and b denote the coupling constants for linear-acoustic and fixed-energy phonons, respectively. The latter generally includes both optical and high-momentum acoustic modes in TMD materials [154, 165–167]. The energy of the dominant phonon in the last term is responsible for a super-linear linewidth dependence on the temperature, denoted by $\hbar\Omega$.

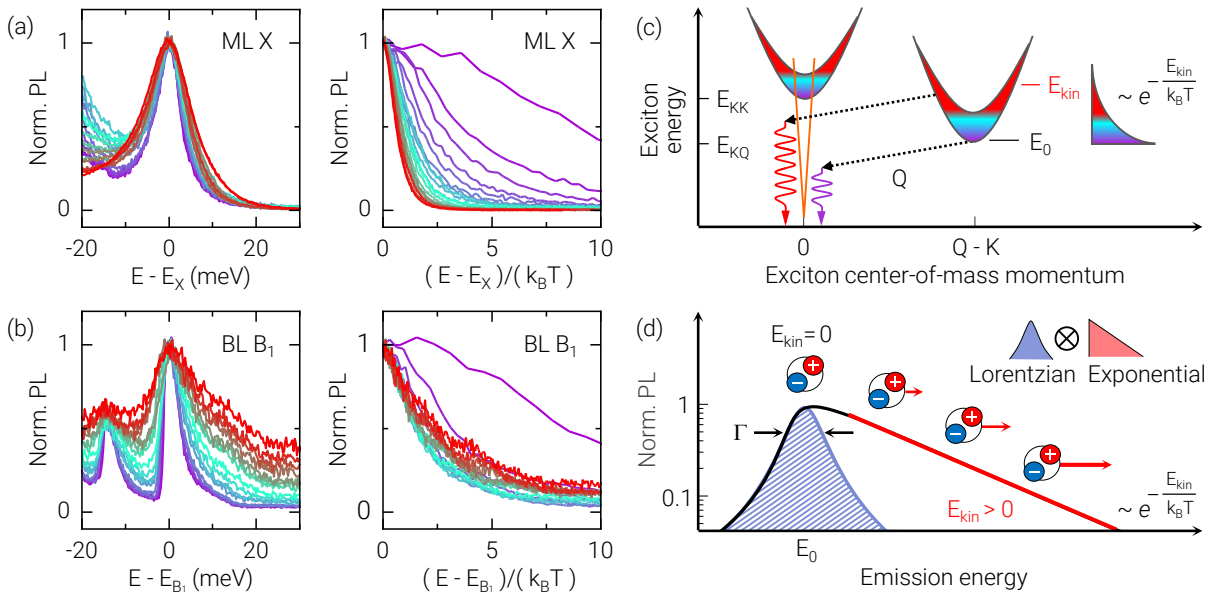

Figure 4.4: (a) Left panel: ML PL spectra from sample B at temperatures from 4 to 120 K, colored from purple to red, normalised to unity and shifted horizontally to the energy E_X of the bright exciton peak X at 4 K. Right panel: Same spectra shifted to the peak center with displayed high-energy shoulder for a rescaled energy axis by $k_B T$. (b) Same for BL in the temperature range from 4 to 80 K with the energy of the peak B_1 as reference. (c) Schematic representation of direct and indirect exciton decay processes. KK excitons, such as X or D, with zero-phonon radiative decay are restricted to 'cold' excitons, indicated by blue shaded population inside the orange light cone. In contrast, phonon sideband luminescence of momentum-dark excitons such as KQ with energy minimum $E_0 = E_{KQ}$ and exciton center-of-mass momentum $Q - K$ is assisted by phonons with momentum Q. This also includes emission from 'hot' excitons, thermally activated population indicated by the red shaded region of the quadratic band). The thermal Boltzmann occupancy of exciton states with finite kinetic energy $E_{\mathrm{kin}} > E_0$ above their respective dispersion minimum is represented by the area of colored shades. (d) Illustration of the phonon sideband asymmetry: The homogeneously broadened Lorentzian spectrum with linewidth Γ is displayed by the blue shaded region, where the y-axis is logarithmic. To model the high-energy shoulder of the observed spectrum, the Lorentzian is convoluted on the high-energy side with the contribution from excitons with finite kinetic energy $E_{\mathrm{kin}} > 0$ according to their exponential Boltzmann thermal occupancy.

On the other hand, the scenario of linewidth broadening due to exciton-phonon scattering applicable to X [154, 165] is insufficient to explain both the presence and the temperature-dependent increase of the higher-energy shoulder of BL peaks.

Generally, an arbitrary crystal momentum is transferred to a phonon. The direct radiative decay pathway of X, also known as zero-phonon line, is limited by recombinations inside the radiative cone, defined by $q_{phot} = \omega/c$. Therefore the condition $k(\omega) \leqq q_{phot}$ has to be fulfilled for photon emission. Thermally excited excitons thus do not directly contribute to the spectra without energetic relaxation via acoustic phonon scattering following the quadratic dispersion $E_X = \hbar^2 k^2/(2M)$, with M being the effective exciton mass and k its momentum.

Recombination of momentum-indirect excitons on the other hand require both a photon and a phonon to simultaneously satisfy energy and momentum conservation constraints. Excitons with a finite center-of-mass momenta recombine via phonon-assisted pathways by momentum transfer such that the resulting exciton momentum is inside the radiative cone. Therefore, all states of the thermally occupied indirect valley are accessible. In consequence, the thermal distribution of exciton momenta directly manifests in the characteristic high-energy shoulder of the resulting PL spectra as illustrated in Fig. 4.4(c) and (d). This very fundamental issue was observed earlier on conventional semiconductors [168–170] and is used in this work to differ between direct transitions and phonon-assisted processes in WSe_2.

This difference becomes even more apparent by rescaling the energy axis at each temperature by the thermal energy of the lattice $k_B T$, with the high-energy shoulder shown in the right panels of Fig. 4.4 (a) and (b). In this representation, the PL spectra of X are all distinct due to symmetric thermal broadening. On the contrary, the BL spectra collapse onto a universal curve for all temperatures above 10 K, when the thermally activated high-energy flank dominates over symmetric broadening. This graphical approach provides a simple method to determine the origin of the peak broadening.

4.5 Modeling of phonon sidebands

To analyse these observations quantitatively, we model the phonon sidebands by Lorentzians weighted with the thermal occupation of exciton states with finite kinetic energies $E_{\text{kin}} = E - E_0 > 0$, as illustrated in Fig. 4.4 (d). This approach yields the spectral lineshape $I(E)$ of phonon sideband resonances at temperature T as:

$$I(E) = I_0 \int_0^\infty \frac{\Gamma/2}{(E-E_0)^2 + (\Gamma/2)^2} \exp\left(-\frac{E_{\text{kin}}}{k_B T}\right) dE, \tag{4.4}$$

where I_0 is a normalisation constant, Γ is the full-width at half-maximum (FWHM) Lorentzian linewidth in units of energy, and k_B is the Boltzmann constant. The exponential term in

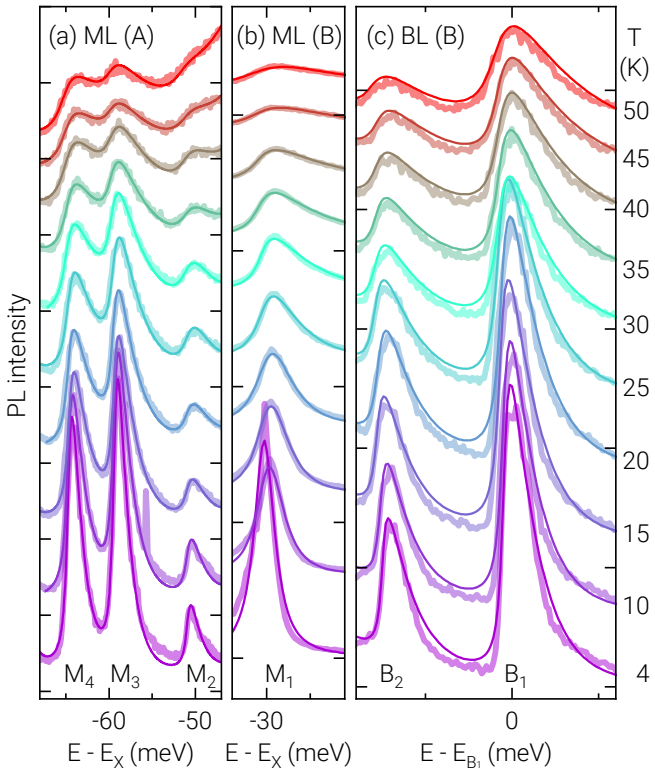

Figure 4.5: Model fits of the asymmetric peaks in (a) and (b) for ML of sample A and B, respectively, and (c) BL of sample B. The fits are displayed in solid lines and were obtained according to Eq. 4.4 to the spectra for temperatures ranging from 4 to 50 K, with exciton temperature, Lorentzian linewidth, peak energy and intensity as free fit parameters. The pronounced asymmetry on the high-energy side of all ML and BL peaks is clearly visible and in good agreement with the model of contributions from thermally activated excitons with finite center-of-mass momenta.

the integral corresponds to the Boltzmann occupation of exciton states with kinetic energy measured with respect to the corresponding exciton band minimum at E_0, for example $E_0 = E_{KQ}$, as displayed in Fig. 4.4 (c). Eq. 4.4 is equivalent to the result of a rigorous derivation in Ref. [22] and was used to model the experimental spectra at different temperatures using I_0, E_0, Γ and the effective exciton temperature $T = T_{\text{exc}}$ as fit parameters. The Boltzmann approximation for bosonic exciton quasiparticles should be reasonable due to rather low population densities in our experiments, see Section 4.2.

The results of least square numerical fits to the spectra of selected ML and BL peaks from both samples are shown as solid lines in Fig. 4.5 (a)-(c). The ML and BL spectra were shifted at each temperature to the energy of the X and B_1 peaks, respectively. To focus on the asymmetric lineshape, the spectra was normalised and offset for clarity. The overall good fit quality over the studied temperature range shows that the peaks M_2, M_3 and M_4 in Fig. 4.5 (a)

as well as M_1 in Fig. 4.5 (b) and B_1 and B_2 in Fig. 4.5 (c) are all asymmetrically broadened and adequately modeled by Eq. 4.4. In particular, it demonstrates the necessity to convolute a thermally broadened Lorentzian with a high-energy shoulder of thermal exciton occupation defined by the 2D Maxwell-Boltzmann factor, to account for the experimental observations.

We first confirm that the lattice temperature corresponds to the externally controlled temperature. To this end, the energy E_0 obtained from best fits to the peaks X, B_1 and B_2 in sample B is plotted as dots in Fig. 4.6 (a) as a function of temperature. The evolution shows for all peaks the expected red-shift with increasing temperature and substantial contributions from bandgap renormalisation by thermally activated phonons, modelled with Eq. 4.1 and displayed with solid lines. The zero temperature limit of the peak energy E_0^0 was left as a free fit parameter. The values for the coupling constant S (2.06 and 1.75 in ML and BL) and the average phonon energy $\hbar\bar{\Omega} = 15$ meV were taken from Ref. [154], due to the higher numerical stability from the wide temperature range used. The observed shifts in our samples are in quantitative agreement with the used parameters and therefore, our analysis strongly supports a one-to-one correspondence between the experimental temperature and the temperature of the crystal lattice. This is a crucial requirement for further interpretation.

The homogeneous linewidth broadening Γ obtained from best unconstrained fit is shown as the red solid line in Fig. 4.6 (b), with the resulting parameters: $\Gamma_0 = 0.9 \pm 0.2$ meV, $a = 25 \pm 10$ μeV/K, $b = 32 \pm 17$ meV and $\hbar\Omega = 15$ meV . Especially $\hbar\Omega$ gives additional insight in the involved phonon modes. A constrained fit with the energy of the LO phonon 31.25 meV yields a rather poor match to the data. The extracted characteristic phonon energy is consistent with 16.3 meV, determined from coherent nonlinear spectroscopy for ML WSe_2 [166] and close to the zone-edge phonon energy of 20 meV in related studies of WS_2 [165]. The coupling constant a obtained from the above analysis is within the range of previously reported values of $20 - 60$ μeV/K for WSe_2 MLs [17, 25, 171].

The last fit parameter is the effective exciton temperature T_{exc}, plotted against the nominal experimental temperature in Fig. 4.6 (c). From the fit procedure defined by Eq. 4.4, we find that the extracted exciton temperature generally follows that of the lattice. For ML peaks in particular, this agreement is very close as illustrated by the gray solid line in Fig. 4.6 (c) which represents the lattice temperature, confirmed above. In contrast, the momentum-indirect excitons in the BL are overheated by about 20 K with respect to the lattice temperature.

This observation will be discussed in the following. At low temperatures, the small derivation from the crystal lattice for the ML phonon-sidebands (M_2, M_3, M_4) stems from the lifted energy and momentum constrains due to phonon-assisted recombination. The increase of this effect in the BL case is attributed to the timescales of the exciton lifetimes in the studied samples. In the ML case, the phonon sidebands M_2, M_3 and M_4 stem from dark excitons that decay on the order of several 100's of ps. Consequently, they live sufficiently long, such that the initially hot excitons are lowered in energy by phonon-scattering on a timescale of a few 10's of ps [27]. Similar arguments apply to the peak M_1. From our analysis, the momentum-

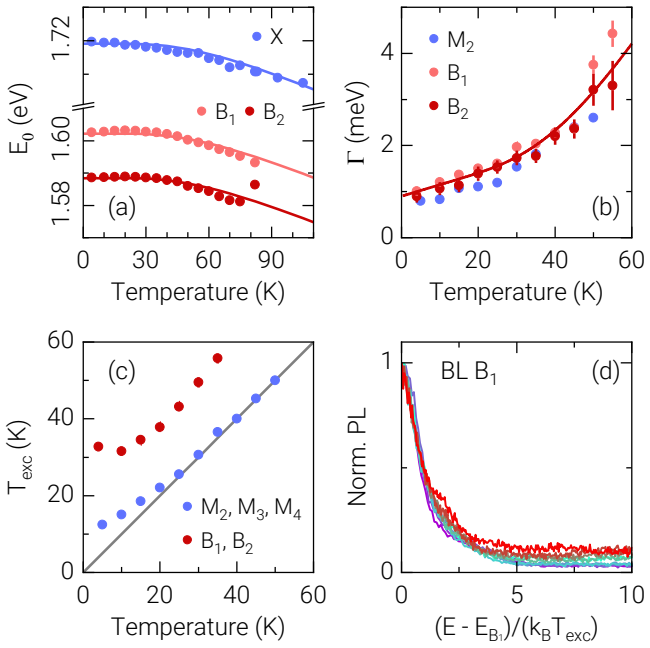

Figure 4.6: Parameters obtained from least-square model fits after Eq. 4.4. (a) Peak energy evolution with temperature for X in ML and B_1 and B_2 in BL of sample B. The solid lines show best fits to thermal bandgap renormalisation according to Eq. 4.1, where parameters from Ref. [154] were used and the overall good fit quality confirms the lattice temperature to match the experimentally measured temperature. (b) Lorentzian symmetrical linewidth of the ML peak M_2 in sample A, and BL peaks (B_1 and B_2) in sample B. The solid line represents the resulting best fit for BL peaks taking into account thermal phonon broadening according to Eq. 4.3. (c) Extracted effective exciton temperature T_{exc} from best fit, plotted versus the nominal sample temperature, shown by the solid grey line. (d) Blue shoulder of B_1 with energy axis normalised by the effective exciton temperature $k_B T_{\mathrm{exc}}$.

indirect character is confirmed, although with its ambiguous discrimination by the exciton g-factor [23, 24, P3], its origin is still unclear. The direct decay of momentum-indirect KK' excitons [23, 24] as well as a phonon sideband of the KQ reservoir [P1] are still under debate.

In contrast, the lifetime of the lowest-energy KQ exciton reservoir in BL WSe_2, with phonon sidebands B_1 through B_3, is only 25 ps [172]. This difference of at least one order of magnitude in the momentum-dark exciton lifetimes between ML and BL, paired with a higher relative injection energy for the latter, accounts for overheating of momentum-dark KQ excitons in the BL case. This is also reflected by the departure from one universal spectrum, shown in the right panel of Fig. 4.4(b). By rescaling the blue shoulder of B_1 by $k_B T_{\mathrm{exc}}$ as in Fig. 4.6(d), the expected notion for phonon-sidebands is recovered. This confirms the thermal Boltzmann occupation of exciton states according to their kinetic energy and temperature.

4.6 Conclusion

In conclusion, the PL of ML and BL WSe_2 was experimentally studied and characteristic spectral lineshape asymmetry of phonon sidebands identified. In contrast to symmetric PL peaks from zero-momentum excitons, the asymmetric profiles arise from thermal distribution of excitons in long-lived dark reservoirs with finite center-of-mass momenta. The extracted exciton temperature generally follow that of the crystal lattice. However, deviations indicate the presence of overheated exciton populations in the system. These are mostly pronounced at lowest temperatures and in the BL case, when the recombination lifetime approaches the time-scale of the cooling processes. Such direct experimental access to the temperature of excitons with finite center-of-mass momenta provides additional insight into the fundamental electron-hole recombination processes in atomically thin semiconductors. Therefore, our work emphasises the distinctions of momentum-direct and momentum-indirect recombination pathways for the entire class of TMD semiconductors and heterostructures. This analysis demonstrates spectroscopic means of distinguishing the respective exciton reservoirs and highlights the role of the phonon-assisted emission for long-lived excitons.

5 Dynamics of spin-valley polarisation of interlayer excitons

In the following Chapter, we will describe the time-dependent change in the polarisation of the exciton emission from a WSe_2-$MoSe_2$ HBL in H-type configuration. First, we introduce the sample properties and confirm the dominant atomic registry of H_h^h via PL energy and exciton g-factor measurements. Fundamental considerations regarding the physical origin of the degree of circular polarisation are given, followed by the description of a rate equation model to capture the magnetic field dependent time-resolved and steady-state PL data. The interplay of long-range Coulomb exchange interaction described by a Hanle-like spin-dephasing, as well as thermal population distribution between Zeeman-split reservoirs of the momentum-direct and momentum-indirect triplet states determines the valley polarisation. This analysis provides access to the intrinsic spin lifetimes of long-lived spin-like momentum-direct and momentum-indirect interlayer excitons.

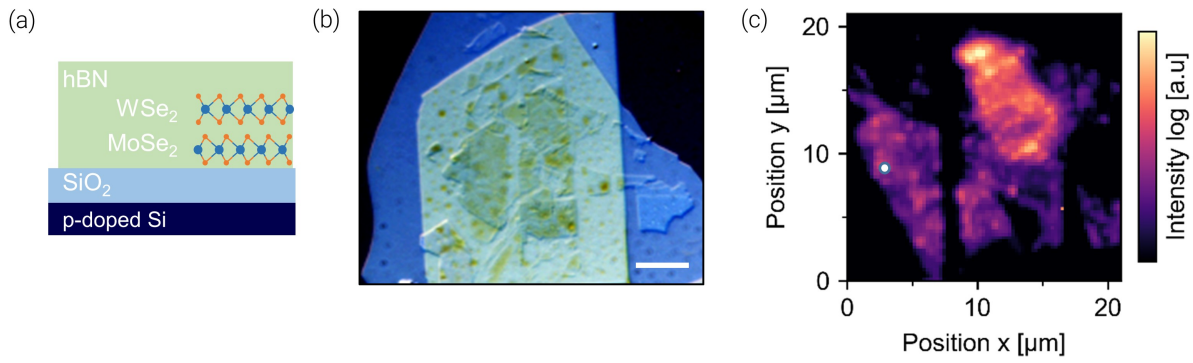

Figure 5.1: Characterisation of the investigated WSe_2-$MoSe_2$ HBL. (a) Schematic of the sample, consisting of an hBN encapsulated WSe_2-$MoSe_2$ HBL in R- and in H-type stacking on a SiO_2/Si substrate. (b) Bright-field microscope image. Scale bar (white) corresponds to 10 μm. (c) PL hyperspectral image recorded at 3.5 K under linear excitation at the $MoSe_2$ ML 1s exciton resonance corresponding to 1.642 eV. The white dot indicates the spatial position of interest.

5.1 Sample characterisation

The investigated sample consist of a WSe_2-$MoSe_2$ HBL encapsulated in hBN on a SiO_2/Si substrate. During its fabrication, a PDMS stamp without an additional PC film was used to transfer each individual 2D crystal consecutively. In the case of $MoSe_2$, two separate stamping steps were performed with a 180° twist angle to obtain both R- and H-type stacking in one sample, where the crystal axes of the MLs were aligned to ensure near parallel and antiparallel orientations. A schematic of the structure is shown in Fig. 5.1 (a). Figure 5.1 (b) shows a bright-field microscope image. Further characterisation was carried out by PL measurements under cryogenic conditions at 4 K (Atto-Dry 1000, Attocube). A hyperspectral PL map under 3 μW excitation at 1.642 eV was recorded in the energy range of interlayer exciton (IX) emission [173], with an integrated PL intensity from 1.26 - 1.53 eV (Fig. 5.1 c). The color-code from dark to bright is displayed on a logarithmic scale. The bright regions recorded in the energy range of IX correspond to R-type stacking and the darker regions to H-type stacking [33, 174], where the dominant atomic registry defines the optical response.

The lack of homogeneity in brightness in either stacking region indicates two likely effects. First, the the fabrication technique is prone to the formation of local strain, trapped pockets of ambient air and organic residues which all contribute to sample disorder. Second, mesoscopic reconstruction (see Chapter 2.2.2) as a consequence of strain relaxation and adhesion energy minimisation leads to single atomic registries exceeding the size of the moiré unit-cell by orders of magnitude, comparable to the optical spot-size of ~ 1 μm of the confocal microscope [33, 175, 176]. Therefore, the spectral response is highly position dependent. The following measurements focus on a local region near the edge of the HBL

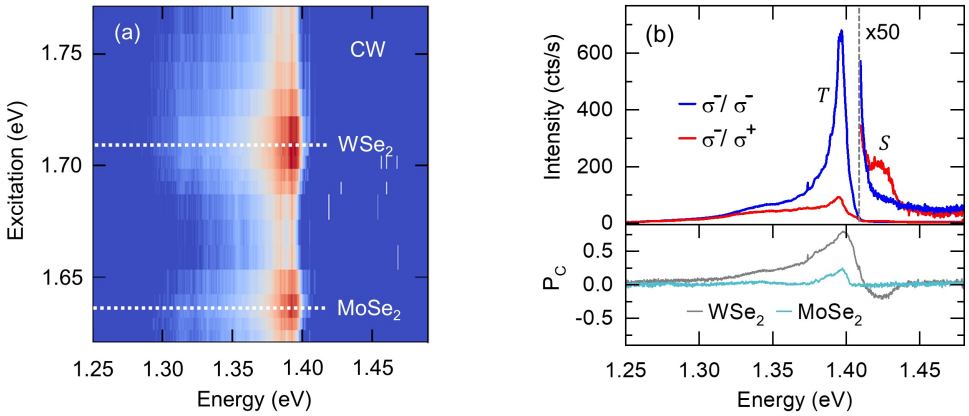

Figure 5.2: Cryogenic confocal photoluminescence measurements on the H_h^h-type WSe_2-$MoSe_2$ HBL. (a) Logarithmic false-color plot of the PLE response from the H-type heterostructure region at continuous-wave excitation with 3 μW. White dotted lines indicate the intralayer exciton resonances. (b) upper pannel: PL spectra under σ^- circular polarised illumination at 1.707 eV excitation energy with a power of 100 μW. The spectra were recorded under co (σ^-) and cross (σ^+) polarised detection, where the intensity for energies higher than 1.405 eV was magnified for clarity. The two features at 1.395 and 1.420 eV are attributed to the Triplet (T) and singlet (S) interlayer excitons of the H_h^h-stacking. Lower panel: Degree of circular polarisation recorded at resonant excitation at the intralayer resonances.

indicated with a white dot in Fig. 5.1(c).

First, photoluminescence excitation (PLE) was carried out to identify exciton resonances, shown in Fig. 5.2 (a). Here, a narrow-band (~ 50 kHz) continuous-wave (cw) laser (SolsTiS, M-squared) was tuned between 1.62 and 1.77 eV and the interlayer exciton PL was recorded under circular co-polarisation (σ^-/σ^-) in the range from 1.25 to 1.5 eV. Two distinct features, at 1.631 and 1.707 eV are associated with the 1s exciton resonance of $MoSe_2$ and WSe_2 ML, respectively [157, 177]. The interlayer exciton formation in a ype-II band-alignment is mediated by charge-transfer processes between the layers and therefore dependent on the population of excited intralayer excitons [81, 173]. Fig. 5.2 (b) shows the according PL spectra, where the laser was tuned to the WSe_2 1s resonance at 1.707 eV and used for circularly polarised excitation at 100 μW. Here, the two spectral features at 1.395 and 1.420 eV are attributed to the triplet (T) and singlet (S) interlayer excitons of the H_h^h-stacking due to their energetic position close to the theoretical and experimental values [33, 178]. The low-energy spectral shoulder may stem from weak unintentional intrinsic doping leading to residual interlayer trion formation of the triplet state [179], or defect-mediated localisation of excitons.

The most important feature of the PL emission of this study is the degree of circular polarisation of the exciton emission. We denote $I_{\sigma_1}(\sigma_2, B_z)$ for the intensity recorded under detection σ_1 in either σ^+ or σ^- circular polarisation with excitation σ_2 (again, either σ^+ or

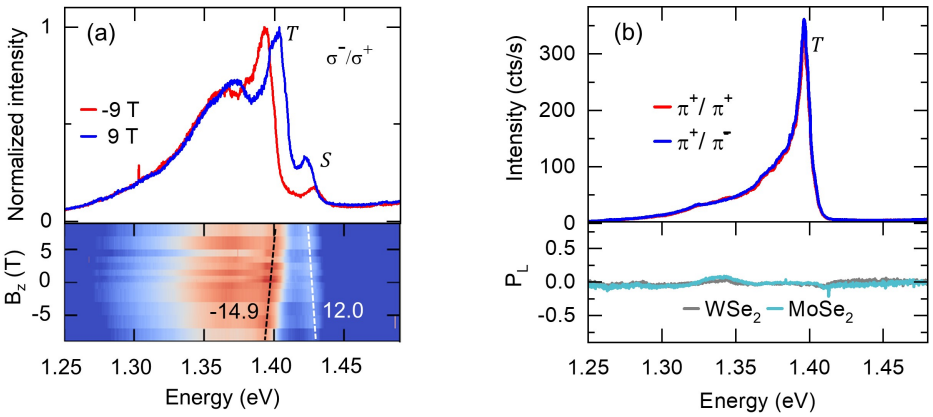

Figure 5.3: (a) Magneto-luminescence spectra recorded under cw excitation with a power of 100 μW under σ^--polarised excitation and σ^+ detection at −9 and 9 T. Lower panel: Magnetic PL sweep from −9 to 9 T with linear least-square fits to the peak positions of T and S, with resulting g-factor values of $g(T) = -14.9$ and $g(S) = 12.0$. (b) PL spectra under linear cw excitation at 1.707 eV and 100 μW with co- and cross linear detection basis. Lower panel: Degree of linear polarisation for excitation at both intralayer exciton resonances.

σ^-) in the magnetic field B_z perpendicular to the sample. The degree of circular polarisation, denoted as $P_c(\sigma_2, B_z)$ in the basis of excitation is then given by:

$$P_c(\sigma_1, \sigma_2, B_z) = \frac{I_{\sigma_1}(\sigma_2, B_z) - I_{-\sigma_1}(\sigma_2, B_z)}{I_{\sigma_1}(\sigma_2, B_z) + I_{-\sigma_1}(\sigma_2, B_z)}, \tag{5.1}$$

where the minus sign in the subscript ($-\sigma$) reverses the polarisation between σ^+ and σ^-. As shown in the lower panel in Fig. 5.2 (b), in contrast to the positive values of P_c for the dominant peak T, for energies higher than 1.41 eV we observe a negative value for P_c. This is attributed to the energetically higher singlet state S, which is populated due to the high excitation power and emits hot PL. According to previously discussed optical selection rules (see Chapter 2.2.5), this change in sign of the observed P_c confirms our peak assignment. Interestingly, the absolute value of polarisation decreases dramatically, when the excitation energy was set to the $MoSe_2$ 1s intralayer exciton resonance, which indicates a transfer of the intralayer exciton polarisation, linked to the energetic ordering of bright and dark states and their difference in intervalley scattering mediated by exchange interaction [180].

To confirm our peak assignment, additional magneto-luminescence and polarisation-resolved spectroscopy was carried out (Fig. 5.3). First, PL spectra under circular excitation and cross-polarised detection as a function of magnetic field were recorded. The magnetic field removes the valley degeneracy and splits the exciton reservoirs by the characteristic Zeeman shift proportional to the exciton g-factors (see Chapter 2.2.4). The comparison between the spectra recorded at 9 and −9 T indicates a negative g-factor for T, and a positive g-factor for S, which is confirmed by a full magnetic sweep and linear least-square fits to the

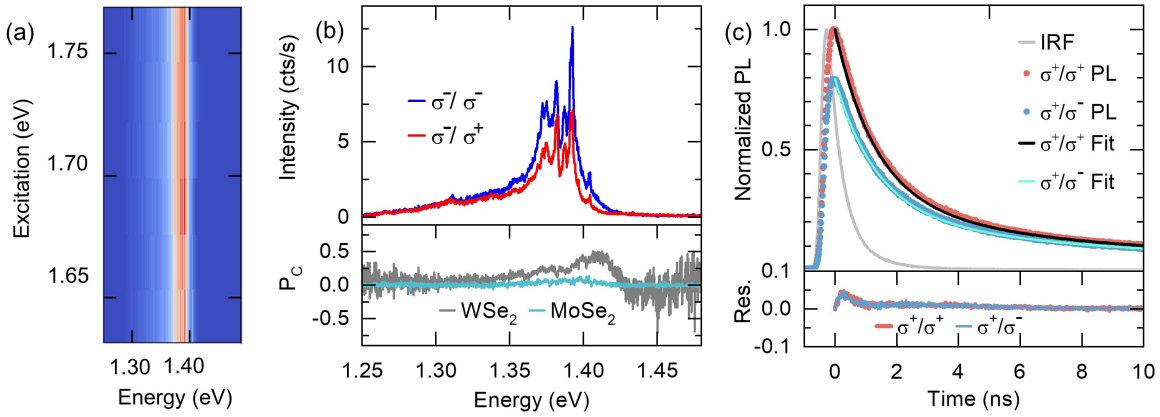

Figure 5.4: (a) Linear false-color plot of PLE from the H_h^h-type HBL region for a pulsed excitation at 2 Mhz with 3 μW. (b) Upper panel: PL spectra under pulsed σ^- circularly polarised excitation at 1.707 eV and 3 μW. The spectra were recorded under co (σ^-) and cross (σ^+) polarised detection. Lower panel: Degree of circular polarisation recorded at resonant excitation of the intralayer resonances. (c) Upper panel: PL decay traces of the integrated IX emission with same polarisation basis as in (b). Indicated in grey is the instrument response function (IRF). Lower panel: Residuum of the least-square fit with a convolution function of the instrument response function and four exponential decays.

respective peak positions, shown in the lower panel of Fig. 5.3 (a). The resulting g-factors are $g(T) = -14.9 \pm 0.3$ and $g(S) = 12.0 \pm 0.2$, which validates the H_h^h atomic registry [33]. Next, the degree of linear polarisation was probed under the same illumination conditions for both intralayer exciton reservoirs, where the absence of linear degree of polarisation (Fig. 5.3 (b)) confirms the assigned atomic registry and peak labeling by ruling out H_h^M and H_h^X stacking on the basis of optical selection rules. In fact, $P_L = 0$ also rules out quantum wires in the spot [181].

5.2 Time-resolved photoluminescence

After the validation of H_h^h-stacking on the selected position on the WSe_2-$MoSe_2$ HBL, we investigated the time-resolved behaviour of the PL response. To this end, the laser was changed to a pulsed super-continuum white light source (NKT-SuperK Extreme) with filter settings to 10 nm width at 2 MHz pulse frequency. First, the excitation energy was tuned in a PLE experiment with data shown in Fig. 5.4 (a). Due to the broad bandwidth of the excitation energy, no exciton resonances were detected, in strong contrast to narrow-band cw operation as discussed above. Also, the spectral signature changed significantly, as shown in Fig. 5.4 (b), where by reducing the excitation power to 3 μW, a strong substructure emerged. In the following analysis, we neglect possible quantum dots (0D) and 1D stripes, typically

found in the vicinity of extended 2D domains, as their total Intensity contribution is negligible compared to the dominant H_h^h atomic registry and its optical selection rules. In general, we exclude the possibility of partial moiré-fillings similar to Ref. [179]. The singlet state (S) is barely populated and the overall PL intensity reduced significantly, as expected for the lower excitation power. Despite the fact that no intensity difference between the two intralayer excitation energies was found, the total value of P_c reduced for $MoSe_2$ 1s excitation, analogous to the narrow-band cw excitation.

Next, we investigated the time-correlated decay without spectral filtering. PL decay traces were recorded with an avalanche-photodiode (APD, Excelitas SPCM-AQRH) with 600 ps response time. Representative time-traces at zero magnetic field with 16 ps binning are shown for co- and cross-polarised detection under σ^- circular polarised excitation in Fig. 5.4 (c). The decay traces are modeled as a convolution of the instrument response function and multi-exponential decay functions as:

$$I(t) = I_0 + A_0 e^{-2[(t-t_0)/w]^2} + \sum_{k=1}^{N} A_k e^{-t/\tau_k}, \tag{5.2}$$

where I_0 quantifies the APD dark counts and the second term models the IRF approximated by a Gaussian with temporal resolution w and time t_0, set to the maximum of each PL decay trace. The third term is the sum of N individual exponential decay channels with lifetimes τ_k. Here, we use four exponents to perform a least-square fit to the PL decay over 500 ns, shown for the first 10 ns as solid lines in 5.4(c). The residuum exhibits a maximum value of 0.05 in the first 400 ps which reduces to values below 0.005. Best-fit parameters were found as: $\tau_1 = 1.1 \pm 0.2$ ns ($A_1 = 0.7 \pm 0.03$), $\tau_2 = 5 \pm 2$ ns ($A_2 = 0.23 \pm 0.02$), $\tau_3 = 30 \pm 5$ ns ($A_3 = 0.06 \pm 0.01$) and $\tau_4 = 350 \pm 43$ ns ($A_4 = 0.01 \pm 0.005$). Lifetimes in the order of nanoseconds are typical for interlayer exctions [33, 34, 67, 84, 180], where the overall increase from sub-picosecond timescales, typical for ML TMDs [25, 182], is due to the reduced wave-function overlap. The resulting decay times are magnetic field invariant and are insensitive to polarisation. Due to the pulsed excitation resulting in high exciton densities, we ascribe the shortest time τ_1 to Auger-like processes [183], which dominate the optical response. We associate τ_2 with the radiative recombination of the interlayer exciton T, with no field dependence as the reduction of the exciton Bohr radius due to the diamagnetic shift is negligibly small in TMDs at the available field strength [184]. The longer decay times (τ_3 and τ_4) are candidates for field-dependent intervalley scattering mechanisms by exchange interaction or phonon spin-lattice relaxation [185, 186]. However, due to to the small weight of $< 6\%$, no significant field dependence was detected.

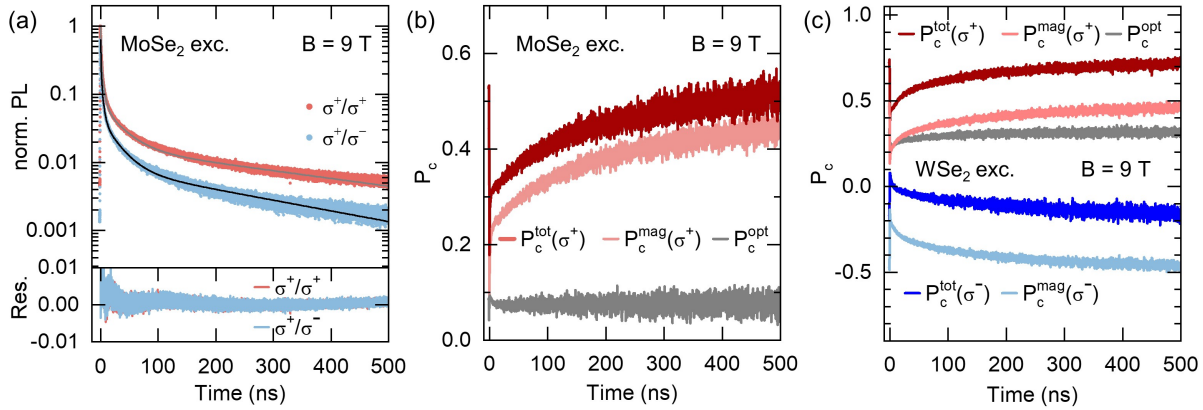

Figure 5.5: Decomposition of the degree of circular polarisation (P_c) from PL decay traces. (a) PL decay traces recorded at 9 T under pulsed σ^+-excitation at 1.642 eV with 2 MHz repetition rate and 3 μW power. Lower panel: Residuum of the least-square fit according to Eq. 5.2. (b) Time-resolved total degree of circular polarisation in σ^+-basis, extracted from PL decay in (a), shown in dark red and labelled as $P_c^{tot}(\sigma^+)$. Decomposition of P_c^{tot} into P_c^{mag} and P_c^{opt} according to Eqs. 5.4-5.6 are plotted in light red and grey. (c) Comparison of the P_c-decomposition at 9 T under σ^+ and σ^- excitation basis via the WSe_2 1s resonance.

5.3 Decomposition of the degree of circular polarisation

In order to access the time-resolved spin dynamics of interlayer excitons, we first analyse the degree of circular polarisation on a theoretical level, where the general formulation is given by Eq. 5.1. Time reversal symmetry provides the following relation:

$$I_{\sigma_1}(\sigma_2, B_z) = I_{-\sigma_1}(-\sigma_2, -B_z), \tag{5.3}$$

where σ_1 refers to the detection- and σ_2 to the excitation-polarisation and the expression $-\sigma$ reverses the polarisation between σ^+ and σ^-. It implies the equivalence of changing the sign of the magnetic field with changing the helicity of light in excitation as well as in detection. The degree of circular polarisation of emitted light has two contributions: the first one is due to a non-zero pump helicity P_c^{opt}, which consist of the difference in co- or cross-polarised detection and the summation of both excitation helicities, defined via:

$$\begin{aligned} P_c^{opt} &= \frac{I_{\sigma^+}(\sigma^+, B_z) - I_{\sigma^+}(\sigma^-, B_z) - I_{\sigma^-}(\sigma^+, B_z) + I_{\sigma^-}(\sigma^-, B_z)}{I_{\sigma^+}(\sigma^+, B_z) + I_{\sigma^+}(\sigma^-, B_z) + I_{\sigma^-}(\sigma^+, B_z) + I_{\sigma^-}(\sigma^-, B_z)}. \\ &= \frac{I_{co}(B_z) - I_{cross}(B_z)}{I_{co}(B_z) + I_{cross}(B_z)}, \end{aligned} \tag{5.4}$$

where $I_{co}(B_z) = I_{\sigma^+}(\sigma^+, B_z) + I_{\sigma^-}(\sigma^-, B_z)$ and $I_{cross}(B_z) = I_{\sigma^+}(\sigma^-, B_z) + I_{\sigma^-}(\sigma^+, B_z)$. Therefore, P_c^{opt} is independent of the excitation basis. The induced polarisation in an ideal system

without dephasing at zero magnetic field would correspond to ±1. With the inclusion of a Zeeman spitting $\Delta_z = g\mu_B B$, population transfer driven by thermalisation leads to the magnetic contribution P_c^{mag}, described by the linear excitation π (summation of σ^+ and σ^-) and the difference between their corresponding detection:

$$\begin{aligned} \pm P_c^{mag}(B_z) &= \pm \frac{I_{\sigma^+}(\sigma^+, B_z) + I_{\sigma^+}(\sigma^-, B_z) - I_{\sigma^-}(\sigma^+, B_z) - I_{\sigma^-}(\sigma^-, B_z)}{I_{\sigma^+}(\sigma^+, B_z) + I_{\sigma^+}(\sigma^-, B_z) + I_{\sigma^-}(\sigma^+, B_z) + I_{\sigma^-}(\sigma^-, B_z)} \\ &= \pm \frac{I_{\sigma^+}(\pi, B_z) - I_{\sigma^-}(\pi, B_z)}{I_{\sigma^+}(\pi, B_z) + I_{\sigma^-}(\pi, B_z)}, \end{aligned} \tag{5.5}$$

where the sign is defined by the excitation helicity of the total degree of polarisation $P_c^{tot}(\sigma^\pm)$, consisting of:

$$P_c^{tot}(\sigma^\pm) = \pm P_c^{mag} + P_c^{opt}, \tag{5.6}$$

with time-reversal symmetry connecting the two polarisation bases of $P_c^{tot}(\sigma^\pm)$. The ratio between the radiative lifetime and the spin dephasing time defines the weight of these two contributions. If the induced polarisation radiates before thermalisation, then P_c^{opt} dominates over P_c^{mag} and vice versa.

To better understand the dominant mechanisms of intervalley scattering and the resulting polarisation defined by the spin distribution of involved excitons in the system, we now apply this decomposition to the PL decay traces. To validate our approach, we first examine the data recorded at 9 T under $MoSe_2$ 1s excitation, shown in Fig. 5.5 (a), where both decays were normalised relative to the maximum counts recorded for $I_{\sigma^+}(\sigma^+, B_z = 9\ T)$. Following Eq. 5.1, we obtain $P_c^{tot}(\sigma^+)$ as a function of time, shown in dark-red in Fig. 5.5 (b). At the moment of light absorption, the population from the preceding pulse reduced to ~0.05% of the injected population per pulse, but defines the polarisation at $t = 500$ ns. Initialisation of the exciton system by a new pulse at $t = 0$ results in $P_c^{tot}(\sigma^+, t = 0, B = 9\ T) = 0.23$. With the use of Eq. 5.4 and 5.5, the time resolved degree of polarisation is shown with additional decomposition into an optical and magnetic contribution. For both contributions, a very fast change in the first nanoseconds is followed by a slower decay (P_c^{opt}) or rise (P_c^{mag}) with a time scale in the order of ~100 ns. After 500 ns, only marginal changes in P_c are observed.

At a magnetic field of $B = 9\ T$, the magnetic component dominates due to the thermalisation driven population transfer between the Zeeman-split reservoirs and shows an offset from the total degree of polarisation by the the optical component, which exhibits only minor changes on short timescales and reaches equilibrium after ~ 10 ns. The total value of P_c^{opt} increases with WSe_2 1s excitation as expected from PL data discussed above, shown in Fig. 5.5 (c). The individual decomposition for σ^+ and σ^- excitation confirms the time-reversal condition (Eq. 5.3) as the magnetic component changes its sign with polarisation, where P_c^{tot} exhibits an offset by P_c^{opt}.

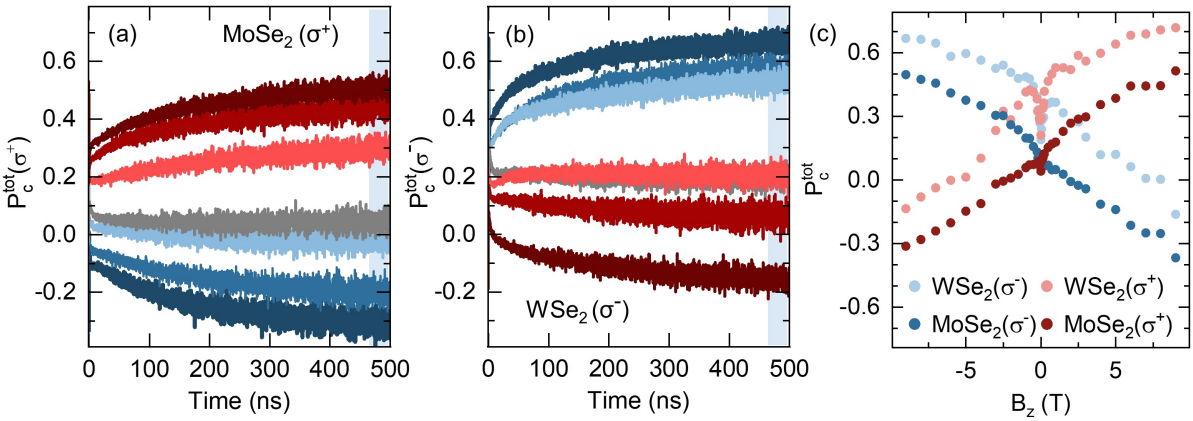

Figure 5.6: Time resolved total degree of circular polarisation for (a) σ^+ and (b) σ^- excitation in resonance with the $MoSe_2$ and WSe_2 1s intralayer exciton respectively. $P_c^{tot}(t)$ was calculated from individual co- and cross polarised PL decay traces and displayed from −9 (dark-blue) to 9 T (dark-red) in 3 T intervals. The blue background schematically depicts extracted steady-state values, shown in (c) for both excitation polarisations and excitation energies.

For each magnetic field in the range of −9 T to 9 T, PL decay traces in four circular polarisation configurations (σ^+/σ^- excitation and detection respectively) were recorded for excitation energies in resonance with $MoSe_2$ and WSe_2 intravalley 1s excitons, as shown in Fig. 5.6 (a) and (b). Here, with the assumption of thermal equilibrium at $t = 500$ ns, the P_c-values for a steady-state analysis were extracted from the mean value of the last 5 ns. The resulting field dependence of P_c^{tot} is shown in Fig. 5.6 (c). We notice an X-like pattern for both excitation conditions shifted in total value by the different optically induced spin polarisations. Two additional features are observed: a non-monotonic behaviour resulting in a polarisation dip around zero field and the interchangeable field or polarisation sign dictated by time-reversal symmetry leading to mirror symmetry in magnetic field.

To better understand the relevant timescales and origins of spin polarisation and dephasing in our HBL system, the same analysis was performed for the magnetic contribution $P_c^{mag}(t)$, shown in Fig. 5.7. At $B = 0$ T, $P_c^{mag}(t) = 0$ for all times as expected. An applied field monotonically increases the absolute value of P_c^{mag}, with similar slopes for all fields. Steady state data extracted from the mean value in the time interval $495-500$ ns is displayed in Fig. 5.7 (b). For cw excitation, the data were extracted from complementary PL spectra and P_c was computed from the integrals over the full spectral range. The resulting values close to zero arise from the continuous repopulation of the system and thereby insufficient thermalisation at high magnetic fields. Interestingly, for pulsed excitation used in PL decay measurements, P_c^{mag} is independent of the excitation energy and therefore only displays population redistribution between the Zeeman-split reservoirs by thermalisation given by:

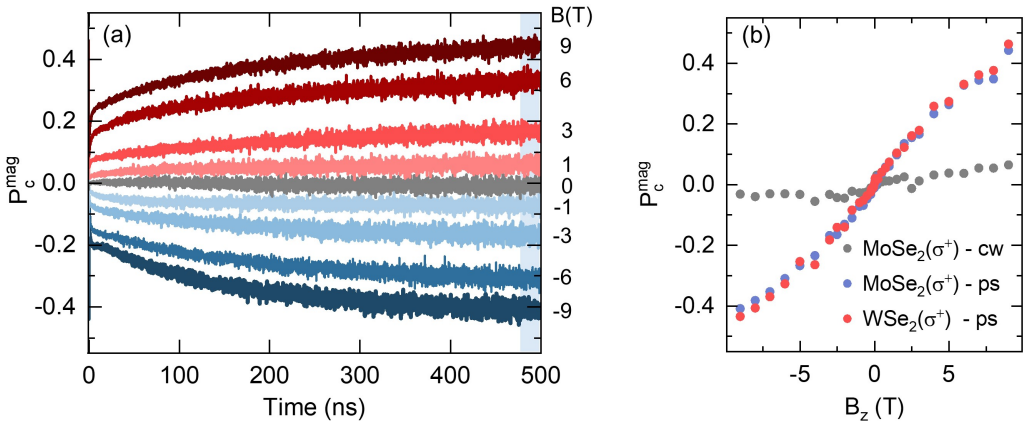

Figure 5.7: (a) $P_c^{mag}(t)$ shown for excitation under σ^+-polarisation in resonance with the $MoSe_2$ 1s exciton as a function of time with varying magnetic field, obtained from individual co- and cross polarised PL decay traces. The blue background schematically depicts extracted steady-state values, shown in (b) for both excitation energies with pulsed light source. Displayed in grey are the values extracted from energy-resolved PL data under continuous-wave excitation.

$$\gamma_{sf}^{ij} = \frac{1}{\tau_{s_0}} e^{\frac{\Delta_{ij}}{2k_B T}}, \tag{5.7}$$

where γ_{sf}^{ij} denotes the exciton spin flip transition from interlayer exciton state IX^i to IX^j, with $i, j \in [\sigma^+, \sigma^-]$ representing the circular polarisation of the involved exciton transition defined by the optical selection rules. The exciton spin-flip time τ_{s_0} is weighted by the Boltzmann distribution, where $\Delta_{ij} = (g_i - g_j)\mu_B B$ represents the Zeeman splitting between exciton states i and j, k_B denotes the Boltzmann factor and T the exciton temperature. We note, that the transitions $IX^i \rightarrow IX^j$ and $IX^j \rightarrow IX^i$ formally differ only by an alternating sign in the Zeeman splitting, leading to an enhanced and suppressed transition rate between IX^i and IX^j according to the energetic ordering of the states defined by the exciton g-factor.

Next, the optical component P_c^{opt} is discussed, where Fig. 5.8 (a) displays representative time-dependent traces for 0 T (grey) and −3/+3 T (blue/red), recorded at both intravalley 1s exciton resonances. Similar to the discussion of PL spectra above, in time-dependent measurements different pump energy leads to a change of P_c^{opt} up to a factor of three. Intravalley polarisation properties of $MoSe_2$ and WSe_2 are inherited by the HBL. Intervalley electron transfer in HBL with type-II band-alignment take place in less than 50 fs [82]. Time-resolved Kerr-spectroscopy measurements on ML WSe_2 has shown, that the hole forming the IX has an extraordinary long spin relaxation time of ~2 μs, compared to ~130 ns for electrons [187]. This implies that due to the type-II band alignment, the injected polarisation of intralayer holes is transferred to interlayer excitons and strongly depends on the ML valley polarisation.

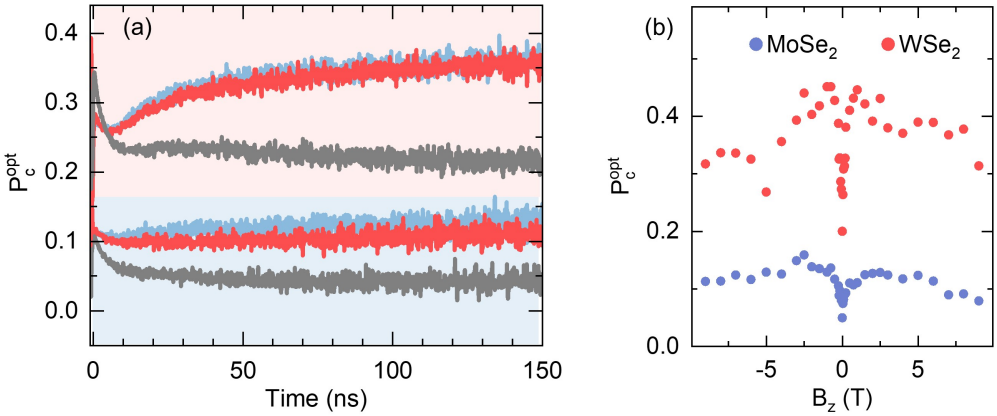

Figure 5.8: (a) $P_c^{opt}(t)$ shown for $MoSe_2$ (blue shaded) and WSe_2 (red-shaded) intralayer excitation as a function of time, where grey represents data recorded at 0 T and blue and red at −3 and 3 T, respectively. After 150 ns, values of $P_c^{opt}(t)$ remain constant, where the steady-state data shown in (b) was extracted from the mean value in the time interval 495 – 500 ns for all magnetic fields.

Fig. 5.8 (b) displays steady-state data extracted from the time-resolved measurements at late times, similar to P_c^{tot} and P_c^{mag} discussed before. In addition to the total offset explained above, we observe a dip centered around zero magnetic field. To further explain the observations mentioned in this section, a model based on rate equations was developed to extract spin-flip times and reproduce the experimental trends.

5.4 Rate equation model

In the following, we present a rate equation model, involving four exciton states, to describe the steady-state and time-resolved field dependence of the magnetic and optical degrees of polarisation of the interlayer exciton PL. With the dominant atomic registry H_h^h in the WSe_2-$MoSe_2$ HBL with type II band alignment, we consider the spin-triplet momentum-direct interlayer excitions denoted as $T^{\pm}$, as well as the momentum-indirect spin-triplet interlayer excitons, denoted as $\tilde{T}^{\pm}$. The sign-index for both reservoirs is defined by the momentum of the hole, where + (−) is related to the K (K') valley of WSe_2. The respective schematic is shown in Fig. 5.9 (a) and the corresponding rate equations are:

$$\frac{\partial T^+}{\partial t} = -\gamma_{tot} T^+ + \gamma_{sf}^{-+} T^- - \gamma_{sf}^{+-} T^+ + \gamma_{vf} \tilde{T}^+ + \gamma_{rel,T^+} IX_{exc} \,,$$

$$\frac{\partial T^-}{\partial t} = -\gamma_{tot} T^- - \gamma_{sf}^{-+} T^- + \gamma_{sf}^{+-} T^+ + \gamma_{vf} \tilde{T}^- + \gamma_{rel,T^-} IX_{exc} \,,$$

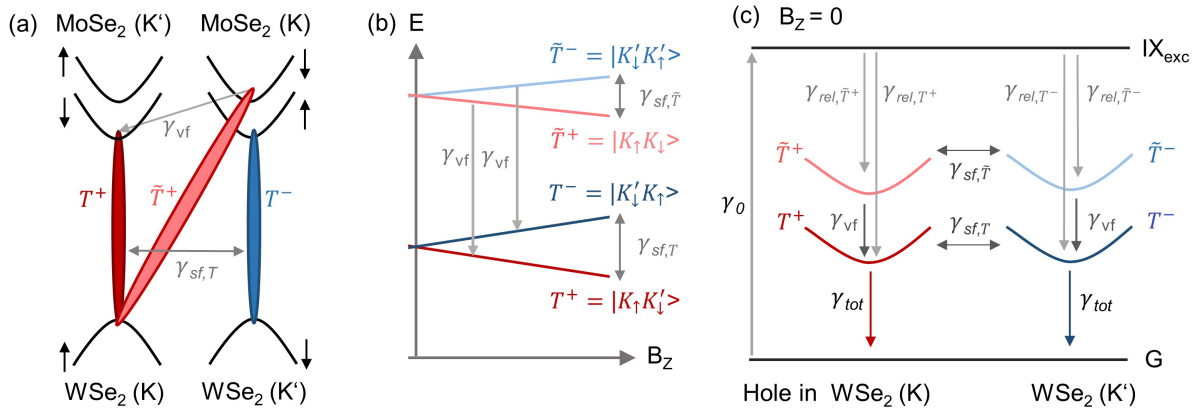

Figure 5.9: Schematic depiction of the rate equation model. (a) Sketch of the type-II band-alignment of the $MoSe_2$-WSe_2 HBL in H_h^h registry. The polarisation of zero momentum interlayer excitons in spin-triplet configuration T and the momentum-indirect spin-equivalent interlayer excitons T̃ is defined by the hole spin residing in the WSe_2 layer. (b) Magnetic field dependence of T and T̃ defined by the Zeeman shift. Exciton g-factors from theory [33] determine the slope of the states involved relative to the 20 meV offset between T and T̃. The spin conserving valley-flip is labeled as γ_{vf}, where the exciton spin-flip rate γ_{sf} is field-dependent. (c) Schematic of the rates used for numerical, time-resolved modelling of the PL decay, magnetic and optical degree of polarisation. After pulsed excitation at $t = 0$, all population resides in IX_{exc} where the branching between T and T̃ as well as between their spin-polarised sub-bands (indicated by the grey arrows) defines the population distribution and the injected pseudo-spin, decaying to the ground state (G) via γ_{tot}.

$$\frac{\partial \tilde{\mathrm{T}}^{+}}{\partial t} = -\gamma_{nr}\tilde{\mathrm{T}}^{+} + \gamma_{sf}^{-+}\tilde{\mathrm{T}}^{-} - \gamma_{sf}^{+-}\tilde{\mathrm{T}}^{+} - \gamma_{vf}\tilde{\mathrm{T}}^{+} + \gamma_{rel,\tilde{\mathrm{T}}^{+}} IX_{exc}\,,$$

$$\frac{\partial \tilde{\mathrm{T}}^{-}}{\partial t} = -\gamma_{nr}\tilde{\mathrm{T}}^{-} - \gamma_{sf}^{-+}\tilde{\mathrm{T}}^{-} + \gamma_{sf}^{+-}\tilde{\mathrm{T}}^{+} - \gamma_{vf}\tilde{\mathrm{T}}^{-} + \gamma_{rel,\tilde{\mathrm{T}}^{-}} IX_{exc}\,,$$

$$\frac{\partial IX_{exc}}{\partial t} = -(\gamma_{rel,\mathrm{T}^{+}} + \gamma_{rel,\mathrm{T}^{-}} + \gamma_{rel,\tilde{\mathrm{T}}^{+}} + \gamma_{rel,\tilde{\mathrm{T}}^{-}})IX_{exc} + \gamma_0 G\,,$$

$$\frac{\partial G}{\partial t} = +\gamma_{tot}(\mathrm{T}^{+} + \mathrm{T}^{-}) + \gamma_{nr}(\tilde{\mathrm{T}}^{+} + \tilde{\mathrm{T}}^{-}) - \gamma_0 G\,, \tag{5.8}$$

with $\gamma_{tot} = \gamma_{rad} + \gamma_{nr}$ being the transition from $\mathrm{T}^{\pm}$ to the ground state consisting of a radiative (γ_{rad}) and non-radiative recombination (γ_{nr}) of the population. Losses from the valley-unlike exciton state $\tilde{\mathrm{T}}^{\pm}$ include non-radiative decay γ_{nr} and the spin-conserving valley flip towards the energetically lower T state, denoted as γ_{vf}. The exciton spin-flip rates γ_{sf}^{ij}, described by Eq. 5.7, are reservoir specific. Their magnetic field dependence is illustrated in Fig. 5.9 (b), where the notation $\mathrm{T}^{+} = |K_{\downarrow}K'_{\uparrow}\rangle$ refers to the exciton consisting of a hole with spin-down in the K valley of WSe_2 and a spin-up electron in the K'-valley of $MoSe_2$. The polarisation-sensitive interlayer exciton formation is described by the relaxation rates $\gamma_{rel} = \sum_i \gamma_{rel,i}$, where $i \in \{\mathrm{T}^{+}, \mathrm{T}^{-}, \tilde{\mathrm{T}}^{+}, \tilde{\mathrm{T}}^{-}\}$, and possible re-population from the ground state (G) to the excited state IX_{exc} is introduced by the rate γ_0.

We rewrite the rate equations by defining the total exciton population as the sum of populations in each valley, $\mathrm{T} = \mathrm{T}^{+} + \mathrm{T}^{-}$, and introduce the valley polarisation as the difference in population via $V_{\mathrm{T}} = \mathrm{T}^{+} - \mathrm{T}^{-}$, resulting in:

$$\frac{\partial \mathrm{T}}{\partial t} = -\gamma_{tot}T + \gamma_{vf}\tilde{\mathrm{T}} + \gamma_{rel,\mathrm{T}} IX_{exc}\,,$$

$$\frac{\partial \tilde{\mathrm{T}}}{\partial t} = -\gamma_{nr}\tilde{\mathrm{T}} - \gamma_{vf}\tilde{\mathrm{T}} + \gamma_{rel,\tilde{\mathrm{T}}} IX_{exc}\,,$$

$$\frac{\partial V_{\mathrm{T}}}{\partial t} = -\gamma_{tot}V_{\mathrm{T}} + \gamma_{vf}V_{\tilde{\mathrm{T}}} - \gamma_{sf,\mathrm{T}}(V_{\mathrm{T}} - P^0_{\mathrm{T}}\mathrm{T}) + \gamma^{\Delta}_{rel,\mathrm{T}} IX_{exc}\,,$$

$$\frac{\partial V_{\tilde{\mathrm{T}}}}{\partial t} = -\gamma_{nr}V_{\tilde{\mathrm{T}}} - \gamma_{vf}V_{\tilde{\mathrm{T}}} - \gamma_{sf,\tilde{\mathrm{T}}}(V_{\tilde{\mathrm{T}}} - P^0_{\tilde{\mathrm{T}}}\tilde{\mathrm{T}}) + \gamma^{\Delta}_{rel,\tilde{\mathrm{T}}} IX_{exc}\,,$$

$$\frac{\partial IX_{exc}}{\partial t} = -\gamma_{rel}IX_{exc} + \gamma_0 G\,,$$

$$\frac{\partial G}{\partial t} = +\gamma_{tot}\mathrm{T} + \gamma_{nr}\tilde{\mathrm{T}} - \gamma_0 G\,, \tag{5.9}$$

with $\gamma^{\Delta}_{rel,\mathrm{T}/\tilde{\mathrm{T}}} = \gamma^{+}_{rel,\mathrm{T}/\tilde{\mathrm{T}}} - \gamma^{-}_{rel,\mathrm{T}/\tilde{\mathrm{T}}}$ describing polarisation-specific branching from the excited

state. To further analyse the exciton spin-flips, we used the identities:

$$P^0 = -\tanh(\beta),\ \beta = \frac{\Delta_{ij}}{2k_B T}\ ,$$

$$\gamma_{sf} = \gamma_{sf}^{+-} + \gamma_{sf}^{-+} = 2\gamma_{sf}^{0}\cosh(\beta)\ , \tag{5.10}$$

where β is the Boltzmann factor defined by the exciton g-factor at a given temperature T and magnetic field, with Δ_{ij} denoting the Zeeman splitting of the reservoir defined by the superscript T/$\tilde{\text{T}}$. A schematic of the involved rates (see Eq. 5.26) is shown in Fig. 5.9 (c). The spin coherence rate γ_{sf}, defined via Eq. 5.10, is of particular interest for further analysis and will be discussed in more detail below.

5.4.1 Long-range Coulomb-induced exchange interaction

So far, the transition rates between the polarisation-resolved exciton states are defined by population transfer between the Zeeman-split sub-bands, purely driven by thermalisation similar to previous work [111]. However, external magnetic field strongly impacts the spin-distribution of excited charge carriers. The underlying physical principle was first discovered and studied in the resonance fluorescence of gases by Hanle, where depolarisation of luminescence by a transverse magnetic field was explained by the precession of excited electron spins [188]. In essence, the precession is described by a Lamor frequency $\Omega = g\mu_B B/\hbar$, where g denotes the g-factor and μ_B the Bohr magneton. If the magnetic field is perpendicular to the exciting light beam B $\perp S_0$, where S_0 is the pseudospin in initial direction, the component of the spin along the direction of the beam changes periodically with frequency Ω. Therefore at time t after excitation, the spin of the electrons is given by $S_z = S_0\cos(\Omega t)\exp(-t/\tau_s)$, where the spin relaxation time τ_s was introduced. The average value of S_z is derived by averaging this expression with the distribution of lifetimes $W(t)$ via [189]:

$$S_z = S_0\int_0^\infty dt\ W(t)e^{-t/\tau_s}\cos(\Omega t). \tag{5.11}$$

With the assumption of thermalised charge carriers, we have $W(t) = 1/\tau_{rad}\exp(-t/\tau_r)$, where τ_{rad} is the radiative lifetime and τ_s denotes the spin relaxation time. It follows:

$$S_z(B) = \frac{S_z(0)}{1+(\Omega T_s)^2},\ S_z(0) = \frac{S_0}{1+\tau_{rad}/\tau_s}, \tag{5.12}$$

where the spin lifetime T_s is defined via $1/T_s = 1/\tau_{rad} + 1/\tau_s$. Equations 5.12 allow the experimental determination of spin-dephasing times τ_s in steady state by recording the degree of PL polarisation as a function of the magnetic field. If the g-factor is known, the

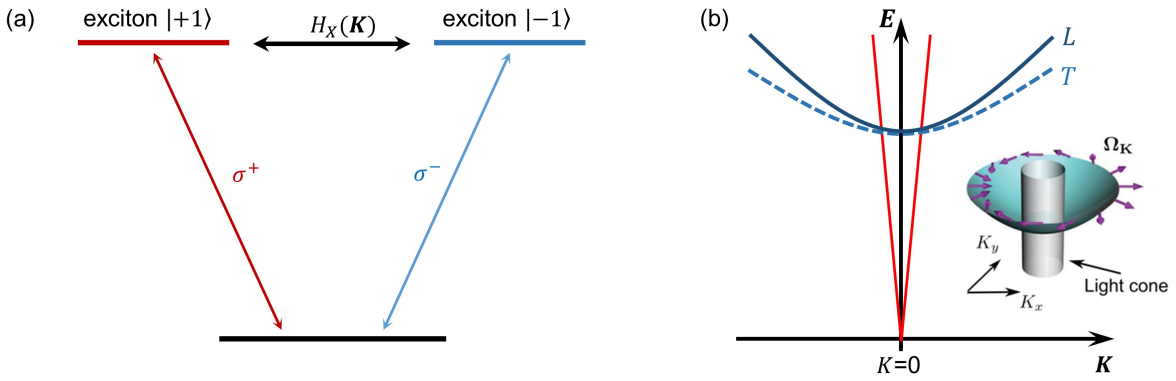

Figure 5.10: (a) Optical selection rules of the circularly polarised eigenstates for ML A-excitons and their long-range Coulomb-induced exchange coupling. (b) Sketch of the exciton dispersion illustrating the splitting of the bright doublet into linearly polarised eigenstates, with either longitudinal (L) or transversal (T) microscopic dipolar orientation relative to the exciton wavevector K (shown not to scale). The photon dispersion is shown in red lines. Inset: Orientation of the momentum-dependent effective in-plane field Ω_k (purple arrows) around the exciton dispersion. Figures adapted from Ref. [196].

half-width of the magnetic depolarisation $B_{1/2} = \hbar/g\mu_B T_s$, commonly referred to as the Hanle curve, give direct access to τ_s. This theoretical treatment was used in numerous works on GaAs [190, 191], quantum wells [192] and TMDs [185, 193–195].

In TMDs, due to the strong Coulomb interactions present, light-matter coupling is dominated by excitons, where long-range exchange interaction couples the excitons of the two spin-valleys and thereby gives rise to an efficient decay mechanism for exciton polarisation [35, 36, 196–198]. The admixture of the valleys at the high symmetry points K and K' by exchange interaction is illustrated in Fig. 5.10, where an exciton in the K valley effectively recombines and produces an exciton in the K' valley without any momentum-transfer or spin-flip of individual charge carriers. This process is more comprehensible if one considers an exciton as a microscopic dipole, oscillating at its resonance frequency either longitudinal (L) or transversal (T) to the in-plane center-of-mass wavevector K_{exc}. The splitting of these states (LT-splitting) acts as an effective magnetic field which mixes the σ^+ and σ^- polarised excitons [36, 192, 199]. The depolarisation timescale depends on the oscillator strength and the wave-function overlap of the electron and hole, and therefore only optically active excitons are affected by long-range exchange interaction. In the case of interlayer excitons, this mechanism is expected to be weaker leading to longer polarisation lifetimes in the order of nanoseconds [173, 200].

The lack of inversion symmetry in TMD monolayers allow Dyakonov-Perel type mechanisms, where scattering at defects, phonons or impurities redistributes the spin during its precession described by the kinetic equation [36, 189, 201]:

$$\frac{\partial \mathbf{S_K}}{\partial t} = \Omega_\mathbf{K} \times \mathbf{S_K} + \frac{\mathbf{S}}{\tau_s} + Q\{S_K\}, \tag{5.13}$$

where $Q\{S_K\}$ is the collision integral describing the involved scattering processes and Ω_K denotes the momentum dependent precession frequency. Eq. 5.13 is solved exactly, e.g. as described in Appendix of Ref. [192], with the solution being:

$$\frac{1}{T_s} = \frac{\Omega_K^2 \tau_2^*}{1 + (\Omega_0 \tau_2^*)^2}, \tag{5.14}$$

where τ_2^* denotes the momentum relaxation time of second angular harmonics of the distribution function. The linewidth Γ related to this dephasing time is defined via $\Gamma \approx \hbar/\tau_2^*$, and Ω_0 is the frequency associated with the external applied field B_z. In the strong scattering regime $\Omega_K \tau_{sc} \ll 1$, the spin decays exponentially and with the assumption, that the spread of excitons in energy space is limited by collision broadening and not by kinetic energy distribution, the spin relaxation time is given by [36, 192, 196]:

$$\frac{1}{\tau_s} = \Omega_K^2 \tau_2^*. \tag{5.15}$$

Inserting into Eq. 5.14 and using $\Gamma \approx \hbar/\tau_2^*$ and $\Delta_z = \hbar\Omega_0$, we obtain for the field-dependent exciton spin flip rate γ_{sf}:

$$\gamma_{sf}(B) = \gamma_{sf}^{th} \frac{1}{1 + (\Delta_z/\Gamma)^2} = \frac{2}{\tau_{s,0}} \frac{\cosh(\beta)}{1 + (\Delta_z/\Gamma)^2}\,, \tag{5.16}$$

where we identified Eq. 5.7 as the thermal spin-flip rate γ_{sf}^{th}, omitted the reservoir notation and used the identities defined via Eq. 5.10.

5.4.2 Steady-state solution

To study the field-dependent behaviour of P_c^{mag} and P_c^{opt} as extracted at $t = 500$ ns, we neglect the non-radiative recombination of $\tilde{\mathrm{T}}$ and set all time derivatives in the rate equations 5.26 to zero, resulting in:

$$\tilde{\mathrm{T}} = \frac{\gamma_{rel,\tilde{\mathrm{T}}}}{\gamma_{vf}},$$

$$T = \frac{\gamma_{rel}}{\gamma_{tot}},$$

$$V_{\tilde{\mathrm{T}}} = \frac{P^0_{\tilde{\mathrm{T}}}\tilde{\mathrm{T}}}{1+\gamma_{vf}/\gamma_{sf,\tilde{\mathrm{T}}}} + \frac{\gamma^{\Delta}_{rel,\tilde{\mathrm{T}}}}{\gamma_{vf}+\gamma_{sf,\tilde{\mathrm{T}}}},$$

$$V_{\mathrm{T}} = \frac{P^0_{\mathrm{T}}\mathrm{T}}{1+\gamma_{tot}/\gamma_{sf,\mathrm{T}}} + \frac{\gamma_{vf}V_{\tilde{\mathrm{T}}}}{\gamma_{tot}+\gamma_{sf,\mathrm{T}}} + \frac{\gamma^{\Delta}_{rel,\mathrm{T}}}{\gamma_{tot}+\gamma_{sf,\mathrm{T}}} \tag{5.17}$$

where we set $IX_{exc} \equiv 1$. The degree of circular polarisation is defined analogously to Eq. 5.1 by the ratio of the valley polarisation to the total exciton population of T via:

$$P_c = \frac{V_{\mathrm{T}}}{\mathrm{T}}. \tag{5.18}$$

The valley polarisation and population of $\tilde{\mathrm{T}}$ hereby only indirectly influence the experimental results as no direct radiative recombination was included due to the momentum mismatch. Subsequently inserting the results into Eq. 5.18, we obtain:

$$P_c = \frac{P^0_{\mathrm{T}}}{1+\gamma_{tot}/\gamma_{sf,\mathrm{T}}} + \frac{P^0_{\tilde{\mathrm{T}}}}{1+\gamma_{vf}/\gamma_{sf,\tilde{\mathrm{T}}}} \cdot \frac{\gamma_{tot}}{\gamma_{tot}+\gamma_{sf,\mathrm{T}}} \cdot \frac{\gamma_{rel,\tilde{\mathrm{T}}}}{\gamma_{rel}}$$

$$+ \frac{\gamma_{tot}}{\gamma_{tot}+\gamma_{sf,\mathrm{T}}} \cdot \frac{\gamma^{\Delta}_{rel,\mathrm{T}}}{\gamma_{rel}} + \frac{\gamma_{tot}}{\gamma_{tot}+\gamma_{sf,\mathrm{T}}} \cdot \frac{\gamma_{vf}}{\gamma_{vf}+\gamma_{sf,\tilde{\mathrm{T}}}} \cdot \frac{\gamma^{\Delta}_{rel,\tilde{\mathrm{T}}}}{\gamma_{rel}} \tag{5.19}$$

To further simplify Eq. 5.19 and to address the question how the population is distributed between T and $\tilde{\mathrm{T}}$ after pulsed excitation, we introduce the branching ratio $b = \gamma_{rel,\tilde{\mathrm{T}}}/\gamma_{rel}$. The induced optical polarisation by circularly polarised excitation $P^{\mathrm{T}/\tilde{\mathrm{T}}}_{ind}$, and therefore, the valley selective population distribution is described by the ratio:

$$P^{\mathrm{T}/\tilde{\mathrm{T}}}_{ind} = \frac{\gamma^{\Delta}_{rel,\mathrm{T}/\tilde{\mathrm{T}}}}{\gamma_{rel}}. \tag{5.20}$$

Rewriting Eq 5.16 by introducing a field-dependent parameter $\alpha_{\mathrm{T}/\tilde{\mathrm{T}}}(B)$ as:

$$\gamma_{sf}(B) = \gamma^0_{sf}\frac{2\cosh(\beta)}{1+(\Delta_{ij}/\Gamma)^2} = \gamma^0_{sf}\alpha(B), \tag{5.21}$$

where $\beta, \Delta_{ij}, \gamma_{sf}(B)$ as well as γ^0_{sf} are reservoir-specific (T or $\tilde{\text{T}}$). The redefinition shows that the spin-flip time $\gamma^0_{sf,\text{T}/\tilde{\text{T}}}$ does only contribute to the steady-state solution in proportion to the reservoir-specific losses γ_{tot} and γ_{vf}. Therefore, with the definitions:

$$r_T = \frac{\gamma^0_{sf,\text{T}}}{\gamma_{tot}},\ r_{\tilde{\text{T}}} = \frac{\gamma^0_{sf,\tilde{\text{T}}}}{\gamma_{vf}}, \tag{5.22}$$

we reduce the parameter space and identify reservoir-specific contributions. This in turn allows us to identify the four terms in Eq. 5.19 as the magnetically and optically induced polarisation of the reservoirs T and $\tilde{\text{T}}$, respectively, as:

$$P_c^{tot} = P^{\text{T}}_{mag} + P^{\tilde{\text{T}}}_{mag} + P^{\text{T}}_{opt} + P^{\tilde{\text{T}}}_{opt}, \tag{5.23}$$

where the explicit expressions are:

$$\begin{aligned}
P^{\text{T}}_{mag} &= \frac{P^0_{\text{T}}}{1 + 1/(r_{\text{T}}\alpha_{\text{T}}(B)) =} \\
P^{\tilde{\text{T}}}_{mag} &= \frac{P^0_{\tilde{\text{T}}}}{1 + 1/(r_{\tilde{\text{T}}}\alpha_{\tilde{\text{T}}}(B))} \cdot \frac{b}{1 + r_{\text{T}}\alpha_{\text{T}}(B)} \\
P^{\text{T}}_{opt} &= \frac{P^{\text{T}}_{ind}}{1 + r_{\text{T}}\alpha_T(B)} \\
P^{\tilde{\text{T}}}_{opt} &= \frac{P^{\tilde{\text{T}}}_{ind}}{1 + r_{\tilde{\text{T}}}\alpha_{\tilde{\text{T}}}(B)} \cdot \frac{1}{1 + r_{\text{T}}\alpha_{\text{T}}(B)}.
\end{aligned} \tag{5.24}$$

Here, the third relation is equivalent to the description of ML steady-state polarisation [36, 186], similar to Eq. 5.12. These identities now are used to analyse the steady-state data shown in Chap. 5.3 and summarised in Fig. 5.11. Least-square fits of $P_c^{tot}(B)$ were computed for both excitation polarisations, with parameters being the effective exciton temperature T, the branching ratio b as well as the exchange-interaction induced splitting Γ, the induced optical polarisation P_{ind} and the ratio of the spin-flip rate and the depopulation rate $r_{\text{T}/\tilde{\text{T}}}$ for both exciton reservoirs. Unbound fits resulted in an unrealistic exciton temperature and therefore the upper bound of $T_{max} = 10$ K was introduced. Otherwise free-fit results show close to equal population distribution into both exciton reservoirs, with similar induced polarisation and negligible exchange interaction for the momentum-indirect reservoir $\tilde{\text{T}}$. Therefore, we set $b = 0.5$, $P^{\text{T}}_{ind} = P^{\tilde{\text{T}}}_{ind}$ as well as $\Gamma_{\tilde{\text{T}}} = \infty$. The resulting parameters for WSe_2 1s resonant pumping are: $T = 9.3$ K, $\Gamma_{\text{T}} = 0.1$ meV, $r_{\text{T}} = 0.42$ and $r_{\tilde{\text{T}}} = 0.2$, with an induced optical polarisation of $P^{\text{T}}_{ind} = P^{\tilde{\text{T}}}_{ind} = 0.26$. Only the latter changes significantly for the data

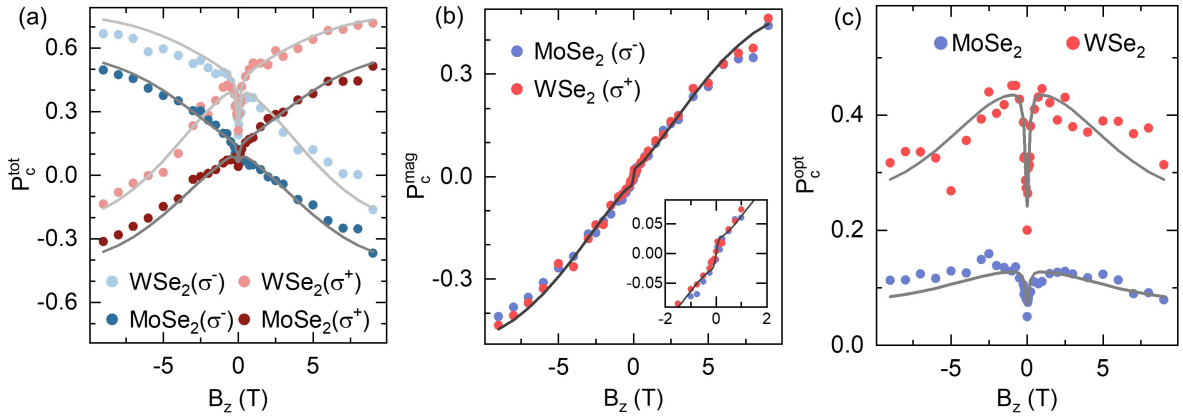

Figure 5.11: Steady-state analysis of the (a) total, (b) magnetically and (c) optically induced degree of circular polarisation. Least-square model-fits using Eq. 5.23 and 5.24 were performed for P_c^{tot}. The resulting fit parameters were used to model the decomposition into P_c^{mag} and P_c^{opt}, where only P_{ind} differs for $MoSe_2$ and WSe_2 excitation. All numerical results are displayed by grey solid lines. Inset in (b) shows the data recorded from −2 to 2 T.

recorded under $MoSe_2$ 1-s pumping, namely $P_{ind} = 0.076$. This is in accord with the steady-state data of P_c^{mag} and P_c^{opt} shown in Fig. 5.11 (b) and (c) for both pump energies, where the former shows identical values and the latter displays similar functional form with an offset. This offset is set by P_{ind}, whereas the functional form strongly depends on the resonance condition defined by Γ. We note that attempts to reproduce the data without the reservoir $\tilde{T}$ resulted in unrealistically high temperatures, whereas its inclusion captures P_c^{mag} even at small fields (see inset in Fig. 5.11). The effective exciton temperature $T = 9.3\ K$ is in accord with previous reports [111] and deviates from the nominal bath temperature of 4 K due to laser-heating and band filling. We also note stronger variations in P_c^{opt} for WSe_2 1s excitation, and attribute it to the transfer of polarisation from the excited excitons to the residual charge carriers from unintentional sample doping [187].

5.4.3 Numerical time-dependent solution

To further test our model and to extract radiative, non-radiative and spin-flip timescales, we solved all ordinary differential equations of first order numerically to model the magnetic and optical component of P_c as well as the observed PL intensity decay. To this end, we included non-radiative Auger-processes with a quadratic dependence on the population in each reservoir [183]. This assumption is justified, as pulsed excitation creates a high population density which promotes non-radiative bi-molecular decay. Therefore, from the PL decay analysis discussed in Chap. 5.2, we attribute the leading timescale of 1.1 ns (70%) to Auger-decay γ_{aug}. Converting the polarisation specific reservoir auger rate $\gamma_{aug} \propto T^2_{+/-}$ into the valley polarisation formalism used above (e.g. $V_T = T^+ - T^-$ and $T = T^+ + T^-$), we

obtain:

$$\gamma_{aug}(\mathrm{T}) = -\frac{\gamma^0_{aug}}{2}(\mathrm{T}^2 + V_\mathrm{T}^2),$$

$$\gamma_{aug}(V_\mathrm{T}) = -\gamma^0_{aug}\mathrm{T}\cdot V_\mathrm{T}, \tag{5.25}$$

with similar expressions for $\tilde{\mathrm{T}}$. We expand Eq. 5.26 accordingly and include a linear generation rate γ_0 as an approximation to Auger-excited higher energy population decaying back to T and $\tilde{\mathrm{T}}$ (See Fig. 5.9c). The resulting rate equations are:

$$\begin{aligned}
\frac{d\mathrm{T}}{dt} &= -\gamma_{tot}\mathrm{T} + \gamma_{vf}\tilde{\mathrm{T}} + \gamma_{rel,\mathrm{T}} IX_{exc} - \frac{\gamma^0_{aug}}{2}(\mathrm{T}^2 + V_\mathrm{T}^2),\\
\frac{d\tilde{\mathrm{T}}}{dt} &= -\gamma_{nr}\tilde{\mathrm{T}} - \gamma_{vf}\tilde{\mathrm{T}} + \gamma_{rel,\tilde{\mathrm{T}}} IX_{exc} - \frac{\gamma^0_{aug}}{2}(\tilde{\mathrm{T}}^2 + V_{\tilde{\mathrm{T}}}^2),\\
\frac{dV_\mathrm{T}}{dt} &= -\gamma_{tot}V_\mathrm{T} - \gamma_{sf,\mathrm{T}}(V_\mathrm{T} - P^0_\mathrm{T}\mathrm{T}) + \gamma_{vf}V_{\tilde{\mathrm{T}}} + \gamma^\Delta_{rel,\mathrm{T}} IX_{exc} - \gamma^0_{aug}\mathrm{T}\, V_\mathrm{T},\\
\frac{dV_{\tilde{\mathrm{T}}}}{dt} &= -\gamma_{nr}V_{\tilde{\mathrm{T}}} - \gamma_{sf,\tilde{\mathrm{T}}}(V_{\tilde{\mathrm{T}}} - P^0_{\tilde{\mathrm{T}}}\tilde{\mathrm{T}}) - \gamma_{vf}V_{\tilde{\mathrm{T}}} + \gamma^\Delta_{rel,\tilde{\mathrm{T}}} IX_{exc} - \gamma^0_{aug}\tilde{\mathrm{T}}\, V_{\tilde{\mathrm{T}}},\\
\frac{dIX_{exc}}{dt} &= -\gamma_{rel} IX_{exc} + \gamma_0 G,\\
\frac{dG}{dt} &= +\gamma_{tot}\mathrm{T} + \gamma_{nr}\tilde{\mathrm{T}} - \gamma_0 G
\end{aligned} \tag{5.26}$$

We now use this set of equations to analyse the time-dependent change in population and polarisation. Hereby, we fix all parameters resulting from the steady-state model shown above, leaving γ_{form}, γ_r and γ_{vf}, as well as γ^0_{aug} and γ_0 as the remaining free parameters.

The initial distribution of population is defined by the leading timescale for the branching from IX_{exc} to T or $\tilde{\mathrm{T}}$ by the exciton formation rate $\gamma_{form} = 2$ ps^{-1}, in accord with energy-state-resolved ultrafast microspectroscopy measurements investigating interlayer formation [82, 202]. As we fixed the branching $b = 0.5$, we distribute both exciton population equally by $\gamma_{g_\mathrm{T}} = \gamma_{g_{\tilde{\mathrm{T}}}} = \gamma_{form}$, with a polarisation dependent weight defined by $P^\mathrm{T}_{ind} = P^{\tilde{\mathrm{T}}}_{ind}$ via $\gamma^\Delta_{rel} = P_{ind}\cdot\gamma_{rel}$.

The other rates are chosen to capture the time-dependent evolution of polarisation for all magnetic fields, shown in Fig. 5.12. We find best correspondence between the data and our model for $\gamma_{aug} = 5$ ns^{-1} ($\tau_{aug} = 0.2ns$), faster than the leading timescale of $\tau_1 = 1.1 \pm 0.2$ ns extracted from multi-exponential fitting in Sec. 5.2 and limited by the APD response time of ~ 600 ps. The radiative and non-radiative linear losses from T described by $\gamma_{\mathrm{tot}} = 0.3$ ns^{-1}

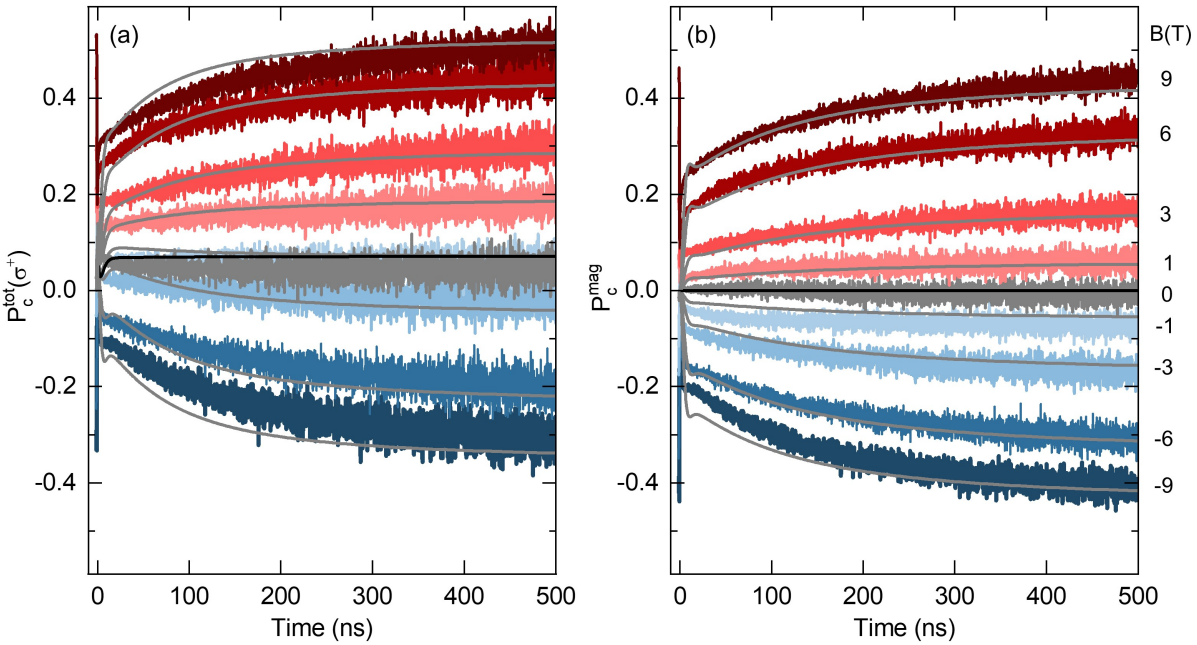

Figure 5.12: Numerical solution of the time-dependent rate-equation model. (a) $P_c^{tot}(t)$ and (b) $P_c^{mag}(t)$, shown for excitation under σ^+-polarisation in resonance with the $MoSe_2$ 1s exciton with varying magnetic field (from −9 T, dark-blue to +9 T, dark-red), obtained from individual co- and cross polarised PL decay traces. Grey (black for $B = 0$ T) solid lines represent the result of Eqs. 5.26 for each magnetic field, respectively.

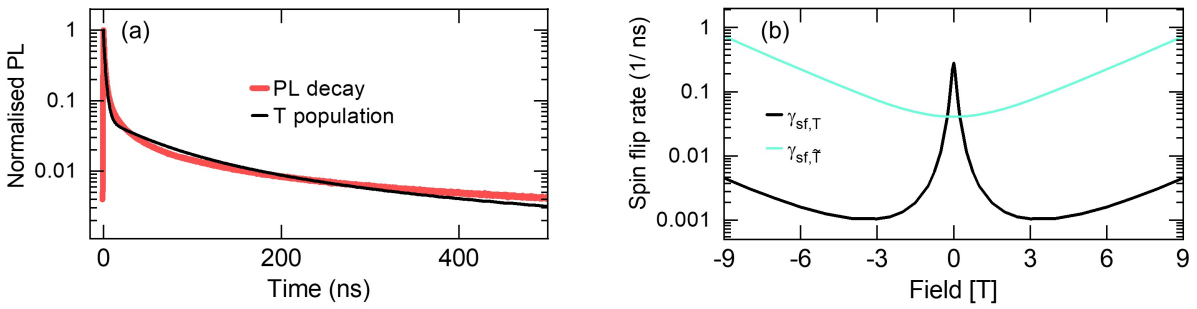

Figure 5.13: (a) Modeled exciton population T at +9 T (black line) compared to the summation of all four PL decay traces recorded with different excitation and detection bases (red). The initial decay is well captured, with deviations for the total population below 10% at longer time scales. (b) Resulting exciton spin-flip rates as a function of the magnetic field according to Eq. 5.16 for T and $\tilde{T}$, where the field-dependence for the latter is purely thermal due to $\Gamma_{\tilde{T}} = \infty$.

T	b	γ_{form}	γ_0	γ_{aug}	γ_r	γ_{vf}	$\gamma^0_{sf,\mathrm{T}}$	$\gamma^0_{sf,\tilde{\mathrm{T}}}$	Γ_T	$P^{\mathrm{T}/\tilde{\mathrm{T}}}_{ind}(\mathrm{MoSe_2/WSe_2})$
9.3	0.5	2	0.05	5	0.3	0.1	0.14	0.02	0.1	0.076 / 0.26
K	-	ps^{-1}	ns^{-1}	ns^{-1}	ns^{-1}	ns^{-1}	ns^{-1}	ns^{-1}	meV	-

Table 5.1: Summary of all parameters extracted first from least-square fits to steady-state values of P_c^{tot}, and subsequently from time-dependent modelling of the PL decay as well as the polarisation dynamics.

($\tau_\mathrm{tot} = 3.34$ ns) fit well to the second leading timescale of $\tau_2 = 5 \pm 2$ ns. The other timescales τ_3 and τ_4 from multi-exponential fitting mismatch the rates extracted by the model with an overall 7% signal contribution.

All fit parameters are summarised in Tab. 5.1. Overall, the agreement with $P_c^{mag}(t)$ displayed in Fig. 5.12 (b) strongly supports our model. Here, the valley-flip timescale of $\tau_{vf} \sim 10$ ns enables an efficient decay channel to the radiative population T. After initial fast interlayer formation [203], the exciton spin-flip rate $\gamma_{sf,\mathrm{T}}$ in combination with a fast Auger decay leads to a rapid change in P_c in the first nanoseconds. As $\gamma_{sf,\tilde{\mathrm{T}}}$ is several times larger than $\gamma_{sf,\mathrm{T}}$ for fields higher than ~ 0.5 T and the population in $\tilde{\mathrm{T}}$ is equally feeding both polarisation-resolved valleys of T via field-independent valley-flip, after the first nanoseconds, a slow and saturating change in P_c is observed until thermal equilibrium is reached and thus, P_c stays constant. We note that previous models [204] describing the saturation of P_c via $P_c(t) = P_f + (P_i - P_f)e^{-t/\tau}$, where P_f and P_i are the final and initial polarisation and τ is the spin relaxation time, do not reproduce our data and therefore motivate the involvement of multiple exciton reservoirs as presented in this work.

The modelled PL decay is shown in Fig. 5.13 (a). The total exciton population $\mathrm{T} = \mathrm{T}^+ + \mathrm{T}^-$ is compared to the sum of all four circularly polarised excitation and detection bases, which effectively corresponds to linear excitation ($P_{ind} = 0$) with detection in σ^+ as well as σ^-. The result captures ~90% of population decay observed in the first nanoseconds and generally follows the functional form of the data. The magnetic-field dependent exciton spin-flip times according to Eq. 5.16 are shown in Fig. 5.13 (b). The field dependency of $\gamma_{sf,\tilde{\mathrm{T}}}$ is purely thermal ($\Gamma_{\tilde{\mathrm{T}}} = \infty$), as the longitudinal-transverse splitting mediated by interlayer exchange interaction only allows relaxation for momentum-direct excitons [36]. The estimated value for the width parameter $\Gamma_\mathrm{T} = 0.1$ meV lies in the same order of magnitude as previous reports for other TMD HBL [185, 186].

Finally, it is worth pointing out discrepancies between the experimental data and model results. The deviations, displayed exemplary for the optical contributions in Fig. 5.14, may stem from single-particle spin flips, one-phonon spin-lattice relaxation [185] or polarisation transfer of the induced optical polarisation to the free charge carriers from unintentional doping [187].

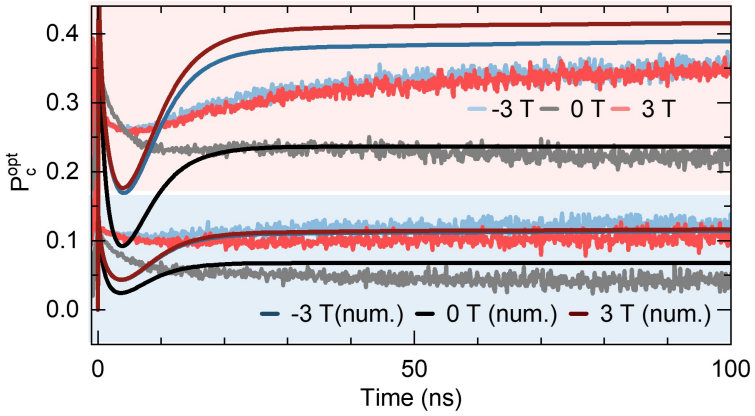

Figure 5.14: Numerical solution for $P_c^{opt}(t)$ shown for $MoSe_2$ (blue shaded) and WSe_2 (red-shaded) intralayer excitation, identical to Fig. 5.8.

5.5 Discussion

Similar to previous reports on spin dynamics of GaAs/AlAs quantum wells with type-II band alignment [205, 206], the degree of polarisation in HBL system was modeled with kinetic equations between Zeeman-split subbands including non-radiative and radiative population redistribution of excitons as a result of spin relaxation as well as thermalisation [111, 186, 207].

Contrary to the above mentioned example of GaAs/AlAs quantum wells, where long-range exchange interactions were neglected due to the momentum-indirect nature of involved excitons, TMD systems in general exhibit strong spin-orbit coupling and Coulomb interactions [36, 196], leading to exchange-mediated exciton spin-flips without momentum transfer as the main source of decoherence at small magnetic fields. The attempt to extract the spin-flip time from the dip of P_c^{opt} via $\tau_{sf} \approx \hbar/(g\mu_B B_{1/2})$, similar to Ref. [193] and with $B_{1/2}$ being the half width at half maximum, results in timescales of the order of picoseconds rather than nanoseconds. The resulting spin-flip time and resonance width of our model are $\tau_{sf}^0 = 7.14$ ns and $\Gamma = 100$ μeV, in agreement with other work ($\tau_{sf}^0 = 40$ ns, $\Gamma = 40$ μeV) using kinetic equations of a multi-level exciton system with similar expression for the electron-hole exchange, with the valley-pseudospin precession described in the strong scattering regime via the Dyakonov-Perrel mechanism as in Eq. 5.14 [185, 186].

Next, it is worth to point out the differences of this work from the above mentioned references. Here, the intervalley scattering rate γ_{sf} is a direct result of thermalisation and exchange interaction, without the inclusion of phonon-induced spin-lattice relaxation [185]. Also, only exciton spin-flips were taken into account, without separate electron and hole intervalley-scattering mechanisms [207]. Further, no additional field-dependent recombination and relaxation rates with phenomenological fit parameters were used as in Ref. [186].

In addition, in this work only two interlayer reservoirs describe the steady-state and time-dependent valley polarisation, with no additional spin-dark reservoirs in WSe_2 ML retaining valley polarisation as proposed in Ref. [34, 208].

In summary, we present a model with minimal assumptions deducted from optical selection rules of the H_h^h stacking in $MoSe_2$-WSe_2 HBL, where the detailed distinction between magnetic (P_c^{mag}) and optical (P_c^{opt}) degree of polarisation, together with the interplay of momentum-direct and indirect spin-triplet interlayer excitons T and $\tilde{T}$ reproduces the data. The modelling of P_c^{mag}, with thermalisation following the Boltzmann distribution between the Zeeman-split sub-bands of T, with known excitonic g-factor [33], in combination with radiative and non-radiative decay channels led to nonphysical high exciton temperatures ($\sim$ 60 K). Therefore, we included an energetic higher reservoir $\tilde{T}$ feeding the radiative population via valley-flip (γ_{vf}). The decrease of P_c^{opt} for small fields on the other hand is only captured with the inclusion of long-range Coulomb-induced exchange interaction.

Within our formalism of total exciton population (T/$\tilde{T}$) and valley pseudo-spin, we found explicit expressions for the contribution of each reservoir to the measured degree of circular polarisation. The steady-state system in thermal equilibrium is defined by the ratio of spin-flip rate to reservoir-specific losses, as well as by the initial population distribution (see Eq. 5.24). The magnetic field dependence of the spin-flip rates stems from Boltzmann-distributed population and exchange interaction. We excluded exchange interactions for momentum-indirect excitons, as expected from theory [36]. In our minimal model, we assume identical branching into momentum-direct and momentum-indirect interlayer exciton reservoirs. The induced optical polarisation, representing the initial valley selective population distribution, is the only parameter which changes between the resonant excitation at both ML resonances. With the inclusion of bi-molecular non-radiative decay in the rate equations, the time-resolved solution does not only reproduce the magnetic degree of circular polarisation in fair detail, but also is in reasonable agreement with its optical component, as well as the measured PL decay.

6 Summary and Outlook

The main goal of this work was to study light-matter interaction of two-dimensional TMD ML and van der Waals heterostructures at cryogenic temperatures. Their optical properties are dominated by excitons even at room temperature due to strong Coulomb-interactions [11]. The local band extrema within the hexagonal first Brillouin zone, commonly referred to as valleys, along with optical selection rules, determine the energetic position and polarisation of the PL response of these semiconductors [13]. Over the last years, the scientific community made remarkable progress in the fundamental understanding of the dominant transitions [53], where especially the increased sample quality by encapsulation in hexagonal boron nitride led to longer lifetimes, a drastic reduction in linewidth and thereby an emerging substructure in PL response contributed to localised excitons, phonon sidebands or charged exction emission [15, P1, 121].

To resolve this ambiguity, field-effect devices tuning the Fermi-level inside TMDs were implemented to distinguish charged exciton features such as trions and Fermi-polarons [209] from neutral excitons. To this end, in Chapter 3 we described the design, installation and operation of a fabrication setup in an inert gas atmosphere followed by a detailed description of the sample fabrication techniques. The exfoliation and transfer techniques as well as the identification of layer numbers in this work was used to expand the device architecture of our group to dual-gate structures, capable of tuning the electric field perpendicular to the TMD plane while varying the Fermi-level. The advances in doping and field control enabled the study of many-body effects on TMDs [210].

The first scope of this thesis described in Chapter 4, was to understand the PL substructure in encapsulated WSe_2 ML and BL. In the bilayer case the peak assignment is unambiguous, the PL stems from KQ momentum-indirect excitons and their phonon sidebands. For the ML bandstructure, theoretical DFT calculations predicted an energetic proximity of the high-symmetry points K and Q in the CBM of 10-40 meV [21]. As the momentum-direct spin-bright and spin-dark neutral excitons (X^0 and D^0) stem unambiguously from KK reservoirs, the red-shifted PL peak structure may either stem from KQ or KK' reservoirs and their

momentum-indirect phonon-assisted transitions [P1, 21, 72]. This work [P2] analysed the spectral asymmetry of phonon sideband luminescence of a sample tuned to charge neutrality in the temperature range from 4 to 100 K. A pronounced high-energy shoulder in momentum-indirect transitions was observed. In contrast, the momentum-direct exitons exhibited symmetric Lorentzian lineshapes , broadened by temperature due to exciton-phonon scattering and limited to the radiative cone. This limitation is lifted for higher-order processes that require the assistance of phonons to conserve momentum upon photon emission. Here, all thermally distributed states are allowed to recombine and contribute to the spectrum. The high-energy shoulder therefore is defined by the Maxwell-Boltzmann distribution.

We modelled the temperature-dependent behaviour for the BL and for the ML peaks red-shifted from the neutral exciton with a convolution of a Lorentzian with the Boltzmann-distribution. The extracted exciton temperature was found to generally follow that of the crystal lattice. Deviations from the lattice are indicative for the presence of hot exciton populations in the system and were found most pronounced for the BL case, where the radiative lifetime of 25 ps [172] approaches the timescale of the cooling processes [27]. This analysis gives direct experimental access to the temperature of excitons with finite center-of-mass momenta and provides additional insight into the fundamental electron-hole recombination processes in atomically thin semiconductors.

Further investigations into the PL response of WSe_2 ML may not only address the energetic position of the the Q-valley, which led to expanded discussions of the peaks M_1 and M_2, 30 meV and 51 meV red-shifted from the bright exciton, respectively [22, 23, 27, 156, 158]. Also, they reveal new signatures upon doping in the infrared, related to dark trion emission [211]. These findings provide additional insights into the spin-split conduction and valence bands. The knowledge gained from studying WSe_2 MLs enables the study of correlated physics, e.g. in twisted bilayer WSe_2 [212], where unconventional superconductivity has recently been demonstrated as a result of moiré-induced flat bands [213], overall making few-layer WSe_2 a highly interesting system.

The second scope of this thesis investigates interlayer excitons in a type-II $MoSe_2$-WSe_2 heterobilayer and its spin dynamics. The formation of heterostructures consisting of different TMD monolayer materials allows band-engineering [214] and introduces mesoscopic reconstrucion [33] between the adjacent layers, both impacting the valley polarisation. Chapter 5 focuses on cryogenic spectroscopy of a $MoSe_2$-WSe_2 HBL with H_h^h stacking (anti-parallel alignment of the centers of the hexagonal real-space lattices) as the dominant atomic registry at the experimentally chosen spot size. The relevant transitions are identified as the spin-triplet (T) and spin-singlet (S) interlayer excitons through exciton g-factor extraction and polarisation resolved spectroscopy [33, 178]. The triplet state shows zero degree of linear polarisation and the singlet shows a negative degree of circular polarisation. In addition, the sign of the g-factor as well as the degree of circular polarisation changes between singlet and

triplet state, in agreement with theoretical predictions based on DFT and optical selection rules [66].

Time- and polarisation resolved measurements of the triplet interlayer exciton transition were conducted at varying magnetic field to understand the spin-dynamics and dephasing mechanisms. First, the degree of circular polarisation was decomposed into magnetic and optical components, both theoretically and experimentally. The magnetic degree of circular polarisation is fully defined by thermalisation, resulting in a Boltzmann-dominated population redistribution between the Zeeman-split reservoirs. The optical degree of polarisation is inherited by the interlayer excitons from the polarised excitation at the 1s intralayer resonance due to their spin-lifetimes exceeding the timescales of intralayer formation [203].

We attributed the magnetic field dependent change of the spin-lifetime of excitons to a Hanle-like spin-precession mediated by long-range Coulomb interaction [36], leading to exciton spin flips without additional momentum transfer, which causes depolarisation at low magnetic field. A rate equation model was implemented and solved for the steady-state. We extracted the ratio of spin to radiative lifetime, with the assumption of momentum-direct and momentum-indirect spin-triplet states, connected via polarisation transferring valley-flips towards the radiative reservoir. Next, the rate equations were numerically solved as a function of time, successfully reproducing most trends in valley polarisation dynamics and PL decay. With that, we identified involved radiative, non-radiative, spin- and valley-flip timescales.

The manipulation of the valley degree of freedom led research from fundamental studies of ML TMD systems [193, 215] to the exploration of nanostructures [216] and further, to the the near endless combinations of HBL systems [217], where e.g. for $MoSe_2$-WSe_2 in H-type stacking near unity P_c was reported in magnetic fields up to 27 T [218]. Future research in the context of spin-dynamics, doping control [219, 220] and band-engineering via material choice, as well as twist-angle control [81, 221], enables tailored optical valley polarisation, critical to devices reaching from sensing, quantum computing and information to optoelectronic applications. In room temperature experiments with TMD monolayers for example, the degree of circular polarisation was recovered up to 61% for doping levels beyond $n_e = 10^{13}$ 1/cm^2 [220]. Additionally, experimental Kerr-spectroscopy [221] may provide an experimental access to neutral and charged interlayer exciton dephasing times. Another approach is to induce a Zeeman-splitting even at zero external field via the magnetic proximity effect of ferromagnetic substrates [186, 222], thereby suppressing the Coulomb exchange-interactions and increasing the degree of polarisation.

In summary, this dissertation studies the line-shape of phonon-sideband luminescence and dynamics of spin-valley polarisation in two separate TMD systems. The line-shape analysis in WSe_2 provides an experimental tool to distinguish between phonon-assisted and momentum direct exciton transitions. Further, it extracts the exction temperature. This analysis is applicable to the entire class of TMDs and beyond.

The study of interlayer exciton spin-dynamics in $MoSe_2$-WSe_2 HBL systems demonstrates a minimal model, where only the interplay of thermalisation and long-range Coulomb exchange interaction between the radiative and momentum-indirect triplet state were taken into account. With that, we were able to reproduce the steady-state and time-resolved magnetic-field dependent degree of circular polarisation, overall highlighting the role of momentum-indirect transitions in HBL systems.

Bibliography

1. Łukasiak, L. & Jakubowski, A. History of Semiconductors. *Journal of Telecommunications and Information Technology,* 3–9 (2023).
2. Moore, G. E. Cramming more components onto integrated circuits. *Electronics* **38,** 114 (1965).
3. Dennard, R., Gaensslen, F., Yu, H.-N., *et al.* Design of ion-implanted MOSFET's with very small physical dimensions. *JSSC* **9,** 256–268 (1974).
4. Novoselov, K. S., Geim, A. K., Morozov, S. V., *et al.* Electric Field Effect in Atomically Thin Carbon Films. *Science* **306,** 666–669 (2004).
5. Novoselov, K. S., Geim, A. K., Morozov, S. V., *et al.* Two-dimensional gas of massless Dirac fermions in graphene. *Nature* **438,** 197–200 (2005).
6. Zhang, Y., Tan, Y. W., Stormer, H. L., *et al.* Experimental observation of the quantum Hall effect and Berry's phase in graphene. *Nature* **438,** 201–204 (2005).
7. Kim, S., Konar, A., Hwang, W. S., *et al.* High-mobility and low-power thin-film transistors based on multilayer MoS_2 crystals. *Nat. Commun.* **3** (2012).
8. Slonczewski, J. & Weiss, P. Band Structure of Graphite. *Physical Review* **109,** 272–279 (1958).
9. Geim, A. K. & Novoselov, K. S. The rise of graphene. *Nat. Mater.* **6,** 183–191 (2007).
10. Mak, K. F., Lee, C., Hone, J., *et al.* Atomically Thin MoS_2: A New Direct-Gap Semiconductor. *Phys. Rev. Lett.* **105,** 136805 (2010).
11. Chernikov, A., Berkelbach, T. C., Hill, H. M., *et al.* Exciton binding energy and nonhydrogenic Rydberg series in monolayer WS2. *Phys. Rev. Lett.* **113,** 1–5 (2014).
12. Yao, W., Xiao, D. & Niu, Q. Valley-dependent optoelectronics from inversion symmetry breaking. *Phys. Rev. B* **77,** 1–7 (2008).
13. Cao, T., Wang, G., Han, W., *et al.* Valley-selective circular dichroism of monolayer molybdenum disulphide. *Nat. Commun.* **3** (2012).
14. Vitale, S. A., Nezich, D., Varghese, J. O., *et al.* Valleytronics: Opportunities, Challenges, and Paths Forward. *Small* **14,** 1–15 (2018).

15. Ajayi, O. A., Ardelean, J. V., Shepard, G. D., *et al.* Approaching the intrinsic photoluminescence linewidth in transition metal dichalcogenide monolayers. *2D Mater.* **4,** 031011 (2017).

16. Cadiz, F., Courtade, E., Robert, C., *et al.* Excitonic linewidth approaching the homogeneous limit in MoS_2-based van der waals heterostructures. *Phys. Rev. X* **7,** 021026 (2017).

17. Brem, S., Zipfel, J., Selig, M., *et al.* Intrinsic lifetime of higher excitonic states in tungsten diselenide monolayers. *Nanoscale* **11,** 12381–12387 (2019).

18. Mak, K. F., He, K., Lee, C., *et al.* Tightly bound trions in monolayer MoS_2. *Nat. Mater.* **12,** 207–211 (2013).

19. Ross, J. S., Wu, S., Yu, H., *et al.* Electrical control of neutral and charged excitons in a monolayer semiconductor. *Nat. Commun.* **4,** 1474 (2013).

20. Huang, J., Hoang, T. B. & Mikkelsen, M. H. Probing the origin of excitonic states in monolayer WSe_2. *Sci. Rep.* **6,** 1–7 (2016).

21. Deilmann, T. & Thygesen, K. S. Finite-momentum exciton landscape in mono- and bilayer transition metal dichalcogenides. *2D Mater.* **6,** 035003 (2019).

22. Brem, S., Ekman, A., Christiansen, D., *et al.* Phonon-assisted photoluminescence from indirect excitons in monolayers of transition-metal dichalcogenides. *Nano Lett.* **20,** 2849–2856 (2020).

23. He, M., Rivera, P., Van Tuan, D., *et al.* Valley phonons and exciton complexes in a monolayer semiconductor. *Nat. Commun.* **11,** 618 (2020).

24. Liu, F., Wu, W., Bai, Y., *et al.* Disassembling 2D van der Waals crystals into macroscopic monolayers and reassembling into artificial lattices. *Science* **367,** 903–906 (2020).

25. Moody, G., Kavir Dass, C., Hao, K., *et al.* Intrinsic homogeneous linewidth and broadening mechanisms of excitons in monolayer transition metal dichalcogenides. *Nat. Commun.* **6,** 8315 (2015).

26. Malic, E., Selig, M., Feierabend, M., *et al.* Dark excitons in transition metal dichalcogenides. *Phys. Rev. Mater.* **2,** 014002 (2018).

27. Rosati, R., Wagner, K., Brem, S., *et al.* Temporal evolution of low-temperature phonon sidebands in transition metal dichalcogenides. *ACS Photonics* **7,** 2756 (2020).

28. Geim, A. K. & Grigorieva, I. V. Van der Waals heterostructures. *Nature* **499,** 419–425 (2013).

29. Cao, Y., Fatemi, V., Fang, S., *et al.* Unconventional superconductivity in magic-angle graphene superlattices. *Nature* **556,** 43–50 (2018).

30. Regan, E. C., Wang, D., Jin, C., *et al.* Mott and generalized Wigner crystal states in WSe_2/WS_2 moiré superlattices. *Nature* **579,** 359–363 (2020).

31. Tsui, Y. C., He, M., Hu, Y., *et al.* Direct observation of a magnetic-field-induced Wigner crystal. *Nature* **628,** 287–292 (2024).

32. Mak, K. F. & Shan, J. Semiconductor moiré materials. *Nat. Nanotechnol.* **17** (2022).

33. Zhao, S., Li, Z., Huang, X., *et al.* Excitons in mesoscopically reconstructed moiré heterostructures. *Nat. Nanotechnol.* **18,** 572–579 (2023).

34. Jiang, C., Xu, W., Rasmita, A., *et al.* Microsecond dark-exciton valley polarization memory in two-dimensional heterostructures. *Nat. Commun.* **9,** 1–8 (2018).

35. Yu, T. & Wu, M. W. Valley depolarization due to intervalley and intravalley electron-hole exchange interactions in monolayer MoS_2. *Phys. Rev. B* **89,** 1–7 (2014).

36. Glazov, M. M., Amand, T., Marie, X., *et al.* Exciton fine structure and spin decoherence in monolayers of transition metal dichalcogenides. *Phys. Rev. B* **89,** 201302 (2014).

37. Wilson, J. & Yoffe, A. The transition metal dichalcogenides discussion and interpretation of the observed optical, electrical and structural properties. *Advances in Physics* **18,** 193–335 (1969).

38. Wang, Q. H., Kalantar-Zadeh, K., Kis, A., *et al.* Electronics and optoelectronics of two-dimensional transition metal dichalcogenides. *Nat. Nanotechnol.* **7,** 699–712 (2012).

39. Qian, X., Liu, J., Fu, L., *et al.* Quantum spin Hall effect in two-dimensional transition metal dichalcogenides. *Science* **346,** 1344–1347 (2014).

40. Xiao, D., Liu, G. B., Feng, W., *et al.* Coupled spin and valley physics in monolayers of MoS_2 and other group-VI dichalcogenides. *Phys. Revi. Lett.* **108,** 1–5 (2012).

41. Xu, X., Yao, W., Xiao, D., *et al.* Spin and pseudospins in layered transition metal dichalcogenides. *Nat. Phys.* **10,** 343–350 (2014).

42. Huang, Y., Sutter, E., Shi, N. N., *et al.* Reliable Exfoliation of Large-Area High-Quality Flakes of Graphene and Other Two-Dimensional Materials. *ACS Nano* **9,** 10612–10620 (2015).

43. Najmaei, S., Liu, Z., Zhou, W., *et al.* Vapour phase growth and grain boundary structure of molybdenum disulphide atomic layers. *Nat. Mater.* **12,** 754–759 (2013).

44. Cai, Z., Liu, B., Zou, X., *et al.* Chemical Vapor Deposition Growth and Applications of Two-Dimensional Materials and Their Heterostructures. *Chemical Reviews* **118,** 6091–6133 (2018).

45. Zhang, Y., Chang, T. R., Zhou, B., *et al.* Direct observation of the transition from indirect to direct bandgap in atomically thin epitaxial $MoSe_2$. *Nat. Nanotechnol.* **9,** 111–115 (2014).

46. Zhang, X., Qiao, X. F., Shi, W., *et al.* Phonon and Raman scattering of two-dimensional transition metal dichalcogenides from monolayer, multilayer to bulk material. *Chem. Soc. Rev.* **44,** 2757–2785 (2015).

47. Jin, Z., Li, X., Mullen, J. T., *et al.* Intrinsic transport properties of electrons and holes in monolayer transition-metal dichalcogenides. *Phys. Rev. B* **90,** 045422 (2014).

48. Zhao, W., Ghorannevis, Z., Amara, K. K., *et al.* Lattice dynamics in mono- and few-layer sheets of WS_2 and WSe_2. *Nanoscale* **5,** 9677–9683 (2013).

49. Zhang, L. & Niu, Q. Chiral Phonons at High-Symmetry Points in Monolayer Hexagonal Lattices. *Phys. Rev. Lett.* **115,** 1–5 (2015).

50. Zhu, H., Yi, J., Li, M.-Y., *et al.* Observation of chiral phonons. *Science* **359,** 579–582 (2018).

51. Li, T. & Galli, G. Electronic Properties of MoS_2 Nanoparticles. *J. Phys. Chem. C* **111,** 16192–16196 (2007).

52. Zhao, W., Ribeiro, R. M., Toh, M., *et al.* Origin of indirect optical transitions in few-layer MoS_2, WS_2, and WSe_2. *Nano Lett.* **13,** 5627–5634 (2013).

53. Wang, G., Chernikov, A., Glazov, M. M., *et al.* Colloquium: Excitons in atomically thin transition metal dichalcogenides. *Rev. Mod. Phys.* **90,** 021001 (2018).

54. Zhu, Z. Y., Cheng, Y. C. & Schwingenschlögl, U. Giant spin-orbit-induced spin splitting in two-dimensional transition-metal dichalcogenide semiconductors. *Phys. Rev. B* **84,** 1–5 (2011).

55. Komider, K., González, J. W. & Fernández-Rossier, J. Large spin splitting in the conduction band of transition metal dichalcogenide monolayers. *Phys. Rev. B* **88,** 1–7 (2013).

56. Kormányos, A., Zólyomi, V., Drummond, N. D., *et al.* Spin-orbit coupling, quantum dots, and qubits in monolayer transition metal dichalcogenides. *Phys. Rev. X* **4,** 1–16 (2014).

57. Liu, G.-B., Shan, W.-Y., Yao, Y., *et al.* Three-band tight-binding model for monolayers of group-VIB transition metal dichalcogenides. *Phys. Rev. B* **88,** 085433 (2013).

58. Koåmider, K. & Fernández-Rossier, J. Electronic properties of the MoS_2-WS_2 heterojunction. *Phys. Rev. B* **87,** 2–5 (2013).

59. Kormányos, A., Burkard, G., Gmitra, M., *et al.* $\mathrm{K} \cdot \mathrm{P}$ Theory for Two-Dimensional Transition Metal Dichalcogenide Semiconductors. *2D Mater.* **2,** 022001 (2015).

60. Echeverry, J. P., Urbaszek, B., Amand, T., *et al.* Splitting between bright and dark excitons in transition metal dichalcogenide monolayers. *Phys. Rev. B* **93,** 1–5 (2016).

61. Lindlau, J. Optical spectroscopy of charge-tunable atomically thin semiconductors at cryogenic temperatures. *PhD Thesis (LMU München)* (2019).

62. Macfarlane, G., McLean, T., Quarrington, J., *et al.* Exciton and phonon effects in the absorption spectra of germanium and silicon. *J. Phys. Chem. Solids* **8,** 388–392 (1959).

63. Sallen, G., Bouet, L., Marie, X., *et al.* Robust optical emission polarization in MoS_2 monolayers through selective valley excitation. *Phys. Rev. B* **86,** 3–6 (2012).

64. Zhang, X. X., You, Y., Zhao, S. Y. F., *et al.* Experimental evidence for dark excitons in monolayer WSe_2. *Phys. Rev. Lett.* **115,** 257403 (2015).

65. Wang, G., Robert, C., Glazov, M. M., *et al.* In-plane propagation of light in transition metal dichalcogenide monolayers: optical selection rules. *Phys. Rev. Lett.* **119,** 047401 (2017).

66. Förg, M., Colombier, L., Patel, R. K., *et al.* Cavity-control of interlayer excitons in van der Waals heterostructures. *Nat. Commun.* **10,** 1–6 (2019).

67. Förg, M., Baimuratov, A. S., Kruchinin, S. Y., *et al.* Moiré excitons in $MoSe_2$-WSe_2 heterobilayers and heterotrilayers. *Nat. Commun.* **12,** 1–7 (2021).

68. Hsu, W.-T., Lin, B.-H., Lu, L.-S., *et al.* Tailoring excitonic states of van der Waals bilayers through stacking configuration, band alignment, and valley spin. *Sci. Adv.* **5,** eaax7407 (2019).

69. He, J., Hummer, K. & Franchini, C. Stacking effects on the electronic and optical properties of bilayer transition metal dichalcogenides MoS_2, $MoSe_2$, WS_2, and WSe_2. *Phys. Rev. B* **89,** 1–11 (2014).

70. Li, Z., Förste, J., Watanabe, K., *et al.* Stacking-dependent exciton multiplicity in WSe_2 bilayers. *Phys. Rev. B* **106,** 1–10 (2022).

71. Gong, Y., Lei, S., Ye, G., *et al.* Two-Step Growth of Two-Dimensional WSe_2/$MoSe_2$ Heterostructures. *Nano Lett.* **15,** 6135–6141 (2015).

72. Hsu, W. T., Lu, L. S., Wu, P. H., *et al.* Negative circular polarization emissions from WSe_2/$MoSe_2$ commensurate heterobilayers. *Nat. Commun.* **9** (2018).

73. Förg, M. Confocal and cavity-enhanced spectroscopy of semiconductor van der Waals heterostructures. *PhD Thesis (LMU München)* (2020).

74. Hermann, K. Periodic overlayers and moiré patterns: Theoretical studies of geometric properties. *J. Phys.: Condens. Matter* **24** (2012).

75. Ghiotto, A., Shih, E. M., Pereira, G. S., *et al.* Quantum criticality in twisted transition metal dichalcogenides. *Nature* **597,** 345–349. eprint: 2103.09796 (2021).

76. Enaldiev, V. V., Zólyomi, V., Yelgel, C., *et al.* Stacking Domains and Dislocation Networks in Marginally Twisted Bilayers of Transition Metal Dichalcogenides. *Phys. Rev. Lett.* **124,** 206101 (2020).

77. Carr, S., Massatt, D., Torrisi, S. B., *et al.* Relaxation and domain formation in incommensurate two-dimensional heterostructures. *Phys. Rev. B* **98,** 1–7 (2018).

78. Liu, G. B., Xiao, D., Yao, Y., *et al.* Electronic structures and theoretical modelling of two-dimensional group-VIB transition metal dichalcogenides. *Chem. Soc. Rev.* **44,** 2643–2663 (2015).

79. Alexeev, E. M., Ruiz-Tijerina, D. A., Danovich, M., *et al.* Resonantly hybridized excitons in moiré superlattices in van der Waals heterostructures. *Nature* **567,** 81–86 (2019).

80. Tan, Q., Rasmita, A., Li, S., *et al.* Layer-engineered interlayer excitons. *Sci. Adv.* **7,** 1–9 (2021).

81. Jiang, Y., Chen, S., Zheng, W., *et al.* Interlayer exciton formation, relaxation, and transport in TMD van der Waals heterostructures. *Light Sci. Appl.* **10,** 1–29 (2021).

82. Chen, H., Wen, X., Zhang, J., *et al.* Ultrafast formation of interlayer hot excitons in atomically thin MoS_2/WS_2 heterostructures. *Nat.Commun.* **7,** 1–8 (2016).

83. Jin, C., Ma, E. Y., Karni, O., *et al.* Ultrafast dynamics in van der Waals heterostructures. *Nat. Nanotechnol.* **13,** 994–1003 (2018).

84. Miller, B., Steinhoff, A., Pano, B., *et al.* Long-Lived Direct and Indirect Interlayer Excitons in van der Waals Heterostructures. *Nano Lett.* **17,** 5229–5237 (2017).

85. Berghäuser, G. & Malic, E. Analytical approach to excitonic properties of MoS_2. *Phys. Rev. B* **89,** 1–6 (2014).

86. Gillen, R. & Maultzsch, J. Interlayer excitons in $MoSe_2/WSe_2$ heterostructures from first principles. *Phys. Rev. B* **97,** 1–7 (2018).

87. Torun, E., Miranda, H. P., Molina-Sánchez, A., *et al.* Interlayer and intralayer excitons in MoS_2/WS_2 and $MoSe_2/WSe_2$ heterobilayers. *Phys. Rev. B* **97,** 1–7 (2018).

88. Landau, L. D. & Lifshitz, L. M. *Quantum Mechanics Non-Relativistic Theory, Third Edition: Volume 3* 3rd ed. (Butterworth-Heinemann, Jan. 1981).

89. Koster, G. *Properties of the Thirty-two Point Groups* (M.I.T. Press, 1963).

90. Enaldiev, V. V., Ferreira, F., Magorrian, S. J., *et al.* Piezoelectric networks and ferroelectric domains in twistronic superlattices in WS_2/MoS_2 and $WSe_2/MoSe_2$ bilayers. *2D Mater.* **2** (2021).

91. Förste, J. Spectroscopy of gate-tunable thin films of tungsten-diselenide. *Master Thesis (LMU München)* (2018).

92. Kwak, D., Polyushkin, D. K. & Mueller, T. In-sensor computing using a MoS_2 photodetector with programmable spectral responsivity. *Nat. Commun.* **14** (2023).

93. Lu, Z., Chen, Y., Dang, W., *et al.* Wafer-scale high-κ dielectrics for two-dimensional circuits via van der Waals integration. *Nat. Commun.* **14,** 1–8 (2023).

94. Li, T., Guo, W., Ma, L., *et al.* Epitaxial growth of wafer-scale molybdenum disulfide semiconductor single crystals on sapphire. *Nat. Nanotechnol.* **16,** 1201–1207 (2021).

95. Chen, Z., Xie, C., Wang, W., *et al.* Direct growth of wafer-scale highly oriented graphene on sapphire. *Sci. Adv.* **7,** 1–7 (2021).

96. Kim, K. S., Lee, D., Chang, C. S., *et al.* Non-epitaxial single-crystal 2D material growth by geometric confinement. *Nature* **614,** 88–94 (2023).

97. Li, Z., Ren, L., Wang, S., *et al.* Dry Exfoliation of Large-Area 2D Monolayer and Heterostructure Arrays. *ACS Nano* **15,** 13839–13846 (2021).

98. Janavika, K. & Prakash Thangaraj, R. Graphene and its application: A review. *Mater. Today Proc.* (2023).

99. Urade, A. R., Lahiri, I. & Suresh, K. S. Graphene Properties, Synthesis and Applications: A Review. *Jom* **75,** 614–630 (2023).

100. Marega, G. M., Ji, H. G., Wang, Z., *et al.* Large-Scale Integrated Vector-Matrix Multiplication Processor Based on Monolayer MoS_2 (2023).

101. Datta, I., Chae, S. H., Bhatt, G. R., *et al.* Low-loss composite photonic platform based on 2D semiconductor monolayers. *Nat. Photonics* **14,** 256–262 (2020).

102. Masubuchi, S., Morimoto, M., Morikawa, S., *et al.* Autonomous robotic searching and assembly of two-dimensional crystals to build van der Waals superlattices. *Nat. Commun.* **9,** 4–6 (2018).

103. Greplova, E., Gold, C., Kratochwil, B., *et al.* Fully automated identification of two-dimensional material samples. *Physical Review Applied* **13,** 1 (2020).

104. Uslu, J.-L., Ouaj, T., Tebbe, D., *et al.* An open-source robust machine learning platform for real-time detection and classification of 2D material flakes. *Mach. Learn.: Sci. Technol.* **5,** 015027 (2024).

105. The interface is still the device. *Nature Materials* **11,** 91–91 (2012).

106. Li, Q., Zhou, Q., Shi, L., *et al.* Recent advances in oxidation and degradation mechanisms of ultrathin 2D materials under ambient conditions and their passivation strategies. *J. Mater. Chem. A* **7,** 4291–4312 (2019).

107. Cowie, M., Plougmann, R., Benkirane, Y., *et al.* How high is a $MoSe_2$ monolayer? *Nanotechnology* **33,** 125706 (2022).

108. Blake, P., Hill, E. W., Castro Neto, A. H., *et al.* Making graphene visible. *Appl. Phys. Lett.* **91** (2007).

109. Benameur, M. M., Radisavljevic, B., Héron, J. S., *et al.* Visibility of dichalcogenide nanolayers. *Nanotechnology* **22** (2011).

110. Pizzocchero, F., Gammelgaard, L., Jessen, B. S., *et al.* The hot pick-up technique for batch assembly of van der Waals heterostructures. *Nat. Commun.* **7** (2016).

111. Neumann, A., Lindlau, J., Colombier, L., *et al.* Opto-valleytronic imaging of atomically thin semiconductors. *Nat. Nanotechnol.* **12,** 329–334 (2017).

112. Alexeev, E. M., Catanzaro, A., Skrypka, O. V., *et al.* Imaging of Interlayer Coupling in van der Waals Heterostructures Using a Bright-Field Optical Microscope. *Nano Lett.* **17,** 5342–5349 (2017).

113. Zeng, H., Liu, G. B., Dai, J., *et al.* Optical signature of symmetry variations and spin-valley coupling in atomically thin tungsten dichalcogenides. *Sci. Rep.* **3,** 4908–4916 (2013).

114. Zhao, W., Ghorannevis, Z., Amara, K. K., *et al.* Lattice dynamics in mono- and few-layer sheets of WS2 and WSe2. *Nanoscale* **5,** 9677–9683 (2013).

115. Liang, L. & Meunier, V. First-principles Raman spectra of MoS_2, WS_2 and their heterostructures. *Nanoscale* **6,** 5394–5401 (2014).

116. Tonndorf, P., Schmidt, R., Böttger, P., *et al.* Photoluminescence emission and Raman response of monolayer MoS_2, $MoSe_2$, and WSe_2. *Opt. Express* **21,** 4908–4916 (2013).

117. Funk, V. Spectroscopy of momentum-dark excitons in layered semiconductors. *Master Thesis (LMU München)* (2017).

118. Cassabois, G., Valvin, P. & Gil, B. Hexagonal boron nitride is an indirect bandgap semiconductor. *Nat. Photonics* **10,** 262–266 (2016).

119. Laturia, A., Van de Put, M. L. & Vandenberghe, W. G. Dielectric properties of hexagonal boron nitride and transition metal dichalcogenides: from monolayer to bulk. *npj 2D Mater Appl* **2,** 1–7 (2018).

120. Dean, C. R., Young, A. F., Meric, I., *et al.* Boron nitride substrates for high-quality graphene electronics. *Nat. Nanotechnol.* **5,** 722–726 (2010).

121. Wierzbowski, J., Klein, J., Sigger, F., *et al.* Direct exciton emission from atomically thin transition metal dichalcogenide heterostructures near the lifetime limit. *Sci. Rep.* **7,** 12383– (2017).

122. Courtade, E., Semina, M., Manca, M., *et al.* Charged excitons in monolayer WSe_2: experiment and theory. *Phys. Rev. B* **96,** 085302 (2017).

123. Raja, A., Selig, M., Berghaüser, G., *et al.* Enhancement of Exciton-Phonon Scattering from Monolayer to Bilayer WS_2. *Nano Lett.* **18,** 6135–6143 (2018).

124. Zheng, Z., Cox, M. C. & Li, B. Surface modification of hexagonal boron nitride nanomaterials: a review. *J. Mater. Sci.* **53,** 66–99 (2018).

125. Gorbachev, R. V., Riaz, I., Nair, R. R., *et al.* Hunting for monolayer boron nitride: Optical and raman signatures. *Small* **7,** 465–468 (2011).

126. Fang, H. H., Han, B., Robert, C., *et al.* Control of the Exciton Radiative Lifetime in van der Waals Heterostructures. *Physical Review Letters* **123,** 67401. arXiv: 1902.00670 (2019).

127. Popert, A. Optically Probing Graphene-Excitonic Sensing of Electronic States. *PhD Thesis (ETH Zürich)* (2022).

128. Rhodes, D., Chae, S. H., Ribeiro-Palau, R., *et al.* Disorder in van der Waals heterostructures of 2D materials. *Nat. Mater.* **18,** 541–549 (2019).

129. Cheliotis, I. & Zergioti, I. A review on transfer methods of two-dimensional materials. *2D Mater.* **11** (2024).

130. Castellanos-Gomez, A., Buscema, M., Molenaar, R., *et al.* Deterministic transfer of two-dimensional materials by all-dry viscoelastic stamping. *2D Mater.* **1** (2014).

131. Taniguchi, T., Jain, A., Parzefall, M., *et al.* Minimizing residues and strain in 2D materials transferred from PDMS. *Nanotechnology* **29,** 265203 (2018).

132. Zomer, P. J., Guimarães, M. H., Brant, J. C., *et al.* Fast pick up technique for high quality heterostructures of bilayer graphene and hexagonal boron nitride. *Appl. Phys. Lett.* **105** (2014).

133. Purdie, D. G., Ferrari, A. C. & Lombardo, A. Cleaning interfaces in layered materials heterostructures. *Nat. Commun.* **9,** 5387 (2018).

134. Frisenda, R., Navarro-Moratalla, E., Gant, P., *et al.* Recent progress in the assembly of nanodevices and van der Waals heterostructures by deterministic placement of 2D materials. *Chem. Soc. Rev.* **47,** 53–68 (2018).

135. Lee, W. M., Upadhya, A., Reece, P. J., *et al.* Fabricating low cost and high performance elastomer lenses using hanging droplets. *Biomed. Opt. Express* **5,** 1626 (2014).

136. Rupp, A. Characterisation of Layered Semiconductors with Scanning Electron Microscopy Techniques. *Master Thesis (LMU München)* (2022).

137. Krelle, L. Plasmon-Exciton-Polaritons in Two-Dimensional Semiconductors Strongly Coupled to Gold Nanoparticle Arrays. *Master Thesis (LMU München)* (2022).

138. Goeser, J. Fabrication and Optical Spectroscopy of Twisted van der Waals Heterostructures. *Master Thesis (LMU München)* (2019).

139. Kim, Y., Herlinger, P., Taniguchi, T., *et al.* Reliable Postprocessing Improvement of van der Waals Heterostructures. *ACS Nano* **13,** 14182–14190 (2019).

140. Younas, R., Zhou, G. & Hinkle, C. L. A perspective on the doping of transition metal dichalcogenides for ultra-scaled transistors: Challenges and opportunities. *Appl. Phys. Lett.* **122** (2023).

141. Mondal, A., Biswas, C., Park, S., *et al.* Low Ohmic contact resistance and high on/off ratio in transition metal dichalcogenides field-effect transistors via residue-free transfer. *Nat. Nanotechnol.* **19** (2023).

142. Nguyen, H. P. G. Fabrication and Optical Spectroscopy of Two-dimensional Magnetic Semiconductor CrSBr. *Master Thesis (LMU München)* (2023).

143. Macfarlane, G. G., McLean, T. P., Quarrington, J. E., *et al.* Fine structure in the absorption-edge spectrum of Ge. *Phys. Rev.* **108,** 1377–1383 (1957).

144. Macfarlane, G. G., McLean, T. P., Quarrington, J. E., *et al.* Fine structure in the absorption-edge spectrum of Si. *Phys. Rev.* **111,** 1245–1254 (1958).

145. Haynes, J. & Briggs, H. Radiation produced in germanium and silicon by electron-hole recombination. *Phys. Rev.* **86,** 647–647 (1952).

146. Newman, R. Optical studies of injected carriers. II. Recombination radiation in germanium. *Phys. Rev.* **91,** 1313–1314 (1953).

147. Haynes, J. R. New radiation resulting from recombination of holes and electrons in germanium. *Phys. Rev.* **98,** 1866–1868 (1955).

148. Haynes, J. R. & Westphal, W. C. Radiation resulting from recombination of holes and electrons in silicon. *Phys. Rev.* **101,** 1676–1678 (1956).

149. Bonfanti, M., Grilli, E., Guzzi, M., *et al.* Optical transitions in Ge/SiGe multiple quantum wells with Ge-rich barriers. *Phys. Rev. B* **78,** 041407 (2008).

150. Giorgioni, A., Gatti, E., Grilli, E., *et al.* Photoluminescence decay of direct and indirect transitions in Ge/SiGe multiple quantum wells. *J. Appl. Phys.* **111,** 013501 (2012).

151. Splendiani, A., Sun, L., Zhang, Y., *et al.* Emerging photoluminescence in monolayer MoS_2. *Nano Lett.* **10,** 1271–1275 (2010).

152. Zhou, Y., Scuri, G., Wild, D. S., *et al.* Probing dark excitons in atomically thin semiconductors via near-field coupling to surface plasmon polaritons. *Nat. Nanotechnol.* **12,** 856–860 (2017).

153. Zhang, X.-X., Cao, T., Lu, Z., *et al.* Magnetic brightening and control of dark excitons in monolayer WSe_2. *Nat. Nanotechnol.* **12,** 883–888 (2017).

154. Arora, A., Koperski, M., Nogajewski, K., *et al.* Excitonic resonances in thin films of WSe_2: from monolayer to bulk material. *Nanoscale* **7,** 10421–10429 (2015).

155. Koperski, M., Molas, M. R., Arora, A., *et al.* Optical properties of atomically thin transition metal dichalcogenides: Observations and puzzles. *Nanophotonics* **6,** 1289–1308 (2017).

156. Liu, E., van Baren, J., Taniguchi, T., *et al.* Valley-selective chiral phonon replicas of dark excitons and trions in monolayer WSe_2. *Phys. Rev. Res.* **1,** 032007 (2019).

157. Wang, G., Marie, X., Gerber, I., *et al.* Giant enhancement of the optical second-harmonic emission of WSe_2 monolayers by laser excitation at exciton resonances. *Phys. Rev. Lett.* **114** (2015).

158. Van Tuan, D., Jones, A. M., Yang, M., *et al.* Virtual trions in the photoluminescence of monolayer transition-metal dichalcogenides. *Phys. Rev. Lett.* **122,** 217401 (2019).

159. Robert, C., Amand, T., Cadiz, F., *et al.* Fine structure and lifetime of dark excitons in transition metal dichalcogenide monolayers. *Phys. Rev. B* **96,** 155423 (2017).

160. Aslan, O. B., Deng, M., Brongersma, M. L., *et al.* Strained bilayer WSe_2 with reduced exciton-phonon coupling. *Phys. Rev. B* **101,** 115305 (2020).

161. Li, Z., Wang, T., Jin, C., *et al.* Emerging photoluminescence from the dark-exciton phonon replica in monolayer WSe_2. *Nat. Commun.* **10,** 2469 (2019).

162. Varshni, Y. P. Temperature dependence of the energy gap in semiconductors. *Physica* **34,** 149–154 (1967).

163. O'Donnell, K. P. & Chen, X. Temperature dependence of semiconductor band gaps. *Appl. Phys. Lett.* **58,** 2924–2926 (1991).

164. Rudin, S., Reinecke, T. & Segall, B. Temperature-dependent exciton linewidths in semiconductors. *Phys. Rev. B* **42,** 11218–11231 (1990).

165. Selig, M., Berghäuser, G., Raja, A., *et al.* Excitonic linewidth and coherence lifetime in monolayer transition metal dichalcogenides. *Nat. Commun.* **7,** 13279 (2016).

166. Dey, P., Paul, J., Wang, Z., *et al.* Optical coherence in atomic-monolayer transition-metal dichalcogenides limited by electron-phonon interactions. *Phys. Rev. Lett.* **116,** 127402 (2016).

167. Shree, S., Semina, M., Robert, C., *et al.* Observation of exciton-phonon coupling in $MoSe_2$ monolayers. *Phys. Rev. B* **98,** 035302 (2018).

168. Umlauff, M., Hoffmann, J., Kalt, H., *et al.* Direct observation of free-exciton thermalization in quantum-well structures. *Phys. Rev. B* **57,** 1390–1393 (1998).

169. Xu, S. J., Li, G. Q., Xiong, S.-J., *et al.* Temperature dependence of the LO phonon sidebands in free exciton emission of GaN. *J. Appl. Phys.* **99,** 073508 (2006).

170. Klingshirn, C. *Semiconductor Optics* 3rd (Springer, Berlin Heidelberg New York, 2007).

171. Chellappan, V., Pang, A. L. C., Sarkar, S., *et al.* Effect of phonons on valley depolarization in monolayer WSe_2. *Electron. Mater. Lett.* **14,** 766–773 (2018).

172. Wang, G., Marie, X., Bouet, L., *et al.* Exciton dynamics in WSe_2 bilayers. *Appl. Phys. Lett.* **105,** 182105 (2014).

173. Rivera, P., Schaibley, J. R., Jones, A. M., *et al.* Observation of long-lived interlayer excitons in monolayer $MoSe_2$-WSe_2 heterostructures. *Nat. Commun.* **6,** 4–9 (2015).

174. Li, Z., Tabataba-Vakili, F., Zhao, S., *et al.* Lattice Reconstruction in $MoSe_2$-WSe_2 Heterobilayers Synthesized by Chemical Vapor Deposition. *Nano Lett.* **23,** 4160–4166 (2023).

175. Weston, A., Zou, Y., Enaldiev, V., *et al.* Atomic reconstruction in twisted bilayers of transition metal dichalcogenides. *Nat. Nanotechnol.* **15,** 592–597 (2020).

176. Rosenberger, M. R., Chuang, H. J., Phillips, M., *et al.* Twist Angle-Dependent Atomic Reconstruction and Moiré Patterns in Transition Metal Dichalcogenide Heterostructures. *ACS Nano* **14,** 4550–4558 (2020).

177. Horng, J., Stroucken, T., Zhang, L., *et al.* Observation of interlayer excitons in $MoSe_2$ single crystals. *Phys. Rev. B* **97,** 241404 (2018).

178. Wietek, E., Florian, M., Göser, J., *et al.* Nonlinear and Negative Effective Diffusivity of Interlayer Excitons in Moiré-Free Heterobilayers. *Phys. Rev. Lett.* **132,** 16202 (2024).

179. Brotons-Gisbert, M., Baek, H., Campbell, A., *et al.* Moiré-Trapped Interlayer Trions in a Charge-Tunable $WSe_2/MoSe_2$ Heterobilayer. *Phys. Rev. X* **11,** 1–12 (2021).

180. Baranowski, M., Surrente, A., Maude, D. K., *et al.* Dark excitons and the elusive valley polarization in transition metal dichalcogenides. *2D Mater.* **4,** 025016 (2017).

181. Bai, Y., Zhou, L., Wang, J., *et al.* Excitons in strain-induced one-dimensional moiré potentials at transition metal dichalcogenide heterojunctions. *Nat. Mater* **19,** 1068–1073 (2020).

182. Palummo, M., Bernardi, M. & Grossman, J. C. Exciton radiative lifetimes in two-dimensional transition metal dichalcogenides. *Nano Lett.* **15,** 2794–2800 (2015).

183. Erkensten, D., Brem, S., Wagner, K., *et al.* Dark exciton-exciton annihilation in monolayer WSe_2. *Phys. Rev. B* **104,** 1–7 (2021).

184. Goryca, M., Li, J., Stier, A. V., *et al.* Revealing exciton masses and dielectric properties of monolayer semiconductors with high magnetic fields. *Nat. Commun.* **10,** 1–12 (2019).

185. Surrente, A., Kłopotowski, Ł., Zhang, N., *et al.* Intervalley Scattering of Interlayer Excitons in a $MoS_2/MoSe_2/MoS_2$ Heterostructure in High Magnetic Field. *Nano Lett.* **18,** 3994–4000 (2018).

186. Castro, E. C., Brandão, D. S., Bragança, H., *et al.* Mechanisms of interlayer exciton emission and giant valley polarization in van der Waals heterostructures. **107,** 035439 (2023).

187. Dey, P., Yang, L., Robert, C., *et al.* Gate-Controlled Spin-Valley Locking of Resident Carriers in WSe_2 Monolayers. *Phys. Rev. Lett.* **119,** 1–5 (2017).

188. Hanle, W. Über magnetische Beeinflussung der Polarisation der Resonanzfluoreszenz. *Zeitschrift für Physik* **30,** 93–105 (1924).

189. Dyakonov, M. & Perel, V. in *Optical Orientation-Theory of Optical Spin Orientation of Electrons and Nuclei in Semiconductors* 11–71 (Elsevier, 1984).

190. Worsley, R. E., Traynor, N. J., Grevatt, T., *et al.* Transient Linear Birefringence in GaAs Quantum Wells: Magnetic Field Dependence of Coherent Exciton Spin Dynamics. *Phys. Rev. Lett.* **76,** 3224–3227 (1996).

191. Blackwood, E., Snelling, M. J., Harley, R. T., *et al.* Exchange interaction of excitons in GaAs heterostructures. *Phys. Rev. B* **50,** 14246–14254 (1994).

192. Maialle, M. Z., de Andrada e Silva, E. A. & Sham, L. J. Exciton spin dynamics in quantum wells. *Phys. Rev. B* **47,** 15776 (1993).

193. Smoleński, T., Goryca, M., Koperski, M., *et al.* Tuning valley polarization in a WSe_2 monolayer with a tiny magnetic field. *Phys. Rev. X* **6,** 1–7 (2016).

194. Smoleński, T., Kazimierczuk, T., Goryca, M., *et al.* Magnetic field induced polarization enhancement in monolayers of tungsten dichalcogenides: effects of temperature. *2D Mater.* **5,** 015023 (2017).

195. Yang, L., Sinitsyn, N. A., Chen, W., *et al.* Long-lived nanosecond spin relaxation and spin coherence of electrons in monolayer MoS_2 and WS_2. *Nat. Phys.* **11,** 830–834 (2015).

196. Glazov, M. M., Ivchenko, E. L., Wang, G., *et al.* Spin and valley dynamics of excitons in transition metal dichalcogenide monolayers. *Phys. Status Solidi B Basic Res.* **252,** 2349–2362 (2015).

197. Hao, K., Moody, G., Wu, F., *et al.* Direct measurement of exciton valley coherence in monolayer WSe_2. *Nat. Phys.* **12,** 677–682 (2016).

198. Srivastava, A., Sidler, M., Allain, A. V., *et al.* Valley Zeeman effect in elementary optical excitations of monolayer WSe_2. *Nat. Phys.* **11,** 141–147 (2015).

199. Ivchenko, E. *Optical Spectroscopy of Semiconductor Nanostructures* (Alpha Science, 2005).

200. Rivera, P., Seyler, K. L., Yu, H., *et al.* Valley-polarized exciton dynamics in a 2D semiconductor heterostructure. *Science* **351,** 688–691 (2016).

201. Dyakonov, M. & Perel, V. Spin relaxation of conduction electrons in noncentrosymmetric semiconductors. *Sov. Phys. Solid State* **13** (1972).

202. Xu, W., Liu, W., Schmidt, J. F., *et al.* Correlated fluorescence blinking in two-dimensional semiconductor heterostructures. *Nature* **541,** 62–67 (2017).

203. Ovesen, S., Brem, S., Linderälv, C., *et al.* Interlayer exciton dynamics in van der Waals heterostructures. *Commun. Phys.* **2** (2019).

204. Holler, J., Selig, M., Kempf, M., *et al.* Interlayer exciton valley polarization dynamics in large magnetic fields. *Phys. Rev. B* **105,** 1–9 (2022).

205. Shamirzaev, T. S., Debus, J., Yakovlev, D. R., *et al.* Dynamics of exciton recombination in strong magnetic fields in ultrathin GaAs/AlAs quantum wells with indirect band gap and type-II band alignment. *Phys. Rev. B* **94,** 1–10 (2016).

206. Shamirzaev, T. S., Rautert, J., Yakovlev, D. R., *et al.* Spin dynamics and magnetic field induced polarization of excitons in ultrathin GaAs/AlAs quantum wells with indirect band gap and type-II band alignment. *Phys. Rev. B* **96,** 1–15 (2017).

207. Smirnov, D. S., Holler, J., Kempf, M., *et al.* Valley-magnetophonon resonance for interlayer excitons. *2D Mater.* **9,** 045016 (2022).

208. Tang, Y., Mak, K. F. & Shan, J. Long valley lifetime of dark excitons in single-layer WSe_2. *Nat. Commun.* **10,** 4047 (2019).

209. Ganchev, B., Drummond, N., Aleiner, I., *et al.* Three-Particle Complexes in Two-Dimensional Semiconductors. *Phys. Rev. Lett.* **114,** 107401 (2015).

210. Polovnikov, B., Scherzer, J., Misra, S., *et al.* Field-Induced Hybridization of Moiré Excitons in $MoSe_2/WS_2$ Heterobilayers. *Phys. Rev. Lett.* **132,** 1–7 (2024).

211. Jindal, V., Mourzidis, K., Balocchi, A., *et al.* Brightened emission of dark trions in transition-metal dichalcogenide monolayers. *https://arxiv.org/abs/2406.02095* (2024).

212. Knüppel, P., Zhu, J., Xia, Y., *et al.* Correlated states controlled by tunable van Hove singularity in moiré WSe_2. *https://arxiv.org/abs/2406.03315* (2024).

213. Xia, Y., Han, Z., Watanabe, K., *et al.* Unconventional superconductivity in twisted bilayer WSe_2. *https://arxiv.org/abs/2405.14784* (2024).

214. Kang, J., Tongay, S., Zhou, J., *et al.* Band offsets and heterostructures of two-dimensional semiconductors. *Appl. Phys. Lett.* **102,** 012111 (2013).

215. Aivazian, G., Gong, Z., Jones, A. M., *et al.* Magnetic control of valley pseudospin in monolayer WSe_2. *Nat. Phys.* **11,** 148–152 (2015).

216. Barman, P. K., Sarma, P. V., Shaijumon, M. M., *et al.* High degree of circular polarization in WS_2 spiral nanostructures induced by broken symmetry. *Sci. Rep.* **9,** 1–7 (2019).

217. Kim, J., Jin, C., Chen, B., *et al.* Observation of ultralong valley lifetime in WSe_2/MoS_2 heterostructures. *Sci. Adv.* **3,** e1700518 (2017).

218. Nagler, P., Ballottin, M. V., Mitioglu, A. A., *et al.* Giant magnetic splitting inducing near-unity valley polarization in van der Waals heterostructures. *Nat. Commun.* **8,** 1–6 (2017).

219. Chakraborty, C., Mukherjee, A., Qiu, L., *et al.* Electrically tunable valley polarization and valley coherence in monolayer WSe_2 embedded in a van der Waals heterostructure. *Opt. Mater. Express* **9,** 1479–1487 (2019).

220. Morozov, S., Yezekyan, T., Wolff, C., *et al.* Inducing room-temperature valley polarization of excitonic emission in transition metal dichalcogenide monolayers. *npj 2D mater. appl.* **8,** 24 (2024).

221. Volmer, F., Ersfeld, M., Faria Junior, P. E., *et al.* Twist angle dependent interlayer transfer of valley polarization from excitons to free charge carriers in $WSe_2/MoSe_2$ heterobilayers. *npj 2D mater. appl.* **7,** 58 (2023).

222. Bragança, H., Zeng, H., Dias, A. C., *et al.* Magnetic-gateable valley exciton emission. *Npj Comput. Mater.* **6,** 1–9 (2020).

List of Publications

P1. Lindlau, J., Robert, C., Funk, V., *et al.* Identifying optical signatures of momentum-dark excitons in monolayer transition metal dichalcogenides. *https://arxiv.org/abs/1710.00988* (2017).

P2. Funk, V., Wagner, K., Wietek, E., *et al.* Spectral asymmetry of phonon sideband luminescence in monolayer and bilayer WSe_2. *Phys. Rev. Res.* **3,** L042019 (2021).

P3. Förste, J., Tepliakov, N. V., Kruchinin, S. Y., *et al.* Exciton g-factors in monolayer and bilayer WSe_2 from experiment and theory. *Nat. Commun.* **11,** 4539 (2020).

P4. Lindlau, J., Selig, M., Neumann, A., *et al.* The role of momentum-dark excitons in the elementary optical response of bilayer WSe_2. *Nat. Commun.* **9,** 2586 (2018).

Acknowledgments

The time has finally come, the end is near. After, lets say a few years, my time as a PhD student under Prof. Alexander Högele is coming to an end — a perfect opportunity to express my gratitude. After playing with tape as my very first task as a master's student, I wasn't expecting to find myself inside a PhD defense. Thank you, Alex, for supporting me at every opportunity and, especially, for your patience during difficult times. I'm grateful for your enthusiasm for quasi-particles created and manipulated by light, for the toys passed down from your daughters, drinks at Christmas parties, and the years of loyal coffee consumption. That last point obviously applies to the whole LS Kotthaus; it was a pleasure to work here.

Big thanks to my first supervisor, Michael Förg. He was my role model in balancing work-life, research, fatherhood and silly jokes. Jonathan Förste and Samarth Vadia, thank you for your relentless support, friendship, and visionary ideas, which we are now bringing to life together. Cheers to many more years on the frontlines of research and, hopefully, soon at the heart of industry! Thanks to the first generation I witnessed completing their PhDs: Manuel Nutz for your English humor and hacker talents, Jonathan Noé and Thomas Hümmer for showing how to spin off from university while focusing on family, and Jessica Lindlau and Andre Neumann for your attention to detail in lab organisation and physics.

And to the newer generation of partially fresh PhDs, Postdocs, and young colleagues, thank you for daily discussions about whether an alternative lunch spot to Mensa was an option. Jonas Gösser, thank you for discussions about finger-strength training, as well as your research in CVD-growth of TMDs. Borislav Polovnikov, for discussions on income inequality. Subhradeep Misra, Shen Zhao, and Farsane Tabataba-Vakili, for insights into academic career paths, a helping hand in the lab and a reintroduction to board games. Anvar Baimuratov, for shared kids' activities, bouldering and blackboard sessions. Lukas Husel, for advice on how to achieve my next goal—El Cap. Julian Trapp, for our shared love of the Kurfürstenstüberl. Thanks to Tim Wedl for good music and relentless fab-discussions. Johannes Scherzer and Anna Rupp, thank you for bringing your good mood to the office, sharing the love for good cappuccino and the enthusiasm for sports.

Special thanks to Prof. Alexey Chernikov, who influenced my understanding of TMDs from the very beginning with his beautiful pictorial approach. Our collaboration had laid the foundation for this thesis. Also, Prof. Mikhail Glazov, thank you for establishing the theoretical concepts this thesis is build on.

To the permanent employees of the physics department: The backbone of everything

related to sample fabrication and clean-room work was formed by Philipp Altpeter and Christian Obermayer. Thank you both for years of help and productive discussions — without you, half of the science done in this building wouldn't have been possible. Thanks also to Anton Heindl for technical support, Stefan Manus for electrical assistance and life stories, and Bert Lorenz and Dayse Ferreira e Silva for your administrative support.

Beyond the university, I wouldn't be here without the lifelong support of my family and friends. To my fellow Funkies: You are the best, kabam, check, noroc! I know you were suffering with me. Milo and Lucian, you make my life worth living.